M.Sc. Thesis

Controlling Single-Photon Generation With Nano-Mechanical Devices

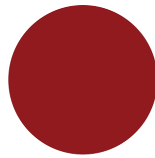

UNIVERSITY OF COPENHAGEN

Lasse Stampe Frølich

Controlling Single-Photon Generation With Nano-Mechanical Devices

Author	Lasse Stampe Frølich
Supervisor	Assoc. Prof. Leonardo Midolo
Co-Supervisor	Prof. Peter Lodahl

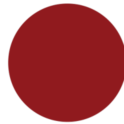

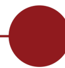

UNIVERSITY OF
COPENHAGEN

Dissertation for the degree of Master of Science

The Niels Bohr Institute

Submitted to the University of Copenhagen
December 6, 2020

Abstract

Scalable quantum photonic technologies require generating, manipulating, and detecting a large number of single photons entirely on-chip. An essential component of such photonic circuits is an efficient, deterministic source of highly indistinguishable photons. Semiconductor quantum dots offer a promising route towards this aim. Embedding these solid-state emitters within photonic nanostructures modulates their surrounding optical environment, and provides a direct interface to their emission properties. In this way, efficient generation of highly indistinguishable, pure photons with near-unity coupling to photonic structures has been reported.

So far, most successful approaches utilize passive photonic nanostructures, that are extremely sensitive to spatial and spectral variations in the quantum dots. As semiconductor quantum dots nucleate at random during growth, this poses a major obstacle towards efficiently and consistently enhancing their emission properties. A central challenge in realizing quantum dot emitters as truly on-demand sources of single photons thus becomes efficiently interfacing their emission properties in a controllable way, independent of their position.

This work introduces two novel devices addressing this issue: a mirror with tunable reflectively, and a tunable phase shifter. These devices are based on the emerging class of nano-opto-electro-mechanical systems, with optical responses that are modulated by nanoscale mechanical deformations induced by electrostatic actuation. This effectively electro-optic interface allows for efficient reconfiguration on-demand by applying an external voltage bias. These devices offer in-plane, compact geometries, are compatible with cryogenic temperatures, and can be integrated directly on-chip.

Characterization of the nano-mechanical mirror demonstrated tuning of the transmission of a broadband coherent light source through the device by up to 98 %, corresponding to an extinction ratio of 17.0 dB. This was shown over a wavelength range of over 35 nm, with a mechanical displacement of only 23 nm. The efficient reconfigurability of the mirror makes it an excellent candidate for creating tunable on-chip cavities. The nano-mechanical phase shifter demonstrated enhancement of the emission rate of an embedded InGaAs quantum dot by up to a factor 2.44. Numerical models are developed that support the findings of both devices and indicate that the performance of the phase shifter can be significantly enhanced by reducing device losses.

On their own, or in combination with other photonic structures, these devices offer a promising path towards efficient, on-demand single-photon sources, essential for the realization of advanced quantum photonic architectures on-chip.

Acknowledgements

First, I would like to thank my supervisors, Peter Lodahl and Leonardo Midolo, for inviting me into the group and guiding me through this project. Leonardo, who was in charge of the daily supervision, deserves my deepest gratitude. Despite the busiest of schedules, he somehow always managed to make time for me and my endless questions. His inexhaustible knowledge, expertise, and fundamental empathy and kindness have been invaluable throughout the last 15 months.

My sincere thanks goes to Xiaoyan Zhou, for spending countless hours with me in the lab, always pushing me to strive for the best, and for her indispensable ideas and contributions. Thank you to Zhe Liu, for providing me with comprehensive knowledge of fabrication, teaching me all the tips and tricks, and for the many pleasant hours spent fabbing together.

I would like to thank the entire Quantum Photonics group and Hy-Q collaboration for welcoming me with open arms, and creating an environment full constructive scientific discussions, laughter, cake, and dank memes. A special thanks goes to Camille Papon, Ying Wang, Ravitej Uppu, Adam Knorr and Arianne Brooks for their assistance during this project.

To my office mates in the (self)proclaimed office-of-the-year, 5 years running, thank you for making every day at the office enjoyable and fun.

I am particularly grateful for my parents, who have always supported me and shown interest in what I do, despite likely not understanding much of it. I would not be where I am today without them, literally, as I would never have been born.

To my girlfriend Hannah, who has been by my side throughout the ups and downs: thank you for being a continuous source of love and support. I genuinely could not have done this without you.

I would like to dedicate this work to my late grandfather, Thomas Arnold Sørensen.

List of Abbreviations

CB - Conduction band

CPD - Critical point dryer/drying

DC - Directional coupler

EBL - Electron-beam lithography

ER - Extinction rato

FSR - Free spectral range

ICP - Inductively coupled plasma

IRF - Instrument response function

IPA - Isopropyl alcohol

LDOS - Local density of optical states

MEMS (NEMS) - Micro(Nano)-electro-mechanical system

MQ - Milli-Q

NMP - N-Methyl-2-pyrrolidone

NOEM(S) - Nano-opto-electro-mechanical (systems)

PID - Proportional-integral-derivative

PVD - Physical vapor deposition

QD - Quantum dot

(Q)PIC - (Quantum) photonic integrated circuit

RF - Radio frequency

RIE - Reactive ion etching

RT - Room temperature

SEG - Shallow-etched grating

SEM - Scanning electron micrograph

SPAD - Single-photon avalanche diode

TE (TM) - Transverse electric (magnetic)

VB - Valence band

Contents

1 Introduction **1**

2 Nano-mechanical devices for quantum photonic circuits **5**
2.1 Single-photon sources . . . 7
2.1.1 Quantum dots . . . 7
2.1.2 Excitation schemes . . . 8
2.1.3 Spontaneous emission of quantum dots in nanostructures . . . 9
2.2 The directional coupler . . . 12
2.2.1 Photonic switches . . . 12
2.2.2 The tunable beamsplitter . . . 13
2.2.3 Introduction to coupled-mode theory . . . 14
2.3 Novel NOEM-based devices . . . 17
2.3.1 S-matrix formalism . . . 18
2.3.2 Tunable NOEM mirror . . . 21
2.3.3 Tunable NOEM phase shifter . . . 23

3 Fabrication of NOEM devices **27**
3.1 Sample growth . . . 28
3.2 Electron-beam lithography . . . 29
3.3 Fabrication procedure . . . 31
3.3.1 Metal deposition and lift-off . . . 31
3.3.2 Etching of shallow-etched gratings . . . 32
3.3.3 Etching and undercut of photonic structures . . . 34
3.3.4 Finishing cleaning and drying procedure . . . 35
3.4 Fabrication results . . . 36

4 Experimental setup **37**

5 Characterization of the tunable NOEM mirror **41**
5.1 Broadband optical characterization . . . 42
5.1.1 Fringes analysis . . . 43
5.1.2 Transmission bandwidth . . . 44
5.2 Comparison to S-matrix model . . . 44
5.2.1 Device losses . . . 46
5.2.2 Improving the S-matrix model . . . 46
5.3 Transmission fine scan . . . 48
5.4 Concluding remarks . . . 50

6 Characterization of the tunable NOEM phase shifter 53
6.1 Quantum dot localization and characterization 54
6.2 Tuning of the quantum dot emission rate 56
6.2.1 Comparison to the S-matrix model 58
6.2.2 Temporal shift 59
6.2.3 Spectral tuning of cavity mode resonances 60
6.2.4 Impact of device losses 62
6.3 Fluorescence lifetime measurements 63
6.4 Concluding remarks 65

7 Conclusion and outlook 67

Bibliography 71

A Cascading junctions formalism 77
A.1 Degenerate cases 78
A.2 Matlab code 79

B Optimized fabrication recipe 81

CHAPTER 1

Introduction

The second half of the 20th century ushered in a scientific revolution within the field of quantum physics [1]. Previously, physicists had seen great success in applying the laws of quantum mechanics to understand some of the most fundamental forces of nature. While these developments profoundly increased our understanding of the physical world, it was a slight change of perspective in the 1980's that ended up defining the modern role of quantum physics: rather than viewing quantum systems as something to be *explained*, scientists started viewing them as something that can be *designed* [2]. This lead to the unification of quantum mechanics, information theory, and computer science, to form the field of *quantum information theory*, which today has become a cornerstone of contemporary quantum physics.

At the heart of this new paradigm is the quantum bit, the quantum mechanical analogue to a classical computational bit. Whereas a classical bit can encompass the values 0 and 1, for a quantum bit, or *qubit*, these two values correspond to quantum states, of which the qubit can exist in any superposition thereof [3]. The amount of information stored in an n-qubit system scales as 2^n, giving a quantum computer the potential to become exceedingly more powerful than a classical computer could ever become [4]. Quantum information protocols have been developed that would be near-impossible to implement on even the most advanced classical supercomputers, but can be efficiently solved with quantum computers. The most famous examples include Shor's factoring algorithm [5] (which, if successfully implemented, would seriously endanger the security of current public-key cryptography schemes), Grover's database search algorithm [6], and protocols for the simulation of quantum systems [7, 8].

Single photons stand out as excellent candidates for the realization of several quantum applications, as qubits can be encoded in numerous degrees of freedom of the photon, such as polarization states, spatial modes, and temporal modes [9]. Proof-of-concept demonstrations of universal quantum computing on a photonic platform has recently been shown with linear-optic photonic processors [10, 11]. The tremendous potential of the quantum photonic foundation is further underlined by a publication released just days before the hand-in of this thesis, in which Gaussian boson sampling with up to 50 photon inputs was achieved, for the first

time demonstrating quantum computational advantage with photons [12]. It is estimated that it would take the most powerful classical supercomputer in the world 600 million years to do such a computation - here, it was performed within an hour. Furthermore, as single photons are the natural carriers of information over extended distances, they would be integral in a future *quantum internet* [13, 14], promising secure communication with quantum key distribution protocols [15], and secure access to remote quantum computers [16].

However, the realization of large-scale quantum photonic technologies require an efficient, on-demand source of highly pure, indistinguishable single photons [17, 18]. Semiconductor quantum dots have in recent years seen rapid advancements, and offer a promising route towards a fully deterministic photon source [19]. These solid-state emitters can be embedded directly in photonic nanostructures such as waveguides [20], photonic crystals [21], and nano-scale optical cavities [22] which modulate the surrounding optical environment to enhance vital emission properties such as emission rate, coupling efficiency and photon indistinguishability. These structures are however inherently fixed upon fabrication, and the achieved enhancement therefore shows pronounced sensitivity to spatial and spectral variations of the quantum dots [23]. As the prevalent method of growth for quantum dots rely on self-assembly, the randomness of their nucleation leads to irregular spatial distributions and inhomogeneously broadened emission frequencies, thus posing a severe obstacle for further advancements [24]. Developing a *truly* on-demand, high-purity single-photon source towards scalable quantum photonic experiments therefore requires *active* control of a quantum dot's emission properties by manipulating the surrounding optical environment.

This could be achieved with reconfigurable photonic devices. For such devices to be efficiently integrated within photonic architectures, they must be operable at the cryogenic temperatures required for coherent quantum dot emission [25], exhibit high reconfigurability and have small, in-plane geometries. A suitable platform for creating devices meeting these criteria is found in nano-opto-electro-mechanical systems (NOEMS), a novel class of hybrid systems coupling optical, electrical and mechanical degrees of freedom [26]. NOEMS rely on mechanically modifying photonic structures at the nanoscale via electrostatic actuation to tune optical fields, thus creating an effective electro-optic interaction. As opposed to several other means of interfacing optical fields, this interaction is strong regardless of the material properties of which it is composed, and can therefore be applied to numerous material platforms. This approach has recently been used to successfully implement high-performance optical switches [27], phase-shifters [28] and tunable optical nanocavities [29] on-chip.

In this work, two novel, reconfigurable photonic devices for controlling the emission properties of embedded quantum dot emitters are presented: a tunable mirror, and a tunable phase shifter. These integrated, chip-scale devices are based on the NOEMS framework, with the optical response modulated by an in-plane mechanical motion induced by electrostatic actuation. This thesis will focus on presenting the underlying theoretical framework governing their working principles, the methods and techniques required to fabricate them, and the results of comprehensive measurements characterizing their optical responses.

In chapter 2, the quantum dot emitter, as well as the light-matter interaction governing its emission, is first introduced. A summary of the relevant theories describing the opto-electro-mechanical interaction in these devices is presented, and theoretical models simulating the devices' performances are developed. Chapter 3 introduces the processes and methods relevant for fabricating the devices (as well as numerous other photonic devices), and chapter 4 describes the experimental setup used in this work. The results and subsequent discussions of the optical characterization measurements of the devices are split into two chapters, with chapter 5 presenting measurements to quantify the tunable reflectivity of the mirror, and chapter 6 presenting measurements to determine the emission rate enhancement of an embedded QD with the phase shifter. Lastly, chapter 7 gives an overview of the obtained results and an outlook to future works.

CHAPTER 2

Nano-mechanical devices for quantum photonic circuits

Photonic integrated circuits (PICs), comprised of a combination of optical components, allow for integrating numerous photonic functions on a single chip of semiconductor material. Intuitively similar to electronic integrated circuits, the difference lies in PICs processing optical signals as opposed to electronic signals. In recent decades, PICs have become increasingly important in modern telecommunication systems, to improve the speed and reduce the size of optical transceivers while keeping low network power consumption. Today, rapid developments in semiconductor growth and manufacturing techniques allow for the development of PICs for quantum applications, e.g. for implementing quantum information protocols based on linear optics, benefiting from the compactness, reconfigurability and low-loss that integrating optical channels and elements directly on a single chip provide [11]. As an example of such PICs, fig. 2.1 shows a universal linear optical processor, consisting of 15 Mach-Zender interferometers with 30 thermo-optic phase shifters, that can be programmed to implement up to 1000 quantum experiments [10]. Here, single photons are supplied by an external source and are coupled into the PIC.

External single photon source

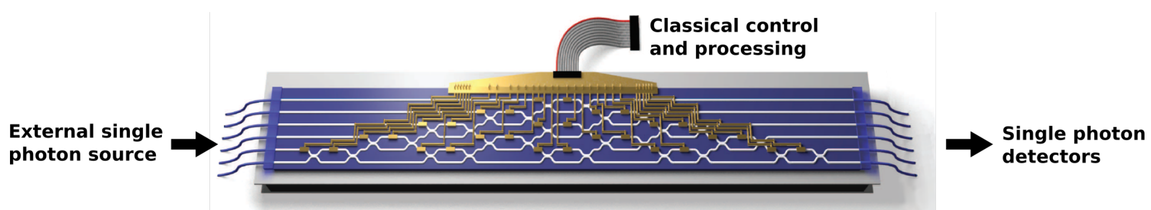

Figure 2.1: Universal linear optic processor. A compact, waveguide-based PIC in silica-on-silicon, which can be programmed into arbitrary configurations for a multitude of quantum experiments. Revision of figure from [10].

However, implementing large linear-optical quantum circuits with tens of quantum bits set very demanding scaling requirements [30], since many high-rate streams of single photons have to be efficiently coupled in the circuits. Therefore, to realise large scale and compact complex quantum architectures, integrating deterministic single

photon sources directly on-chip becomes a necessity [31]. A promising candidate for such integrated sources are self-assembled InGaAs quantum dots (QDs) embedded in GaAs nanophotonic structures [23]. These QDs offer near on-demand and highly indistinguishable photons, and have been studied rigorously in the past decade [32, 33]. Utilizing QDs as single-photon sources in advanced quantum photonic integrated circuits (QPICs) requires efficient control of their emission properties [34], ideally with photonic devices directly integrated on-chip. Efficient collection can be obtained by embedding QDs in 1D single-mode waveguides [35], and including a mirror ensures that emission is only collected in one direction [36]. However, the random nucleation of QDs during growth lead to random spatial distributions and inhomogenous spectral distributions. As pictured in fig. 2.2, this collection scheme may therefore lead to suppression of the QD emission rate. By modifying the optical

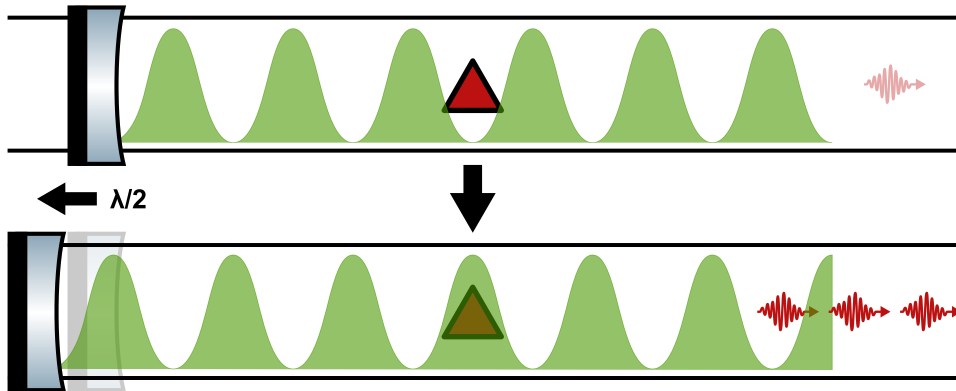

Figure 2.2: Quantum dot emission in a 1D waveguide with a movable mirror. (Top) The geometry of a 1D waveguide ensures that the QD (red triangle) emits mainly into guided modes. Placing a mirror to direct all emitted photons in one direction may lead to suppressing the QD emission, as the position of the QD may place be at a node of the surrounding field ($|E|^2$ indicated by green curves). (Bottom) The QD emission can be greatly enhanced by moving the mirror, placing the QD in an anti-node of the surrounding field.

environment surrounding the QD, intuitively comparable to moving the mirror, the emission rate of the QD can be directly interfaced [37]. A promising platform for creating a photonic device with such functionality is found in NOEMS [26]. In this project, two such devices built on the NOEM framework are presented. The central building block for these devices is the NOEM directional coupler (DC), which has recently shown promising results utilized as a photonic router [38]. The electrically controlled, nano-mechanical DC offers low losses, high reconfigurability, quick switching times and a compact footprint, making it an excellent foundation for the further development of integrated photonic devices. This chapter will first introduce the QD single-photon sources used in this work, and illustrate how the light-matter interaction can be controlled by modifying the emitters' environment. A description of the NOEM DC and the coupled-mode theory governing its operation is then given, followed by an introduction to the novel NOEM based devices that are the main focus of this thesis, concluding in a derivation of their working principles.

2.1 Single-photon sources

The performance of single-photon sources can be gauged by three figures-of-merit [19]: (1) Single-photon purity - only single photons should be emitted, meaning a negligible probability of emitting multiple photons, (2) single-photon coupling efficiency - coupling between emitted photons and desired optical modes should approach unity, and (3) indistinguishability - for use in most quantum applications, single photons are required to be highly indistinguishable. Self-assembled QDs, most notably InGaAs QDs embedded in GaAs semiconductors, have proven to be an excellent choice of single-photon emitters, due in part to their high performance in all three of these figures-of-merit, and in part because they can be directly integrated in a QPIC. In this section, an introduction to the optical properties of self-assembled QDs is provided, followed by a description of how they can be interfaced to nanophotonic waveguides.

2.1.1 Quantum dots

A common approach to creating QDs is by the epitaxial (layer-by-layer) growth of semiconductor heterostructures, through a process known as the Stranski-Krastanov method, relying on the *self-assembly* of the QDs [23]. As an example, the growth of InGaAs QDs grown on top of a GaAs substrate, similar to the ones investigated in this work, is considered. Initially, monolayers of InAs are grown layer-by-layer on top of a GaAs substrate by *molecular-beam epitaxy*, a process that is described in detail in chapter 3. Due to the 7 % mismatch in lattice constants between InAs and GaAs, strain is introduced between the two layers. As the thickness of the InAs *wetting layer* is increased, this strain is released with the formation of small, randomly positioned, pyramidal shaped islands - also known as *quantum dots* [39], pictured in fig. 2.3.a. Subsequent capping of these QDs with GaAs protects them from oxidation, and gives them a more truncated pyramidal shape. This method of growth yields an inherently random distribution of QDs, but the density can be controlled by adjusting the growth parameters. Typical self-assembled QDs are 1-10 nm in height, and 10-70 nm in width.

In a semiconductor material such as GaAs, the electron dispersion relation in the conduction band (CB) can locally be approximated by a parabola. The electrons experience a strong periodic potential reflecting the crystal lattice of the semiconductor, meaning that the curvature of the CB can no longer be determined using the rest mass of the electron. Instead, the curvature is dependent on the *effective mass* of the electron. The effective mass describes the motion of an electron wavepacket in a periodic potential, as if it was a free electron. However, in the valence band (VB) of the semiconductor material, the curvature is negative, resulting in a negative effective mass, as illustrated in fig. 2.3.b. Exciting an electron to the CB creates an absence of an electron, that due to the negative effective mass, rises up in the VB. This absence can be understood as a new type of particle, denoted a *hole*. Exciting an electron to the CB can thus be thought of as generating an electron-hole pair, a process which has the same energy as the band gap energy. Within the QD, nanoscale confinement in all three spatial dimensions leads to an effective *zero-dimensional* system with discrete energy levels in both the CB and

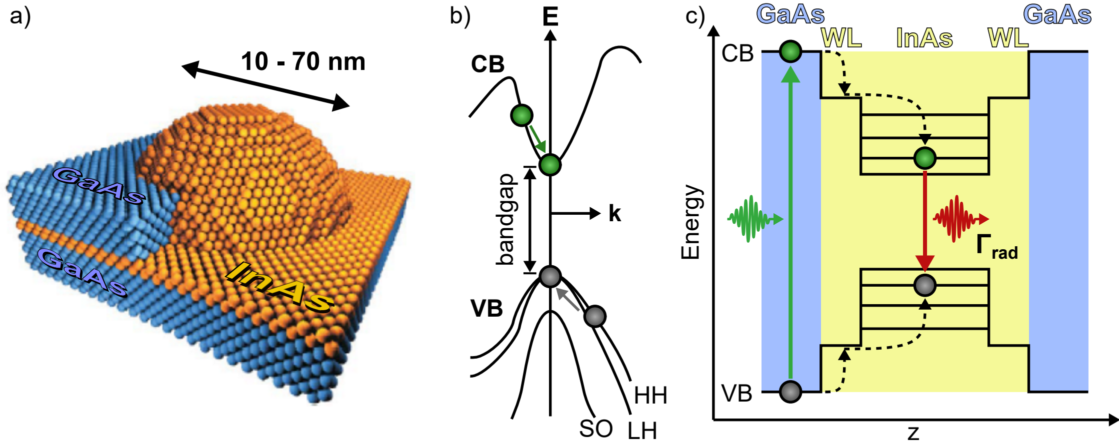

Figure 2.3: Self-assembled InGaAs quantum dots. a. Monolayers of InAs (orange) are deposited on top of GaAs (blue), and strain is released in the random formation of island-shaped structures (QDs) that are subsequently capped by a layer of GaAs. **b.** Electronic band structure in a QD. Electrons in the CB fall down, while holes in the VB rise up. The VB is split into three sub-bands due to spin-orbit interactions and confinement. **c.** Energy diagram of a QD along the growth direction. Electrons can be optically excited to the CB forming an electron-hole pair, which may be trapped within the QD due to its lower energy band gap, where it may recombine with the emission of a single photon.

valence band VB, as shown in fig. 2.3.c. The energy levels mimic those of an atom, resulting in QDs often being referred to as *artificial atoms* (though QDs typically consist of $\sim 10^5$ atoms). As is also evident from the figure, the energy band gap between the CB and VB bands of InGaAs is smaller than that of the surrounding GaAs, an example of a type I heterointerface [40]. These two factors allow the formation of a Coulomb interaction bound state, known as an *exciton* $|X\rangle$, consisting of an electron and a hole occupying the CB and VB, respectively. This corresponds to one of several possible excited states of the QD. With time, the electron-hole pair may recombine by emitting a single photon, leaving the QD in its ground state. The average time it takes for an exciton to recombine is defined as the *lifetime*, and is around 1 ns for QDs in bulk. The lifetime, or spontaneous decay rate, can however be highly modified by altering the QDs surrounding dielectric environment. The energy of the emitted photon is identical to that of the energy levels within the QD. Differences in QD size leads to variations in the energy levels, thereby causing an inhomogenous broadening of the spectral distribution of the emitted photons from a QD-ensemble. Spatially isolating single emitters in low-QD-density materials allows for addressing individual QDs, and by implementing resonant excitation schemes, even individual transitions can be addressed [41], in conjunction providing a near on-demand source of very pure single-photons.

2.1.2 Excitation schemes

Several schemes can be implemented to optically excite QDs, that depend on the frequency of the pumping laser. One such scheme is *above band* excitation, in which the frequency of the pumping laser is equal to that of the GaAs band gap energy.

This is illustrated in fig. 2.3.c, where an electron-hole pair is formed in the GaAs band gap that eventually becomes trapped within the QD due to the lower band gap energy of InGaAs. This method is easy to carry out in the lab, but has the disadvantage of possibly exciting higher exciton energy levels, producing a multi-emission spectrum. The excitation energy can also be *quasiresonant*, and match either a continuum of states in the wetting layer (with a similar mechanism to above band excitation), or an excited exciton state (also known as *p-shell* excitation). Finally, an excitation energy resonant with the exciton transition energy directly excites electron-hole pairs within the QD, providing the cleanest spectrum, but is more challenging to implement experimentally as it requires filtering the resonant excitation laser to achieve pure single-photon emission. A nanophotonic device capable of filtering residual light in resonant QD excitation [41] was recently developed in the Quantum Photonics group, making this excitation scheme more feasible. In this work, QDs are mainly addressed by the above band excitation scheme using a pulsed diode laser with a central emission wavelength of 795 nm, as this method does not require filtering of residual light.

2.1.3 Spontaneous emission of quantum dots in nanostructures

A considerable advantage of using semiconductor QD emitters is that they can be directly integrated in photonic nanostructures. This not only provides efficient collection of the emitted photons, but also allows for directly modifying the properties of the emitter using its surrounding environment. In the following, the emission properties of a QD incorporated in a one-dimensional nanobeam waveguide is described using the local density of optical states (LDOS) formalism. In short, the LDOS is the spatially-resolved density of optical modes at a given frequency, a quantity which directly determines the spontaneous emission of an emitter, and more generally, the local light-matter interaction strength.

Electronic states in semiconductor quantum dots

In the following derivations, the QD emitter will be approximated by a two-level system with an excited state $|e\rangle$ and ground state $|g\rangle$, separated by the transition frequency ω_0. For a periodic potential such as in the crystalline structure of a semiconductor, the electron wave-function is given by the Bloch wavefunctions [42]:

$$\psi_{\mathbf{k}}(\mathbf{r}) = u_{\mathbf{k}}(\mathbf{r})e^{-i\mathbf{k}\cdot\mathbf{r}}, \tag{2.1}$$

where $\mathbf{k}$ is the electron wave-vector. The Bloch wavefunctions are periodic, with similar periodicity as the atomic crystal structure. A heterojunction such as the type-I heterojunction of an InGaAs QD in GaAs, can be represented in the *envelope function* formalism as a slowly-varying perturbation of the crystal lattice potential. In this case, the electron (or hole) wave-function is approximated by a Bloch-function evaluated at $\mathbf{k} = 0$, modulated by a slowly-varying envelope function $F_n(\mathbf{r})$:

$$\psi_n(\mathbf{r}) \simeq F_n(\mathbf{r})u_{n0}(\mathbf{r}), \tag{2.2}$$

where the index n denotes the band-index ($n = c, v$ for CB and VB, respectively). Within the QD, the VB is split into three otherwise degenerate sub-bands: the split-off, light hole, and heavy hole bands, as shown in fig. 2.3.b. The split-off band is shifted to a lower energy due to spin-orbit interactions. The light and heavy hole bands have different effective masses (hence their names), resulting in different curvatures. They have different Bloch functions, which ultimately affect the optical selection rules in the QD. As the transitions between the conduction band and heavy-hole band have the lowest energy, it is in most cases a good approximation to neglect transitions to the light-hole band [23]. The relevant transition in QDs are therefore between electrons and heavy-holes, and the excited and ground states become:

$$\begin{aligned}\Psi_e(\mathbf{r}) &= \langle \mathbf{r}|e\rangle = F_e(\mathbf{r})u_{c0}(\mathbf{r}),\\ \Psi_g(\mathbf{r}) &= \langle \mathbf{r}|g\rangle = F_{hh}(\mathbf{r})u_{hh0}(\mathbf{r}).\end{aligned} \tag{2.3}$$

Spontaneous decay of an emitter

In the Wigner-Weisskopf approximation [43], the radiative decay rate of an emitter can be calculated using Fermi's golden rule [44], which gives the transition rate between an energy eigenstate of an emitter to either a discrete state or continuum of states:

$$\Gamma_{i\rightarrow f} = \frac{2\pi}{\hbar}\left|\langle f|\,\hat{H}_{int}\,|i\rangle\right|^2 \delta(E_{final} - E_{initial}) \tag{2.4}$$

The initial and final states are in this case given by:

$$\begin{aligned}|i\rangle &= |e\rangle \otimes |0\rangle\,,\\ |f\rangle &= \sum_{\mathbf{k}} |g\rangle \otimes |1_{\mathbf{k}}\rangle\,,\end{aligned} \tag{2.5}$$

where $|1_{\mathbf{k}}\rangle$ corresponds to an emitted single photon with wave-vector $\mathbf{k}$ (disregarding the two polarization components for each wave-vector). In the electric dipole approximation, the interaction Hamiltonian is given by:

$$\hat{H}_{int} = -q\hat{\mathbf{r}} \cdot \hat{\mathbf{E}}(\mathbf{r_0}, t), \tag{2.6}$$

where q is the elementary charge, $\hat{\mathbf{r}}$ is the dipole moment operator, and $\hat{\mathbf{E}}(\mathbf{r_0}, t)$ is the electric field evaluated the position of the quantum dot r_0. In quantized form, the electric field is given by:

$$\hat{\mathbf{E}}(\mathbf{r}) = i\sum_{\mathbf{k}} \mathbf{e_k}\mathcal{E}_{\mathbf{k}}(E_{\mathbf{k}}(\mathbf{r})\hat{a}_{\mathbf{k}} - E^*_{\mathbf{k}}(\mathbf{r})\hat{a}^\dagger_{\mathbf{k}}), \tag{2.7}$$

where $\mathbf{e_k}$ is the field orientation unit vector, $E_{\mathbf{k}}(\mathbf{r})$ is the spatial distribution of the electric field, and $\hat{a}_{\mathbf{k}}$ and $\hat{a}^\dagger_{\mathbf{k}}$ are the field annihilation and creation operators, respectively. The amplitude of this field is the vacuum fluctuation field $\mathcal{E}_{\mathbf{k}} = \sqrt{\frac{\hbar\omega_{\mathbf{k}}}{2\epsilon_0}}$, where $\omega_{\mathbf{k}}$ is the optical angular frequency. Plugging in the expressions for the electric field, interaction Hamiltonian, and initial and final states into eq. 2.4 and dismissing terms yielding zero gives:

$$\Gamma_{rad} = \frac{2\pi q^2}{\hbar}\sum_{\mathbf{k}} \mathcal{E}^2_{\mathbf{k}}|\,\langle g|\,\hat{\mathbf{r}} \cdot \mathbf{e_k}E^*_{\mathbf{k}}\,|e\rangle\,|^2\delta(\hbar\omega_0 - \hbar\omega_{\mathbf{k}}). \tag{2.8}$$

Decomposing the dipole moment into $\hat{\mathbf{r}} = \hat{r}\mathbf{e_r}$ and substituting the expression for the vacuum fluctuation field, the equation simplifies to:

$$\Gamma_{rad} = \frac{\pi q^2 \omega_0}{\hbar \epsilon_0} | \langle g | \hat{r} | e \rangle |^2 \sum_{\mathbf{k}} |\mathbf{e_r} \cdot \mathbf{e_k}|^2 |E_{\mathbf{k}}|^2 \delta(\omega_0 - \omega_{\mathbf{k}}). \quad (2.9)$$

For the case of a QD, the matrix element $\langle g | \hat{r} | e \rangle$ can be derived in the envelope function formalism (assuming a slowly-varying envelope function) as [42]:

$$\langle g | \hat{r} | e \rangle = r_{vc} \langle F^*_{hh} | F_e \rangle , \quad (2.10)$$

where $r_{vc} = \langle u_v | \hat{r} | u_c \rangle$ is the dipole matrix element between element between the CB and VB.

The final expression for the spontaneous decay rate thus becomes:

$$\Gamma_{rad} = \frac{\pi q^2 \omega_0}{\hbar \epsilon_0} |r_{vc}|^2 | \langle F^*_{hh} | F_e \rangle |^2 \rho(\mathbf{r}_0, \mathbf{e_r}, \omega_0), \quad (2.11)$$

where the projected local density of optical states

$$\rho(\mathbf{r}_0, \mathbf{e_r}, \omega_0) = \sum_{\mathbf{k}} |\mathbf{e_r} \cdot \mathbf{e_k}|^2 |E_{\mathbf{k}}|^2 \delta(\omega_0 - \omega_{\mathbf{k}}) \quad (2.12)$$

has been introduced. It describes the mode density of the vacuum fluctuation field that is "seen" by an emitter. The resulting emission spectrum is a Lorentzian with a central frequency ω_0 and FWHM of Γ_{rad}. Equation 2.11 shows that the spontaneous decay rate can be controlled by modifying the LDOS. The suppression or enhancement of the spontaneous decay rate is commonly known as the *Purcell effect*, and can be implemented with photonic nano-structures in the emitter's environment to modify the LDOS. The ratio of the enhancement due to the environment, as compared to in a homogeneous bulk medium, is given by the *Purcell factor*:

$$F_p = \frac{\Gamma_{rad}}{\Gamma_{hom}}. \quad (2.13)$$

Altering the LDOS thus also allows for control of the radiated power, as for a continuous-wave excitation the radiated power is:

$$P = \hbar \omega_0 \Gamma_{rad}. \quad (2.14)$$

In this work, InGaAs QDs are embedded within suspended GaAs nanobeam waveguides. Due to the high difference in the refractive index of GaAs ($n_2 \approx 3.55$ for $\lambda = 940$ nm at room temperature) and air $n_1 \approx 1$, light is confined due to total internal reflection. Changing the physical size of the waveguides changes the effective refractive index n_{eff} of the guided modes with propagation constants $\beta = kn_{eff}$, and only allows guided modes fulfilling $kn_2 > \beta > kn_1$ [42]. Modes with propagation constants $\beta \leq kn_1$, leak out of the waveguide, and are hence called *leaky modes*. For a GaAs nanobeam waveguide of width 300 nm and thickness 160 nm, only the fundamental transverse electric (TE_0) and transverse magnetic (TM_0) modes are allowed to propagate. The TE_0 mode is of special interest, as this has an electric field component mainly oriented in the y-direction, as illustrated in fig. 2.4.

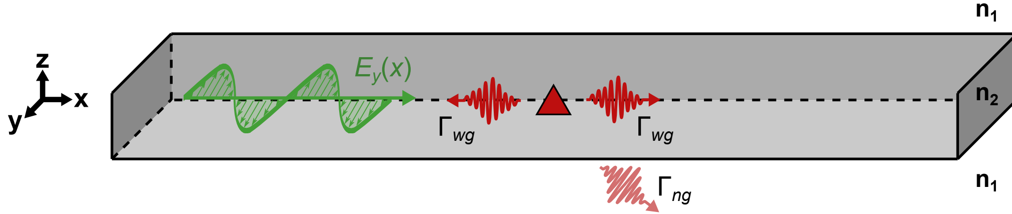

Figure 2.4: Quantum dot emission in a nano-beam waveguide. The dimensions of the waveguide ensure that only single-modes are allowed to propagate. An embedded QD (red triangle) primarily emits in the guided TE_0 mode (green wave) due to having an in-plane dipole moment. Non-guided mode emission is suppressed due to total internal reflection.

This is an important feature, as the dipole moment of the QD is entirely in-plane and located in the middle layer of the waveguide. This enables a greatly enhanced coupling to the guided TE_0 mode, with a rate given by Γ_{wg}, and a suppressed decay rate to the leaky (non-guided) modes denoted Γ_{ng}. The coupling between emitter and guided modes is quantified by the β-factor (not to be confused with the propagation constant):

$$\beta = \frac{\Gamma_{wg}}{\Gamma_{wg} + \Gamma_{ng} + \Gamma_{nrad}}, \tag{2.15}$$

where Γ_{nrad} is the rate of intrinsic nonradiative recombination. Maximizing the β-factor is therefore highly desirable. For a dipole located near the center of the waveguide, and a dipole moment aligned with the electric field, β-factors can be as high as 95% [45].

2.2 The directional coupler

2.2.1 Photonic switches

The ability to route single photons between different quantum nodes is the cornerstone of wide range of reconfigurable QPICs. In such circuits, the essential building block is the switch, also known as the single photon router - in practice a tunable beamsplitter. Making complex quantum photonic architectures feasible means ensuring that the elementary switch features: compact footprints, short switching times, low optical losses, low power consumption and low driving voltages [46]. Most switching approaches, such as thermo-optic [47] and electro-optic [48], rely on altering the refractive index of the waveguide material in combination with Mach-Zender interferometers to facilitate switching. While they often show promising results in one or more key areas, it comes at the expense of poor performance in the others. Rapid developments in micro- and nano-electro-mechanical systems (MEMS/NEMS) in combination with optical integrated systems have in recent years lead to several novel switching devices of high performance. A novel switching approach, merging the research disciplines of deterministic photon-emitter interfaces and nano-opto-electromechanics (NOEMs), presents an elegant and efficient method of photon routing (pictured in fig. 2.5) [38]. The capabilities and promising potential of the core device component, namely the central tunable *directional coupler* (DC) found

in the NOEM switch, is in this work implemented to create new on-chip devices with different functions that are essential for QPICs. Therefore, an introduction to the working principles of the DC and underlying coupled-mode theory is given in the following.

2.2.2 The tunable beamsplitter

An illustration of the DC is pictured in fig. 2.5. It consists of two single-mode waveguides with a small gap in between. Being in close proximity to each other causes the guided modes of the two waveguides to couple (a complete description is given in section 2.2.3), leading to transfer of power between the two waveguides. This is the principle behind the DC (red dashed box in fig. 2.5). Control of the power transfer is achieved by attaching pairs of metal electrodes on slabs connected to both waveguides (dashed black box). Applying a voltage across these electrodes induces an attracting electrostatic force that pulls the central waveguides apart, altering the coupling between the modes. This allows to completely route light into either waveguides, as well as any power ratio in between (fx a 50:50 beamsplitter).

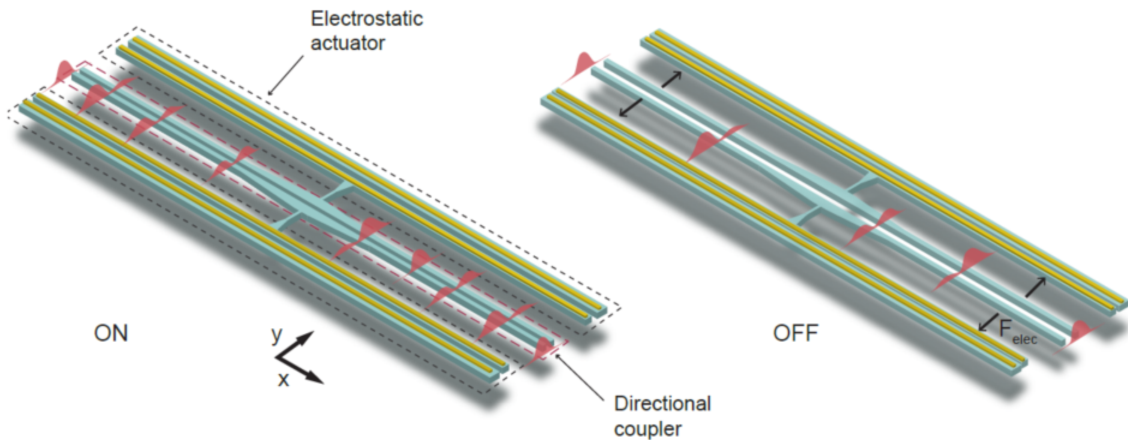

Figure 2.5: Illustration of the tunable beamsplitter. The guided modes of the waveguides couple evanescently, enabling a transfer of power. The power transfer can be reconfigured by applying a voltage across the electrodes, tuning the gap distance between the waveguides by electrostatic forces. Taken with permission from [49].

The displacement as a function of voltage is calculated by modelling the two electrodes as parallel plate capacitors exerting a force $F \propto V^2$, and finding the static solutions to Hooke's law $F = -ky$ [26]:

$$(d_0 - y)^2 y - \frac{V^2 \epsilon_0 L_s t}{2k_T} = 0, \tag{2.16}$$

where y is the waveguide displacement, t and d_0 are, respectively, the thickness and initial distance of the slabs on which the electrodes sit, V is the applied voltage, ϵ_0 the vacuum permitivity, L_s the length of the freely moving electrode, and k_T is the total stiffness of the system.

Equation 2.16 reveals two things about the DC. First, at voltages greater than

$$V_{PI} \geq \sqrt{\frac{8k_t d_0^3}{27\epsilon_0 L_s t}}, \tag{2.17}$$

no solution is found for eq. 2.16, meaning that the electrostatic force is greater than the restoring spring force, causing an irreversible pull-in of the electrodes, defining the maximal travel range possible. For typical device stiffness and dimensions used in this work, a pull-in voltage in the range of 10-15 V is typically found. Secondly, dy/dV increases with voltage, meaning that at low voltages, little tuning is to be expected, and vice-versa for high voltages. Setting the maximal applied voltage to around 9 V, corresponding to a displacement of around 40 nm for each actuator, therefore strikes a good balance between device performance and durability, and will be used in this work.

2.2.3 Introduction to coupled-mode theory

The previous section described the electro-mechanical coupling, and how applying a voltage to two electrostatic actuators leads to a displacement of the waveguides in the DC. This section will focus on deriving how varying the central gap distance affects the coupling of the guided modes in the two waveguides, and how this relates to the transfer of power. The system investigated is similar to that of fig. 2.5, where two parallel waveguides, waveguide 1 and 2, oriented along the x-direction and separated by a gap distance d, carry TE optical modes of free-space wavelength λ_0 (wave number $k = 2\pi/\lambda$). The waveguides are assumed to be loss-less and single-mode. Considering first the case where the two waveguides are isolated, their individual propagating modes then take the form:

$$\mathbf{E}_{1,2}(\mathbf{r}) = \mathbf{e}_{1,2}(y,z)e^{-i\beta_{1,2}x}, \tag{2.18}$$

where $\mathbf{e}_{1,2}$ are the fields of the two guided modes and $\beta_{1,2} = n_{1,2}k$ are the propagation constants in waveguide 1 and 2, respectively. Bringing the waveguides in close proximity to each other, coupled-mode theory [50] then describes how the evanescent tail of $\mathbf{E}_1$ extends to waveguide 2 and $\mathbf{E}_2$ to waveguide 1, introducing a perturbation. Under the assumption that this perturbation is small, the fields guided by the two coupled modes may be approximated by a linear combination of the two individual modes:

$$\mathbf{E}(\mathbf{r}) \approx a_1(x)\mathbf{e}_1(y,z)e^{-i\beta_1 x} + a_2(x)\mathbf{e}_2(y,z)e^{-i\beta_2 x} \tag{2.19}$$

where the two amplitude functions, $a_1(x)$ and $a_2(x)$ have been introduced. The evolution of the amplitude functions are given by the *coupled-mode equations* [51]:

$$\begin{aligned} \frac{da_1(x)}{dx} &= -ig_{21}a_2(x)e^{-i\delta x}, \\ \frac{da_2(x)}{dx} &= -ig_{12}a_1(x)e^{-i\delta x}. \end{aligned} \tag{2.20}$$

Here, the phase mismatch $\delta = \beta_2 - \beta_1$ and the coupling coefficients g_{21} and g_{12} have been introduced. The coupling coefficient g_{21} is given by the overlap integral of the evanescent tail of waveguide 2 and the guided mode of waveguide 1, and vice-versa for g_{12}. For symmetric waveguides, it is assumed that $g_{21} = g_{12} = g$ due to energy conservation. As light couples evanescently, the coupling factor g is expected to follow an exponential dependence on the distance [42]:

$$g = g_0 e^{-\kappa d} \tag{2.21}$$

with g_0 being a constant that depends exclusively on the properties of the isolated waveguides, and κ being the *photonic tunneling constant* of the evanescent mode in the gap region. Equation 2.21 shows directly the relation between waveguide coupling and gap distance. At this point it becomes useful to switch to an alternative view, in which the two waveguides are treated as a single system with two orthogonal (normal) modes which do not couple. The fields of the normal modes of this composite waveguide system are derived by rewriting the coupled-mode equations (eq. 2.20) with the introduction of $A_{1,2}(x) = a_{1,2}(x)e^{-i\beta x}$:

$$\frac{d}{dx}\begin{bmatrix} A_1(x) \\ A_2(x) \end{bmatrix} = -i \begin{bmatrix} \beta & g \\ g & \beta \end{bmatrix} \begin{bmatrix} A_1(x) \\ A_2(x) \end{bmatrix}. \tag{2.22}$$

The matrix M can be decomposed to:

$$M = \begin{bmatrix} \beta & g \\ g & \beta \end{bmatrix} = SDS^{-1} \tag{2.23}$$

where S is a matrix composed of eigenvectors of M, and D is the diagonal matrix constructed from the corresponding eigenvalues. They are:

$$S = \begin{bmatrix} 1 & 1 \\ 1 & -1 \end{bmatrix}, \; D = \begin{bmatrix} \beta + g & 0 \\ 0 & \beta - g \end{bmatrix}, \; S^{-1} = \begin{bmatrix} 1/2 & 1/2 \\ 1/2 & -1/2 \end{bmatrix}. \tag{2.24}$$

By inserting eq. 2.23 into 2.22, the basis is changed from the individual waveguide system to the combined waveguide system:

$$\frac{d}{dx} S^{-1} \begin{bmatrix} A_1(x) \\ A_2(x) \end{bmatrix} = -iDS^{-1} \begin{bmatrix} A_1(x) \\ A_2(x) \end{bmatrix}, \tag{2.25}$$

In this basis, two normal modes can propagate in the DC: a *symmetric mode* and *anti-symmetric*, given by:

$$\begin{bmatrix} A_S(x) \\ A_{AS}(x) \end{bmatrix} = S^{-1} \begin{bmatrix} A_1(x) \\ A_2(x) \end{bmatrix} = \frac{1}{2} \begin{bmatrix} A_1(x) + A_2(x) \\ A_1(x) - A_2(x) \end{bmatrix}. \tag{2.26}$$

Solving eq. 2.25 shows that these normal modes propagate according to their propagation constants:

$$\beta_{S,AS} = \beta \pm g. \tag{2.27}$$

The symmetric and anti-symmetric modes can be written in terms of the modes of the individual waveguides:

$$\begin{aligned} a_S e^{-i\beta_S x} &= \frac{1}{2}\left(a_1 e^{-i\beta x} + a_2 e^{-i\beta x}\right), \\ a_{AS} e^{-i\beta_{AS} x} &= \frac{1}{2}\left(a_1 e^{-i\beta x} - a_2 e^{-i\beta x}\right), \end{aligned} \tag{2.28}$$

Figure 2.6.a illustrates how the evanescent tails of the individual waveguides fields combine either in or out of phase to create the symmetric and anti-symmetric normal modes, respectively.

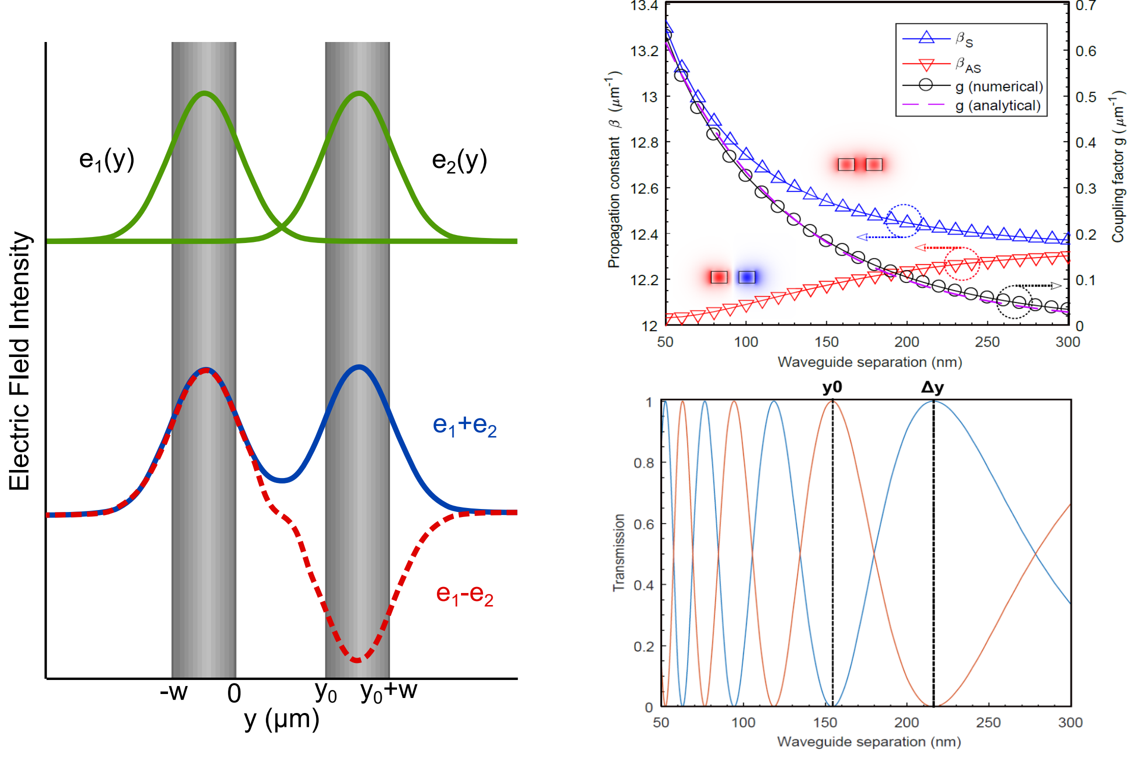

Figure 2.6: Properties of the DC. a. Field profiles of the modes in the DC. The guided modes of the individual waveguides (green) couple to form the symmetric (blue) and anti-symmetric (red dashed) normal modes. **b.** Numerical analysis with suitable parameters yield values for the propagation constants β_S and β_{AS} of the normal modes, as a function of waveguide displacement. The right axis show values for the coupling factor g, found both numerically (black circles) by $2g = \Delta\beta$ and analytically by fitting eq. 2.21 (purple dashed line), showing good agreement. **c.** Transmission at the two output ports of the DC as a function of waveguide displacement. The dashed lines illustrate the switching distance Δy required to achieve full switching from an initial gap distance of y_0. Figures **b.** and **c.** are taken with permission from [38].

The amplitudes of the fields in the individual waveguides can similarly be written in the basis of the normal modes:

$$a_{1,2}e^{-i\beta x} = \frac{1}{2}\left(a_S e^{-i\beta_S x} \pm a_{AS} e^{-i\beta_{AS} x}\right). \tag{2.29}$$

In this picture, the power transfer between the two waveguides can be understood as the two normal modes of the composite waveguide system interfering due to the mismatch of their propagation constants. The intensity for the two waveguide modes can be written as:

$$I_1 = I_0 \sin^2\left(\frac{\beta_S - \beta_{AS}}{2}x\right) = I_0 \sin^2(gx), \tag{2.30}$$

$$I_2 = I_0 \cos^2\left(\frac{\beta_S - \beta_{AS}}{2}x\right) = I_0 \cos^2(gx), \tag{2.31}$$

where I_0 is the initial intensity introduced to the DC. Consequently, $g = \frac{\beta_S - \beta_{AS}}{2} = \frac{\Delta\beta}{2}$. Numerical simulations of the propagation constants of the modes in the DC allows for the extraction of $g(y_0, \lambda_0)$ and a value of $g_0(\lambda_0)$ by fitting the model of eq. 2.21. The waveguide parameters used for the simulations are similar to those used in this work, with widths $w = 200$ nm, thicknesses $t = 160$ nm, and refractive indices $n = 3.48$ (GaAs). It is here worth noting that decreasing the waveguide width would in fact lead to greater coupling between the waveguides, but at the cost of more scattering losses and less robust structures. The results of the simulation are plotted for $\lambda_0 = 940$ nm in fig. 2.6.b, and fig. 2.6.c shows the dependence of I_1 and I_2 on the waveguide separation. The distance along the coupler after which power has been transmitted completely from one waveguide to the other is denoted the *transfer length*, given by:

$$L_t = \frac{\pi}{2g} = \frac{\pi}{\Delta\beta}, \tag{2.32}$$

which allows the intensity through one port to be expressed as:

$$I_1 = I_0 \sin^2(\frac{\pi}{2L_t}x). \tag{2.33}$$

Thus, for a DC with fixed coupling length L_c, varying the waveguide separation changes g and therefore L_t, altering the power transfer between the two waveguides. To achieve full switching from one waveguide to the other requires a $\pi/2$ shift in the argument of eq. 2.33, corresponding to a *switching displacement* of:

$$\Delta y = \frac{1}{\kappa}\frac{1}{\frac{L_c}{L_{t0}}e^{-\kappa y_0} - 1}, \tag{2.34}$$

as a function of the gap distance at rest y_0. An example of possible values of y_0 and Δy is shown in fig. 2.6.c.

2.3 Novel NOEM-based devices

The NOEM DC introduced in section 2.2.2 constitutes a novel approach to photon routing which can be integrated directly with single-photon sources such as InGaAs QDs, and operated at QD compatible cryogenic temperatures. Full switching can be achieved at 10 V, with a maximal power transfer of $(99.5/0.5 \pm 0.2)$ %, insertion loss of 0.67 dB and a response time below 1 µs. However, while the photon router is instrumental to a great range of QPICs, realizing complex quantum processing applications with single photons requires advances in the performance and efficiency of other devices in the QPIC toolbox, such as an integrated mirror with reconfigurable reflectivity, and an integrated phase shifter to control the spontaneous emission of a QD (as was depicted in fig. 2.2). In this chapter, two novel devices based on the NOEM DC are introduced: a tunable NOEM mirror and a tunable NOEM phase shifter. Proposed designs for these devices are shown in fig. 2.7.a and 2.7.b, and their working principles is presented in 2.7.c. These devices benefit from the same efficiency as the photonic switch, but can be integrated and combined to form

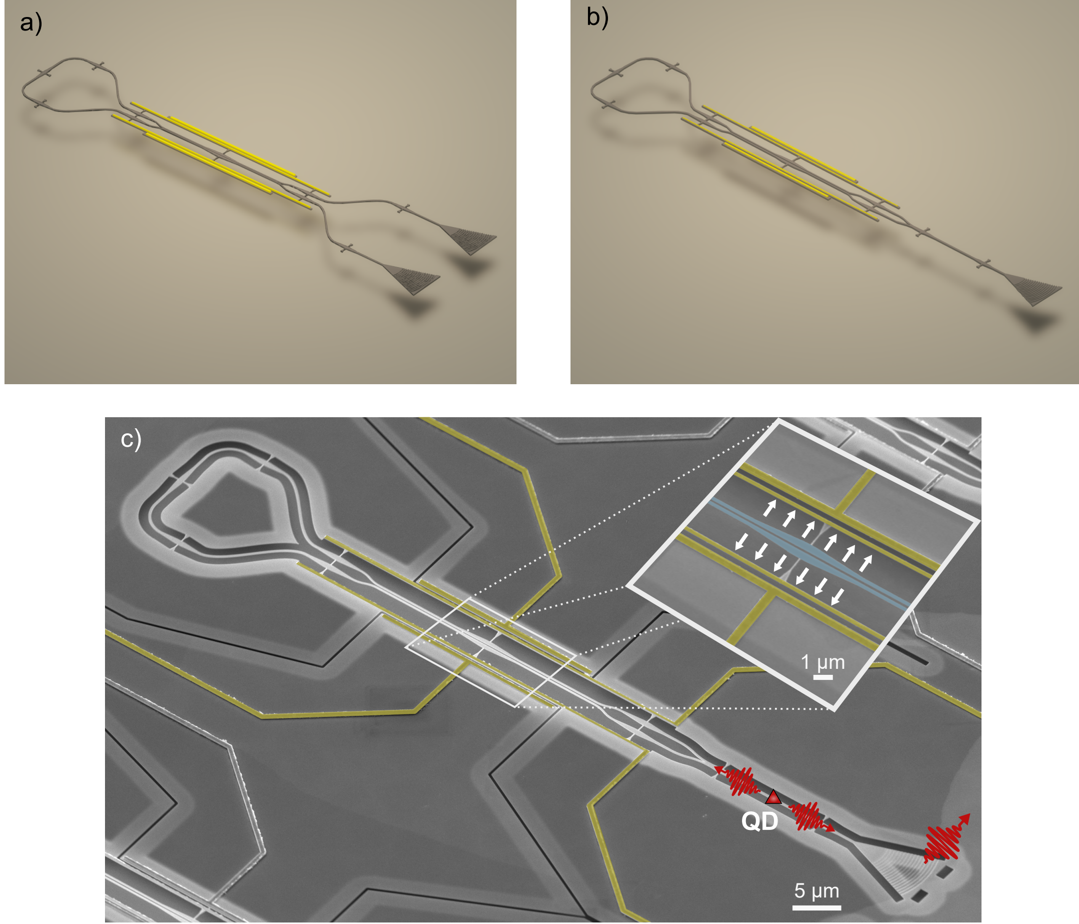

Figure 2.7: Proposed NOEM-based devices. a. 3D rendering of the proposed tunable NOEM mirror. **b.** 3D rendering of the proposed tunable NOEM phase shifter. **c.** False-color SEM of a fabricated NOEM phase shifter, highlighting the working principle of the devices. Here, the emission of an embedded QD (red triangle) can be tuned via the electro-mechanical coupling in the central DC, shown in the inset. Electrodes are highlighted in yellow, and the mechanical motion of the waveguides, highlighted in blue, is indicated by the white arrows.

numerous advanced quantum architectures, and aid in solving key issues that are currently limiting the development of QPICs. The capabilities and possible uses of these devices are described in detail below. Although these devices may seem similar, they provide very different functions, and will therefore be treated separately throughout this work. In the following, a thorough derivation of the *S-matrix* formalism is presented. This method, used in many branches of quantum physics, is here implemented to derive basic principles of these photonic nanostructures.

2.3.1 S-matrix formalism

The *scattering matrix*, or S-matrix, is a powerful technique to describe the relation between the initial and final states of a system undergoing scattering. It is used in several branches of physics, including quantum field theory, network theory and optics.

In its most general form, the S-matrix is given by [52]:

$$\boldsymbol{\Psi}_{\text{out}} = \boldsymbol{S}\boldsymbol{\Psi}_{\text{in}} \tag{2.35}$$

For optics, it can be used to relate the amplitudes and phases of waves *exiting* a system in terms of those *entering* the system. For an N-port device, the S-matrix will be a $N \times N$ *unitary* matrix, such that $\boldsymbol{S}^{\dagger}\boldsymbol{S} = 1$. That the S-matrix is unitary ensures that the current density is conserved throughout the system. For instance, a two-port system as the one depicted in fig. 2.8.a, where light can go in or out of two separate ports (labelled port 1 and 2), the corresponding S-matrix is a 2x2 matrix:

$$\begin{bmatrix} b_1 \\ b_2 \end{bmatrix} = \begin{bmatrix} S_{11} & S_{12} \\ S_{21} & S_{22} \end{bmatrix} \begin{bmatrix} a_1 \\ a_2 \end{bmatrix}, \tag{2.36}$$

where inherently $|S_{11}| = |S_{22}|$ and $|S_{12}| = |S_{21}|$. As an example, only injecting a field into port 1 gives the equations: $b_1 = S_{11}a_1$, and $b_2 = S_{21}a_1$. If light was injected into both ports, the equations would contain a contribution from both a_1 and a_2.

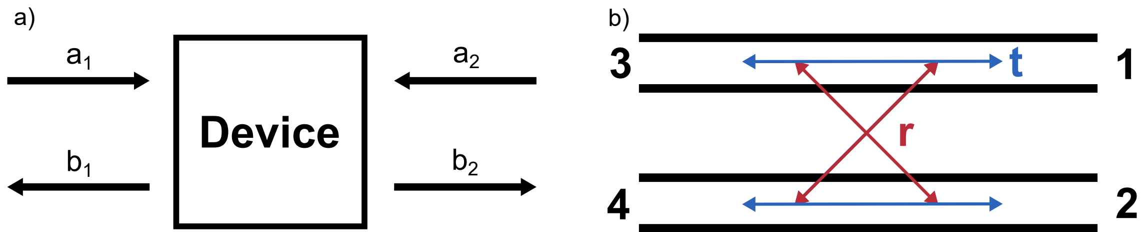

Figure 2.8: General two-port device and directional coupler. a. The outgoing fields b_1 and b_2 in a general two-port device are related to the input fields a_1 and a_2 by the S-matrix. **b.** An accurate S-matrix can be constructed by modelling the DC as a four-port beamsplitter. The transmission (reflection) coefficient t (r) represents transmitted (reflected) waves in the system.

This leads to an intuitive understanding of the specific S-matrix parameters: the matrix element $S_{i,j}$ directly relates the field exiting port i to that entering port j. For $i = j$, the parameter describes the fields that are reflected, and for $i \neq j$ describes fields that are transmitted. In this same picture, the field intensity between ports can be related by:

$$I_i = |S_{ij}|^2 I_j, \tag{2.37}$$

where $0 \leq |S_{ij}|^2 \leq 1$ is the intensity fraction of the field exiting port i compared to that entering port j. The S-matrix is thus an effective yet simple tool to describe a multitude of devices, including photonic structures. Modelling the DC introduced in section 2.2.2 as a simple tunable beamsplitter, light can either be transmitted (same waveguide) or reflected to the cross-port (opposite waveguide), with probabilities given by the transmission and reflection coefficient $|t|^2$ and $|r|^2$, respectively. This is illustrated in fig. 2.8.b.

Assuming a lossless system and ignoring any overall phase, the S-matrix for the DC becomes:

$$S_{dc} = \begin{bmatrix} 0 & 0 & t & -ir \\ 0 & 0 & -ir & t \\ t & -ir & 0 & 0 \\ -ir & t & 0 & 0. \end{bmatrix}. \quad (2.38)$$

As t and r are in this case both real numbers, a factor of $-i$ has been added to the cross-port to include information on the phase [53]. Due to the constraint on the coefficients: $|r|^2 + |t|^2 = 1$, the reflection coefficient can be written in terms of the transmission coefficient as $|r| = \sqrt{1 - |t|^2}$. These coefficients can also be written in terms of the parameters of the actual system. The diagonal matrix from eq. 2.24 is rewritten in an exponential form to define a new matrix J, describing the propagation of the normal modes through a length x:

$$J = e^{-iDx} = \begin{bmatrix} e^{-i\beta_S x} & 0 \\ 0 & e^{-i\beta_{AS} x} \end{bmatrix}. \quad (2.39)$$

Substituting this matrix in place of the diagonal matrix in eq. 2.23, and replacing x with L_c, a new matrix T is constructed:

$$T = SJS^{-1} = \frac{1}{2} \begin{bmatrix} e^{-i\beta_S L_c} + e^{-i\beta_{AS} L_c} & e^{-i\beta_S L_c} - e^{-i\beta_{AS} L_c} \\ e^{-i\beta_S L_c} - e^{-i\beta_{AS} L_c} & e^{-i\beta_S L_c} + e^{-i\beta_{AS} L_c} \end{bmatrix}. \quad (2.40)$$

The elements of the matrix T describes a propagation of length L_c for the modes of the coupled waveguides in terms of the normal modes. Because of this, they can be related to the coefficients t and r by:

$$T = \begin{bmatrix} t & -ir \\ -ir & t \end{bmatrix}. \quad (2.41)$$

The coefficients are therefore:

$$t = \frac{1}{2} \left(e^{-i\beta_S L_c} + e^{-i\beta_{AS} L_c} \right) \quad (2.42)$$

and similarly

$$r = \frac{i}{2} \left(e^{-i\beta_S L_c} - e^{-i\beta_{AS} L_c} \right). \quad (2.43)$$

By using the above equations, the exact device parameters can be incorporated into the S-matrix of the DC (eq. 2.38). S-matrices for individual systems can be combined to describe more complex, composite systems, using the *cascading junctions* method from network theory. A derivation of the method of cascading S-matrices is given in appendix A. In the following, this method will be applied to describe the operating principle and ideal-case performance of the NOEM mirror and NOEM phase shifter.

2.3.2 Tunable NOEM mirror

In the DC introduced in section 2.2.2, light injected into one waveguide will, after the coupling length L_c, either stay in the same waveguide, or cross over to the other, the ratio of which can be controlled by varying the gap separation. A *Sagnac loop mirror* [54] can be created by introducing a nano-beam waveguide loop that connects the two waveguide ends. Light exiting the waveguides is thus guided through the loop and sent through the DC a second time, where the normal modes of the DC interfere once more, and light is transmitted to one of the two remaining ports. Similar to the NOEM switch, when injecting light into one port, the ratio of light that is transmitted can be controlled by varying the gap-distance. The two extremities are then either full reflection, or full transmission. This device, illustrated in fig. 2.9.a, is thus effectively a mirror with a tunable reflectivity, as is indicated in fig. 2.9.b.

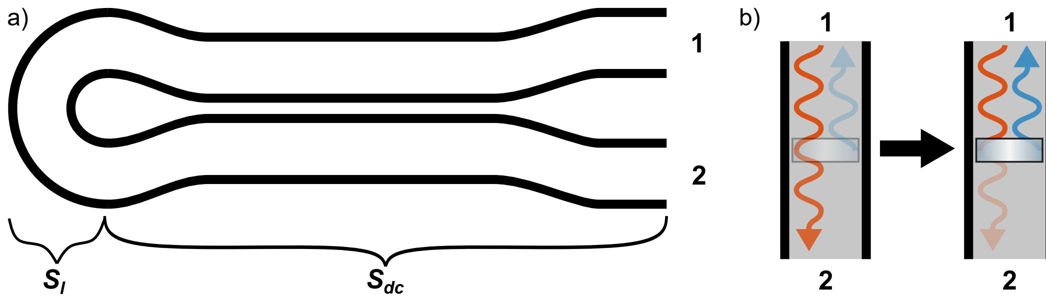

Figure 2.9: Schematic of the NOEM mirror. a. Schematic of the device. The S-matrix for the NOEM mirror is constructed by cascading the S-matrices of the loop and the DC, leaving only port 1 and 2. **b.** Conceptual view of the tunable mirror. The idea of the NOEM mirror is similar to placing a mirror with adjustable reflectivity between port 1 and 2.

This *tunable NOEM mirror* can be fabricated directly on-chip, is operable at cryogenic temperatures, and can be directly integrated with QD single-photon sources. Mirrors are often of interest for the construction of optical cavities that enhance the radiative decay rate of a contained emitter by a factor $F_p \propto \frac{Q}{V_m}$, where Q denotes the cavity quality factor, and V_m is the cavity mode volume [55]. Transmission out of a cavity T to a coupled waveguide also depends on the Q-factor by:

$$T = \frac{(Q_i - Q)^2}{Q_i^2} \tag{2.44}$$

where $1/Q = 1/Q_i + 1/Q_c$ is the waveguide-loaded Q-factor, and Q_i and Q_c are the intrinsic and coupled Q-factors of the cavity, respectively [56]. State-of-the-art GaAs photonic-crystal-based cavities containing a single QD can achieve quality factors as high as $Q = 1.6 \cdot 10^5$, with sub-wavelength mode volumes [57]. The properties of such a cavity are however fixed upon fabrication. A cavity constructed by a pair of the proposed NOEM mirrors, or perhaps a photonic-crystal reflector and NOEM mirror, would facilitate tuning of the Q-factor. The Purcell enhancement and transmission can in this way be controlled, in order to find an optimal trade-off for the experiment at hand.

NOEM mirror S-matrix

The S-matrix for the NOEM mirror can be constructed by cascading the S-matrix of the DC (eq. 2.38) and that of a waveguide loop, as indicated in fig. 2.9.a. The latter can simply be written:

$$S_l = \begin{bmatrix} 0 & e^{i\phi} \\ e^{i\phi} & 0 \end{bmatrix} \tag{2.45}$$

where the loop is similarly assumed to be lossless. The propagation phase ϕ is assumed to be equal for both directions and can be set to $\phi = 0$. Using the theory of cascading junctions, the resulting S-matrix for the combined mirror system, S_m, becomes:

$$S_m = \begin{bmatrix} -2itr & t^2 - r^2 \\ t^2 - r^2 & -2itr, \end{bmatrix} \tag{2.46}$$

where $|S_{11,22}|^2 = 4|tr|^2$ and $|S_{12,21}|^2 = |t^2 - r^2|^2$ are the intensity ratios corresponding to light that is transmitted and reflected when injected into one of the two ports, respectively. Figure 2.10.a plots the intensity ratios corresponding to reflection and transmission through the mirror as a function of $|t|^2$. Inserting eq. 2.42 and 2.43

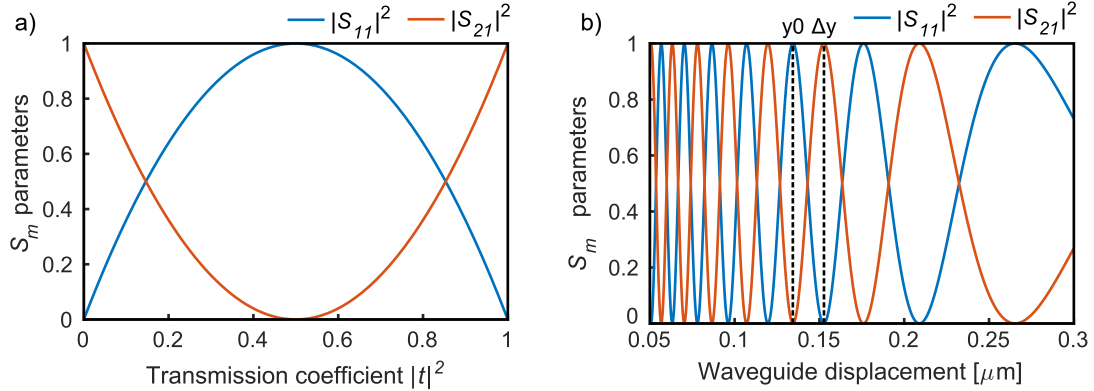

Figure 2.10: S-matrix analysis of the NOEM mirror. a. Transmission and reflection in the mirror as a function of the transmission coefficient, given by the S-matrix model. Light entering port 1 can either be reflected (blue curve) or transmitted to port 2 (orange curve), with a ratio dependent on the configuration of the beamsplitter. **b.** Same as a., but as a function of DC gap distance. By using values from numerical simulations of the DC, the S-matrix model shows that the tuning behaviour of the mirror is similar to the DC (here for reflection and transmission), but with a switching displacement that is halved.

into S_m and using values from numerical simulations for $\lambda_0 = 940$, the S-matrix parameters can be expressed entirely in terms of the waveguide separation d, as presented in fig. 2.10.b. The values used match those for the numerical simulations of the DC presented in fig. 2.6.c, inviting a comparison between the two. The NOEM mirror displays a similar "switching" behaviour, but with a switching displacement Δy that is halved. This is to be anticipated, as light in the NOEM mirror passes through the central DC twice, in principle doubling its effect.

2.3.3 Tunable NOEM phase shifter

By merging the two out-coupling ports of the NOEM mirror, a new, single-port device is constructed. In the resulting device, illustrated in fig. 2.11.a, the intensity of light is unchanged (assuming a lossless system), but will experience a change of phase. The phase change is a combination of a propagation phase and the phase change induced by the DC. The former is fixed for a given device, but the latter can be altered by changing the coupling in the DC, i.e. by varying the waveguide separation. This is the *tunable NOEM phase shifter*. An intuitive understanding of this device is realized by comparing it to a mirror that can be spatially shifted forwards and backwards, changing the spatial distribution of the vacuum electric field, as indicated in fig. 2.11.b.

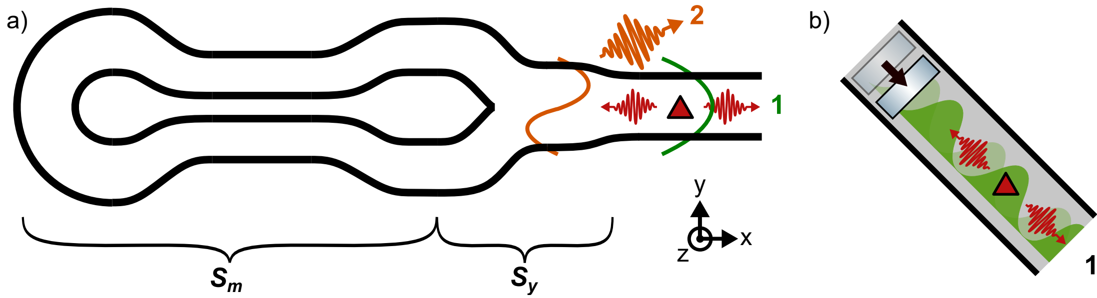

Figure 2.11: Schematic of the NOEM phase shifter. a. Schematic of the device. The S-matrix for the NOEM phase shifter is constructed by cascading the S-matrices of the mirror and a y-splitter structure. A second port is included to account for a higher-order mode that is tapered out. **b.** Conceptual view of the tunable phase shifter. The idea of the NOEM phase shifter is similar to a movable mirror in the waveguide. When moved, the surrounding vacuum electric field (green curves) surrounding the QD (red triangle) changes, enhancing its spontaneous emission rate.

In the single-mode waveguide near the out-coupler, two sinusoidal TE waves thus propagate in opposite directions, with electric fields oriented in the y-direction [42]:

$$\begin{aligned} E_1(x) &= \mathrm{Re}[E_{1,y}e^{-i\beta x}] = E_{1,y}\cos(\beta x), \\ E_2(x) &= \mathrm{Re}[E_{2,y}e^{+i(\beta(x+\Delta x)+\phi)}] = E_{2,y}\cos(\beta(x+\Delta x)+\phi), \end{aligned} \tag{2.47}$$

where Δx is an arbitrary propagation length difference, and $E_{1,y}$ and $E_{2,y}$ are the amplitudes of the two waves, which for a lossless system $E_{1,y} = E_{2,y}$. The factor ϕ is here the phase change induced by the DC. The total field is then a superposition of the two fields:

$$E(x) = E_1(x) + E_2(x) = E_{1,y}\cos(\beta x) + E_{2,y}\cos(\beta(x+\Delta x)+\phi). \tag{2.48}$$

Changing the phase thus changes the spatial distribution (or amplitude at a fixed position) of the standing wave. This is the case not only for light propagating through the device, but also for the vacuum fluctuation field introduced in section 2.1.3. Equations 2.11, 2.12 and 2.14 described how the radiative decay rate and radiated power of an emitter depends on the vacuum fluctuation field through the

LDOS, where the spatial field distribution enters as $\rho(\mathbf{r}_0, \mathbf{e}_\mathbf{r}, \omega_0) \propto |E_\mathbf{k}|^2$. The tunable NOEM phase shifter therefore constitutes a powerful approach to modifying the emission properties of a QD single photon source located in a waveguide, where the surrounding vacuum fluctuation field is tailored to control the LDOS.

An issue with QD single-photon sources is that a QD emitting into a waveguide mode will have an equal probability to emit into either waveguide direction. As further photon processing or detection devices are usually located on only one side of the emitter, this effectively constitutes a loss of 50%. One solution is to fabricate a photonic-crystal Bragg mirror on one side of the emitter reflecting photons emitted in the wrong direction, but this also induces the unwanted effect of an uncontrollable phase change altering the LDOS, and subsequently the decay rate of the emitter. In the worst case, emission from the QD is completely suppressed. The tunable NOEM phase shifter can however account for this by controlling the phase, thereby enabling control of the spontaneous emission of the QD.

NOEM phase shifter S-matrix

The NOEM phase shifter S-matrix can be constructed by combining the S-matrix for the mirror, calculated in eq. 2.46, with that of a y-splitter. A y-splitter is a nanostructure that merges two parallel waveguides into one, as shown in fig. 2.11.a. While it intuitively resembles a three port device, a fourth port must be included to account for a higher-order mode that is tapered out, and to ensure a unitary S-matrix. The corresponding S-matrix is:

$$S_y = \begin{bmatrix} 0 & 0 & 1/\sqrt{2} & 1/\sqrt{2} \\ 0 & 0 & 1/\sqrt{2} & -1/\sqrt{2} \\ 1/\sqrt{2} & 1/\sqrt{2} & 0 & 0 \\ 1/\sqrt{2} & -1/\sqrt{2} & 0 & 0 \end{bmatrix} \tag{2.49}$$

Combining the S-matrices for the mirror and y-splitter structures creates the phase shifter S-matrix S_{ps}:

$$S_{ps} = \begin{bmatrix} -(r+it)^2 & 0 \\ 0 & (it-r)^2 \end{bmatrix}. \tag{2.50}$$

The only parameter of importance is here S_{11}, corresponding to the first-order mode entering and exiting the single out-coupler. The phase change is given by the argument of this parameter, and can be found by inserting t and r:

$$\phi = 2\beta_S L_c. \tag{2.51}$$

It is worth noting that the phase change only depends on β_S, as opposed to the tuning of the NOEM mirror, which depends on both β_S and β_{AS}.

Figure 2.12.a shows the phase change as a function of gap distance in the DC, using values from numerical simulations. Figure 2.12.b shows the corresponding change of the vacuum fluctuation field amplitude at a fixed position. As the device is assumed to be lossless, the intensity ratio is simply $|S_{ps,11}|^2 = (r^2+t^2)^2 = 1$. However, losses in the reflected wave incorporated by $E_{2,y}$ in eq. 2.48 are detrimental to the performance of the device. This is illustrated in fig. 2.12.b, where several values of $E_{2,y}$ as fractions of $E_{1,y}$ are plotted.

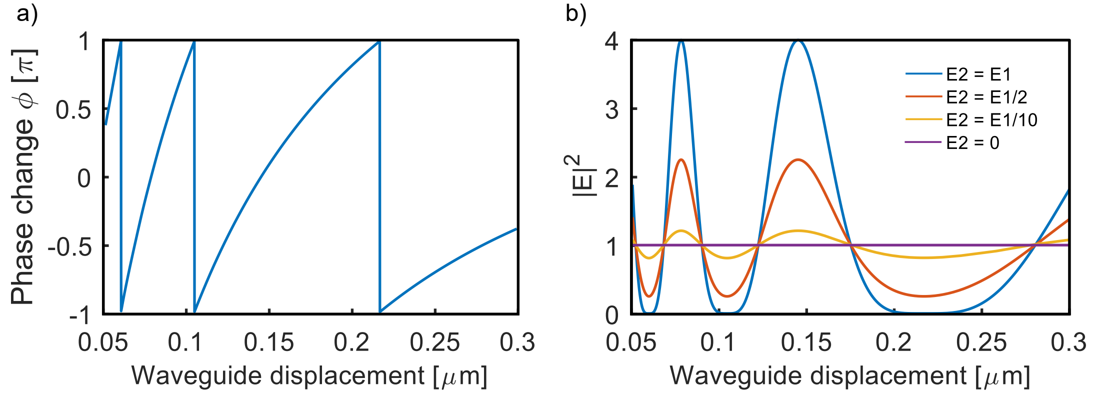

Figure 2.12: S-matrix analysis of the NOEM phase shifter. a. Tuning of the phase as a function of DC gap distance, given by the S-matrix model. Light entering and exiting port 1 experiences a phase shift determined by the waveguide displacement in the DC. **b.** Vacuum electric field amplitude at the position of a QD as a function of DC gap distance. The S-matrix model shows that the change in phase effectively tunes the amplitude of the vacuum electric field. The tuning is plotted for different device losses, highlighting its importance for the performance of the device.

The contrast between the maximum and minimum attainable values can be quantified by the extinction ratio (ER), given in dB as:

$$ER = 10 \log_{10} \left(\frac{P_{max}}{P_{min}} \right). \tag{2.52}$$

P_{max} (P_{min}) is the maximum (minimum) value, in this case given in terms of optical power. As is evident from fig. 2.12.b, losses are expected to inhibit the obtainable ER for the NOEM phase shifter, and should therefore be minimised.

Chapter 3

Fabrication of NOEM devices

Microscale devices with electrically controllable parts, also known as micro-electro-mechanical systems (MEMS), as well as their nanoscale counterpart, nano-electro-mechanical systems (NEMS), are mature technologies that have already found success employed in a wide range of modern day applications, such as in smartphone sensors and printer heads [58, 59]. Specifically NEMS have recently become a subject of great interest in the field of optics and photonics (NOEMS), as confining electromagnetic fields to sub-micrometre dimensions allows for controlling light efficiently with high speed and low power consumption [26]. NOEMS offer unprecedented versatility, as they can be fabricated on numerous material platforms, most notably silicon, silicon-on-insulator, and III-V semiconductors such as GaAs. Examples of NOEMS fabricated on different platforms are presented in fig. 3.1.

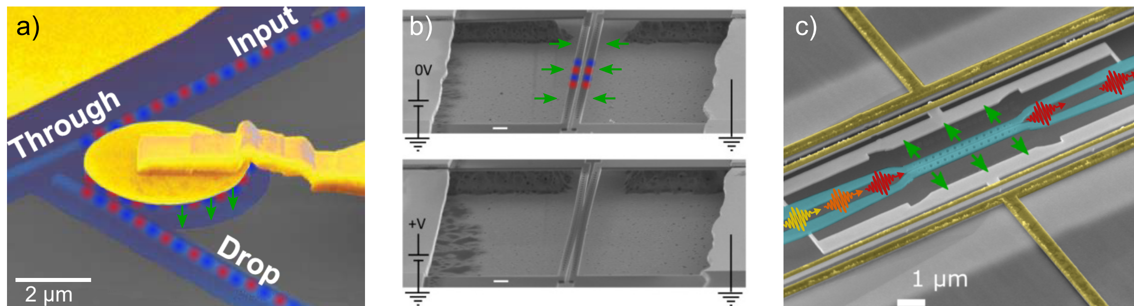

Figure 3.1: False-color SEMs of NOEMS examples. a. Optical switch based on a plasmonic resonator controllable by electrostatic actuation, fabricated on silicon. The switched optical field is overlaid. **b.** A programmable photonic crystal cavity made of two electrostatically actuated nanobeams, fabricated on silicon-on-insulator. The optical field of the confined cavity mode has been overlaid. **c.** Reconfigurable nano-mechanical single-photon filter, fabricated on GaAs. Electro-mechanical deformation of the coupled nanobeam photonic crystal cavity allows for filtering of single-photons. The green arrows indicate the direction of actuation in all figures. Adapted from: ref. [46] **a.**; ref. [60] **b.**; ref. [56] **c.**

Silicon is a platform of particular interest, as it has been the staple of semiconductor electronics for decades, and promises efficient integration of silicon optical circuits with existing complementary-metal-oxide-semiconductor (CMOS) electronics [46]. However, QD emitters grown on silicon suffer from a low radiative rate due to the indirect energy band gap of silicon [61]. Conversely, a direct band gap semiconductor such as GaAs seamlessly integrates with highly radiative QD single-photon sources, and is therefore the material platform of choice in this work. Regardless of the chosen material platform, MEMS/NEMS can be fabricated using techniques that fall into one of two categories. When fabricating MEMS/NEMS devices, mainly *bulk machining* techniques are used, where structures are defined by selectively removing or etching into the substrate. Conversely, additive techniques that deposit material on the surface of the substrate, are known as *surface machining* techniques, and are also used in certain steps of the MEMS/NEMS fabrication process. A general recipe for MEMS/NEMS fabrication consists of the following overall steps:

1. Metal deposition and lift-off
2. Etching of shallow-etched gratings (SEG)
3. Etching and undercut of photonic structures
4. Finishing cleaning and drying procedure

which are shown in fig. 3.2.b. In this chapter, these processes are described generally, starting with an introduction to the growth of the GaAs wafers used in this work, and an overview of the essential method of electron-beam lithography. The exact recipe used in this work is given in appendix B.

3.1 Sample growth

In this work, undoped GaAs wafers with embedded InAs quantum dots are used, similar to that illustrated in fig. 3.2.a. Since GaAs is a compound semiconductor, more specifically a III-V semiconductor, more care is required in the growth process compared to elementary semiconductors such as silicon. By using an epitaxial method such as molecular-beam epitaxy, compound semiconductors can be grown layer by layer with extreme purity, layer thickness control and material composition control [40]. In MBE, a semiconductor wafer is placed in a ultra-high vacuum chamber, with pressures as low as 10^{-10} to 10^{-11} mbar, and is heated to a temperature between 500°C to 600°C. Atoms evaporated from heating crucibles, known as effusion cells, are directed to the substrate, where they stick to the surface and diffuse until they find the energetically most favorable position in the crystal lattice. The flux of atoms can be controlled by shutters in front of the effusion cells, allowing for precise control of the material composition. In the case of GaAs, both shutters are open, and the flux is controlled by the temperature of the crucible. Under the right conditions, the crystal is grown atomic layer by atomic layer, which can be monitored by scattering an electron beam off the surface of the crystal, and observing the resulting diffraction pattern. The precise control of the layer-by-layer growth allows for the introduction of different materials on the crystal, with very sharp interfaces.

This could for example be the introduction of InAs layers on a GaAs crystal. Intially, the InAs grows layer-by-layer, but due to the 7 % mismatch between the lattice constants of InAs and GaAs, strain is generated around the interface. Increasing the top layer thickness, the strain is eventually released in the form of small islands [39], which are the QD's that were introduced in 2.1.1. This is shown in the zoom-in of fig. 3.2.a. This method of growth is known as the Stranski-Krastanov method.

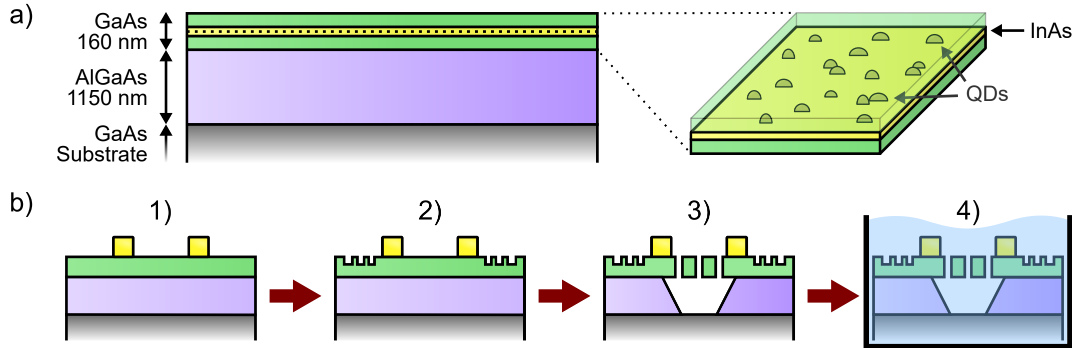

Figure 3.2: Undoped quantum dot wafer and general MEMS/NEMS fabrication process. a. An undoped wafer with a layer of InGaAs QDs embedded in the top GaAs membrane. The QDs are randomly distributed, but an even QD density is achieved by substrate rotation during growth. **b.** A general process used for fabricating many NEMS/MEMS devices. Specific steps are explained in the main text.

For the wafers used in this work, an 1150-nm thick sacrificial layer of $Al_{0.77}Ga_{0.23}As$ is initially grown on top of a GaAs substrate. This layer is removed in the final steps in order to suspend the photonic structures. The thickness of this layer is important for the performance of the fabricated devices, as will be elaborated in section 3.3.2. A 160-nm GaAs membrane with a layer of InAs QD's in the center is subsequently deposited. In order to achieve a uniform density of QDs over the surface of the wafer, the QD's are grown with rotation. The wafers can be cleaved into smaller chips, depending on the size limitation of the experimental setup. The wafers used in this work were grown by the group of Professor Andreas D. Wieck at Bochum University, and their method for growing InAs QDs can be found in ref. [62].

3.2 Electron-beam lithography

A schematic of the devices to be fabricated is known as a *mask*. Transfer of the patterns that constitute the devices from mask to wafer can be achieved with lithographic methods such as optical lithography and electron-beam lithography. Lithography is a crucial part of many steps in the fabrication process, not only when fabricating NEMS devices, but indeed any devices containing features with critical dimensions on a micro/nanometer scale. In many cases, electron-beam lithography (EBL) is preferred to optical lithography, as the resolution of optical lithography is limited by the diffraction of light, while EBL can produce patterns down to nanometers in size. Figure 3.3.a shows a simplified illustration of the working

principle EBL-system. With EBL, a pattern is written unto a thin organic polymer film known as a *resist* by a focused beam of electrons. As the resist is sensitive to electrons, exposing the surface with an electron beam will transfer energy to the polymer chains of the resist, changing its solubility. When immersed in a special developer, either the exposed part (positive resist) or unexposed part (negative resist) is removed, creating a mask that can be utilized for subsequent processing, as shown in fig. 3.3.b.

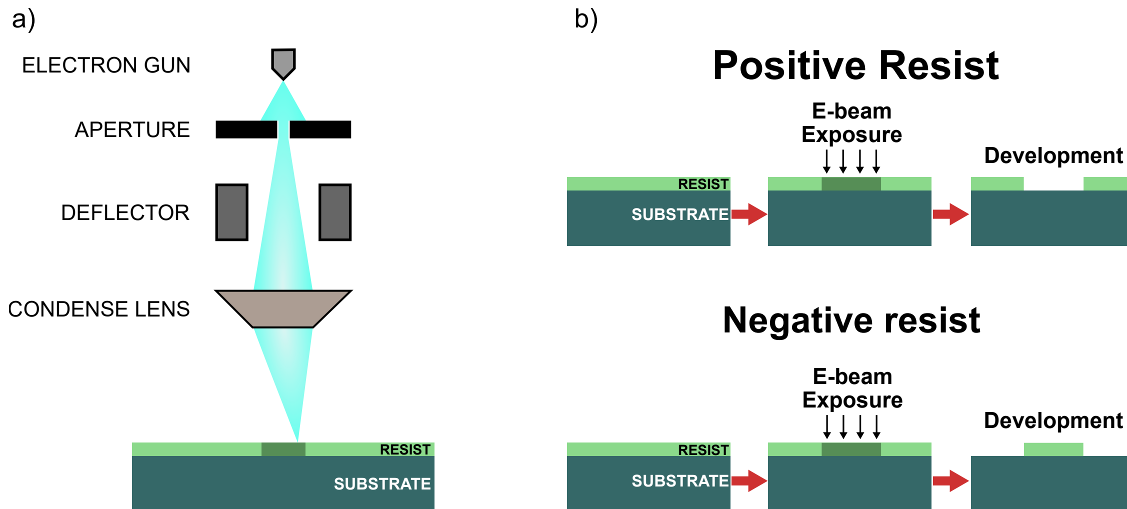

Figure 3.3: Principles of electron-beam lithography. a. Working principle of an EBL-system. A beam of electrons is emitted, filtered through an aperture, and focused unto the sample. A 500 × 500 μm^2 writing field is defined at a fixed position, and beam deflectors are used to spatially trace out the desired pattern. **b.** For a positive resist, the exposed areas are removed after development, while a negative resist leaves only the exposed areas after development.

An electron emitter provides a beam of electrons that is constricted through an aperture. A magnetic condenser lens focuses the beam onto a writing spot on the surface of the sample. A set of electromagnetic deflectors are used to manipulate the spot laterally on the writing surface, thereby tracing out the pattern that is to be exposed. The *dose* or *exposure dose* is the current of electrons per unit area. It is normally measured in $\mu C/cm^2$, and can be controlled by varying the electron current and exposure time. The highest achievable resolution of EBL-systems is in the range of 0.06-0.15 nm [63]. In practice the resolution is limited to ∼10 nm. There are multiple reasons for this, but one major factor arises from the interactions of the beam electrons with the resist and substrate. The forward scattering and backscattering of electrons is collectively known as *proximity effects*.

Proximity effects lead to a broadening of the exposure area, causing unwanted exposure or over-exposures. Forward scattering is due to electron-electron interactions deflecting the beam electrons by a small angle in the resist. The effect of forward scattering is influenced by the acceleration voltage of the EBL-system. In this work, an Elionix ELS-F125 with an acceleration voltage of 125 KeV is used. The high acceleration voltage ensures that most electrons pass through the resist with minimal interactions, reducing the effect of forward scattering. After passing

through the resist, some electrons may scatter off heavier atoms in the substrate, leading to a wide-angle scattering of electrons, again causing unwanted exposure. This backscattering of electrons can be corrected for using specialized software such as Beamfox Proximity, which fractures the desired patterns into smaller polygons and corrects the doses to reduce proximity effects.

The choice of resist and resist developing conditions is also important. In this work, the positive resist *ZEP520* by Zeon Chemicals L.P. was used due to its high sensitivity and resolution, and *CSAR* by Allresist GmbH was used as an alternative. To ensure a flat and even layer of resist with the optimal thickness, the resist is spin-coated onto the sample. The thickness of the resist can be gauged by expert eyes (in the case of ZEP520, a green color with a pinkish hue roughly corresponds to a thickness of 550 nm), or measured precisely using a Filmetrics Thin Film Thickness Measuring system. Both ZEP520 and CSAR can subsequently be developed in n-amyl acetate at room temperature (RT), or at -5 °C when higher resolution and edge smoothness is required [64].

3.3 Fabrication procedure

3.3.1 Metal deposition and lift-off

In this work, small metal electrodes are used to implement the electrostatic actuation that pulls the central waveguides apart. Well-defined electrodes are key to ensure good device performance, as damaged electrodes may have detrimental impacts on the tuning of the DC. These electrodes, as well as the large metal bonding pads, are deposited through a metalization/lift-off process. First, the sample is spin-coated with ZEP520 and the patterns are exposed using EBL as described in section 3.2. After development, the sample is cleaned by plasma descum. This ensures that any residual resist in the exposed regions of the sample is removed, thereby ensuring good contact between the surface of the sample and the metal. The sample is then loaded upside-down into a physical vapor deposition (PVD) system. The evaporation process begins by pumping down the chamber to a vacuum of $\sim 10^{-7}$ mbar. A beam of electrons is deflected by magnets onto a crucible containing the desired metal, causing energy to be transferred from the impinging electrons to the metal, ultimately leading to evaporation of the metal. Metal atoms then travel out of the crucible and coat the sample in a thin and even layer, with a rate of less than 1 nm/s. The thickness of the film is determined by the changing of the oscillation frequency of a quartz crystal. The deposition rate can then via a feedback loop be controlled by altering the current of the electron beam.

In previous works, the small electrodes and large bonding pads were fabricated separately. In this work however, a newer PVD system allows for fabricating both the small electrodes and large bonding pads simultaneously. Both are made from a 170-nm layer of Au, with a 10-nm layer of Cr deposited prior to increase adhesion between the sample surface and the metal. This is a considerable improvement over previous works, where Ni and Ti were used as adhesion layers for the small electrodes and bonding pads, respectively. Using Cr throughout simplifies the entire metalization process substantially, and Cr is found to stick better than Ni. After

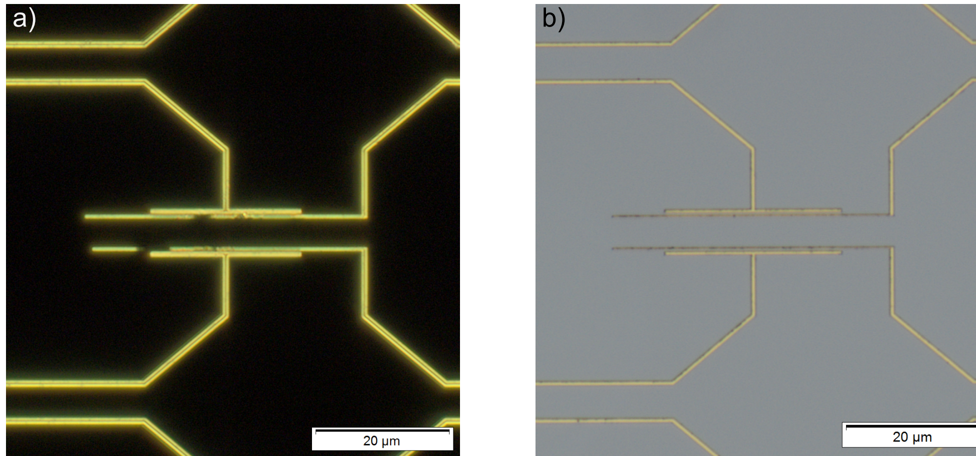

Figure 3.4: Optical images of the metal electrodes. a. Partially stripped metal electrodes. The electrodes are defined by EBL and the deposition of a 170-nm layer Au. Lift-off of the metals in unwanted parts is a crucial step, and is here overdone, causing detrimental electrode damage. **b.** Same as **a.**, but with an improved lift-off process. Improving the lift-off process results in a higher yield rate. Some residues remain on the electrodes.

metal evaporation, the lift-off process removes the resist in non-patterned areas (and evaporated metal on top of it), leaving metal only in the patterned areas. Previously, this has been done by submersing the sample in hot (80 °C) N-Methyl-2-pyrrolidone (NMP), blowing most of the unwanted metal off with a pipette, and leaving the sample overnight in RT NMP. This method was however found to produce inconsistent results, as it often lead to leftover metal not being stripped in non-patterned areas, effectively ruining the sample. A different lift-off technique is therefore used, where the sample is first submersed in hot NMP, and subsequently sonicated at low power and frequency to aid in the removal of the resist. As shown in fig. 3.4.a, this process should be done with caution, as overdoing the sonication easily leads to stripping of the small electrodes, detrimental to device performance. The optimized fabrication recipe in appendix B is found to produce the most consistent results, leaving clearly defined electrodes such as those pictured in fig. 3.4.b.

3.3.2 Etching of shallow-etched gratings

Efficiently coupling light into on-chip photonic structures is critical for the device performance. In this work, chip-to-fiber coupling is achieved with *shallow-etched gratings* (SEGs), which offer high coupling efficiencies (> 60%) and low back reflections (< 1%). These couplers have previously been studied and optimised for the desired central wavelength of 930 nm [65]. The working principle of SEGs is illustrated in fig. 3.5.a. The thickness of the AlGaAs sacrificial layer is important for SEGs, as the coupling efficiency is affected by the depth of the undercut. The optimal thickness has previously been found through simulations to be 1150 nm. Wafers with this sacrificial layer thickness are therefore preferred. The back-reflection can be minimised by ensuring that the SEG is completely undercut by the deep etching process described in section 3.3.3.

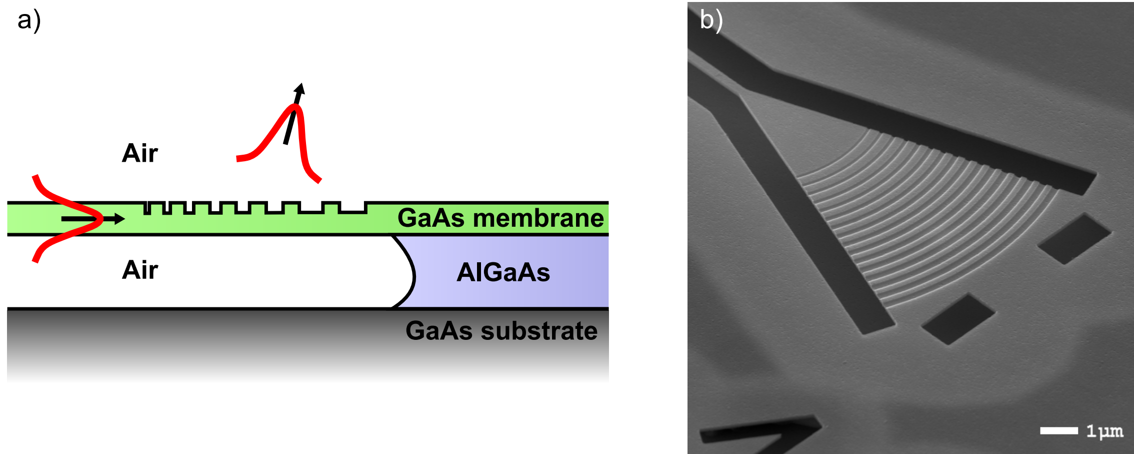

Figure 3.5: Working principle of shallow-etched gratings. a. Schematic cross-section of a SEG. The grooves of the SEG form a crystalline structure that diffract a propagating mode upwards at an angle. **b.** SEM of a fabricated SEG. The SEG is fully undercut, ensuring that reflections are minimized.

The patterns of the SEG are defined by EBL on a CSAR9% resist, which after development is dry etched to create the grooves of the grating. Dry etching is a method to remove material from a sample using a highly energetic plasma, and is in this work done by reactive ion etching (RIE) for the SEGs. Controlling the etch depth is of great importance, as this influences the central transmission wavelength and reflectivity of the gratings. RIE has a relatively slow etching rate, thereby providing greater control of the etching depth.

In RIE, a specific combination of gasses are introduced into a vacuum chamber containing the sample. The sample itself is placed on one of two parallel plates, where one of them is grounded. Applying a strong radio-frequency (RF) electromagnetic field to the sample plate ionizes the gas molecules, creating a plasma. Positive ions are accelerated towards the sample, ultimately colliding with it. Material on the sample is subsequently removed by a combination of a chemical reaction between the ions and the sample, and the ions physically knocking off material (sputtering). Due to the verticality of the ion collision with the sample, an anisotropic etching profile is achieved. Conversely, the etching due to chemical reactions is isotropic, which is not favorable. Optimal control of the chemical processes is therefore critical to provide an anisotropic profile, while increasing the selectivity of the material etched and minimizing surface damage [66]. The etching depth can be monitored by interferometry with a laser on a 200×200 µm^2 reference square. In this work, a mixture of BCl_3 and Ar gasses are chosen, with controlled flows of 5 and 10 sccm, respectively. The pressure is maintained at 20 mTorr, and the supplied RF field power is 43 W. The introduction of Ar gas is mainly to induce sidewall passivation, to prevent etching of the sidewalls and increase the anisotropic profile. A fully undercut SEG with anisotropically etched groves, fabricated in this work, is pictured in fig. 3.5.b.

3.3.3 Etching and undercut of photonic structures

RIE is well suited for cases where feature sizes are relatively large and the etch depth relatively small. However, for cases where resolution and deep etching depths are required, RIE falls short. This is due to an effect called *RIE lag*, causing smaller openings to etch slower than large ones, and have more isotropic profiles [67]. To reduce this effect, the plasma pressure can be lowered and ion energy increased. This is however not possible with RIE, as there is only one power supply that controls both plasma density and ion acceleration. To overcome this, an additional inductive coil is introduced providing a strong magnetic field specifically used to control the dissociation rate of the gasses, and thereby the plasma density, as pictured in fig. 3.6. Coupling this with the RF bias on the sample to independently control the ion energy, highly anisotropic profiles and high etching rates can be achieved [68]. This is the principle behind inductively coupled plasma (ICP) etching, a process that is critical for defining photonic structures with nanoscale feature sizes, such as the narrow central waveguides adopted in this work. The process of defining these photonic structures starts similarly as previous steps - with EBL. For the first produced sample, ZEP520 was used, while for the second sample, the recipe was adapted to use CSAR resist instead. This might have an affect on device performance, as different resists react slightly differently to EBL and ICP processes.

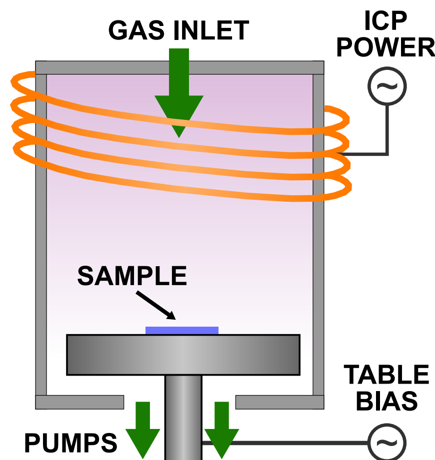

Figure 3.6: Reactive ion etching/inductively coupled plasma etcher. An RF electromagnetic field creates a plasma, and positive ions are accelerated towards the sample by a voltage bias. Material is removed from the sample chemically and physically by the impinging ions. In ICP etchers an additional power coil is introduced to achieve higher etch rates and more anisotropic profiles.

The ICP recipe used in this work follows the one developed in [69], which has been optimised to yield high anisotropicity, smooth sidewalls and high material selectivity. The sample is first glued to a Si wafer using a thermally conductive and removable adhesive, and the electrode upon which it is placed is lowered to 0 °C, in order to avoid excessive heating and resist re-flow. A combination of BCl_3, Cl_2 and Ar gasses with respective flow rates of 3/4/25 sccm is used, and the chamber pressure is 4.7 mTorr. Here, the chlorine acts as the main etching agent, while boron trichloride is used for sidewall passivation, and argon is introduced for dilution as well as

increasing the physical etching rate. The ICP coil power is set to 300 W and the electrode RF power is 47 W. The etch depth is here measured on the resist layer using laser interferometry, and the process is automatically ended when roughly 260 nm of resist remains, as resist layer thicknesses smaller than 200 nm tends to enlarge the etched features and erode the sidewalls.

After ICP etching, the remaining resist is removed in hot (70 °C) NMP (or RT 1,3-dioxolane for CSAR resist). Selective removal of the sacrificial AlGaAs layer to suspend the photonic structures is subsequently carried out by wet etching with a hydrofluoric acid (HF) solution. This is a suitable choice as HF does not etch GaAs, but will etch $Al_xGa_{1-x}A$ (for both wafers used in this work, $x = 0.77$). The HF etch rate mainly depends on the HF solution concentration and the Al concentration of the sacrificial layer, and the size of the undercut (the length of membrane around the structures that is suspended) is controlled by the etching time. For example, on the sample used in this work, a 5 % HF solution with an etch time of 44 s was found to give an undercut of ~ 3 μm. The process is ended by submersing the sample in Milli-Q (MQ) water to dilute the HF. After this step, it is imperative to handle the sample with the utmost care to avoid the collapse of the structures on the sample - this includes ensuring that the sample is submerged in liquid during the entire cleaning process. If the sample at any point is allowed to dry out, the capillary forces between the liquid and sample cause a surface tension that can potentially collapse the structures [70]. To overcome this issue, the sample is placed in a "boat", remaining fully immersed as it is transported between the various liquids of the etching and subsequent cleaning processes.

3.3.4 Finishing cleaning and drying procedure

Wet etching with HF inevitably leads to the formation of unwanted residues. It is imperative to properly clean the sample after wet etching, as residues accumulated on the fabricated structures can lead to losses due to scattering in waveguides, and severely limit device performance. Aluminum triflouride (AlF_3) is one such residue, and can be found on the surface of the sample in a crystalline structure. AlF_3 is easily diluted in water, and can therefore be removed simply by immersing the sample in clean MQ water after wet etching. Residue in the form of carbon-rich films is also prevalent, and originates from resist damaged during the ICP etching process. These cannot be removed effectively with NMP, but can instead be converted into CO_2 and water by dipping the sample in hydrogen peroxide (H_2O_2). This, however, has the unwanted side-effect of oxidizing GaAs. The oxidized layer can be removed by phosphoric acid (H_3PO_4), which has the added benefit of dissolving other residues such as aluminum hydroxide ($Al(OH)_3$) found on the bottom of the etched areas. In the final step, the sample is transferred from water to isopropyl alcohol (IPA). Water and IPA are miscible, but due to slightly differing densities - 1 g/cm3 for water compared to 0.786 g/cm3 for IPA - turbulence between the two liquids occurs upon mixing. The transfer of the sample from MQ water to IPA must therefore be carried out slowly and with caution. In practice, this is carried out by placing the sample at the bottom of a beaker containing enough MQ water to cover the sample. IPA is then slowly poured in from the sidewalls of the beaker, while moving the sample slowly up, thereby gently introducing IPA into the boat containing the sample. The

sample can then be transferred to subsequent IPA beakers to ensure that no water remains. Drying the sample requires a process that eliminates surface tension. This is achieved by utilizing critical point drying (CPD). The sample is first loaded into the CPD holder, where it remains submersed in IPA, and the holder is then loaded into a Leica EM CPD300 automated critical point dryer. Here, the IPA is gradually exchanged with liquid CO_2. The chamber pressure is thereafter increased to 74 bar and the temperature to 31.1 °C - bringing the CO_2 to its critical point. At this point, phase boundaries between the liquid and gaseous state vanish, reducing surface tension to zero. The CO_2 thus effectively goes from liquid to gaseous state without crossing the liquid-gas boundary. The resulting gaseous CO_2 is removed from the system, leaving the finished sample dried out.

3.4 Fabrication results

The methods and techniques described in this chapter comprise some of the fundamental processes for fabricating a great variety of photonic structures, and can also be applied in other fields, such as microelectronics. The individual steps must however be modified to the requirements of the specific device. In this work, a total of 5 samples have been fabricated to completion following the recipe given in appendix B. However, only two samples were of high enough quality, and with high enough device yield rate, to warrant subsequent investigations. These will be referred to throughout the following chapters, and sample specific details are given below.

- **LoopSwitchB**: Fabricated on a new, undoped wafer with optimised sacrificial layer thickness. A more gentle lift-off approach was used for this sample, leaving it in NMP overnight and blowing on it with a pipette as a substitute for sonification. This left the electrodes in good condition, but somewhat dirty, as shown in fig. 3.4.b. The SEGs on this sample are not completely suspended, resulting in less transmission and higher reflectance of the SEGs.

- **NEMSV3**: Fabricated on an relatively old undoped wafer with a non-optimal sacrificial layer thickness of 1370 nm, likely reducing the transmission efficiency. Excess sonication lead to electrode damage on some devices, as pictured in fig. 3.4.a. CSAR resist was used as a replacement for ZEP520, which might affect device performance. ALL SEGs were either completely or almost fully suspended. It is apparent from SEM images that some residues remain on the sample.

CHAPTER 4

Experimental setup

Experiments with QD single-photon sources are often conducted at cryogenic temperatures in order to limit the interactions of the QD and the surrounding environment, and preserve the coherence of the emitted photons [71]. For low temperatures (< 60 K), acoustic phonons (vibrations in the crystal lattice) shake the QD emitter, causing its discrete energy levels to blur, at a dephasing rate that depends linearly on the temperature. For this reason, it is imperative that the devices introduced in this work are compatible with cryogenic temperatures. The samples are therefore placed in cryostats, and all characterization measurements are either conducted at < 10 K, or both in RT and < 10 K. Characterizing the devices also requires the operation of several types of lasers and a versatile setup that allows for good optical control of the laser input. In this chapter, the optical setups, lasers, and cryostats used in this work will be described. The optical setups are pictured in fig. 4.1, which also include the laser input and collection paths.

Mounting the sample

Measurements to characterize the fabricated devices are performed in two different setups: measurements on the LoopSwitchB sample are conducted in the *flow* setup, while measurements on the NEMSV3 sample are conducted with the *ARS* setup. These setups share several similarities, but differ in fundamental ways, and will thus be described individually. In both cases the sample is first glued unto a sample holder using silver glue with high thermal conductivity. The sample is placed on a copper pad on the sample holder to ensure good thermal contact with the cryostat. The large metal bonding pads on the sample are then wire-bonded to metal pads on the sample holder, enabling a current to flow from a DC source (Keithley 2450 Sourcemeter), through custom coaxial feedthroughs in the cryostats, to the sample, once it is mounted. The sample holder is then mounted in the transfer chamber of a cryostat, which is subsequently pumped down to a high vacuum ($\sim 10^{-7}$ mbar) and cooled down to <10 K.

Laser sources

The different characterization measurements require utilizing different lasers. For broadband transmission measurements of the NOEM mirror, a super-continuum white light laser (SuperK by NKT Photonics) is utilized. The wavelengths of interest are filtered by a low pass filter (LP) and dichroic mirror (DM). Narrowband transmission measurements of the NOEM mirror are conducted using a continuously tunable laser (CTL with DLC Pro driver by Toptica Photonics) offering high resolution (linewidth of < 10 kHz) and small step size (0.3 pm). For QD photoluminescence measurements of the NOEM phase shifter, the QDs are excited by the above-band excitation scheme described in section 2.1.2. This is implemented using a pulsed diode laser (PDL800-B driver with LDH-P-C-780 diode head by PicoQuant) with a central emission wavelength of 780 nm and variable repetition rate of 2.5-40 MHz. The output power of all three lasers can be controlled and stabilized using a homemade proportional-integral-derivative (PID) setup. The lasers are coupled to fibers and sent to the free-space parts of either of the two setups.

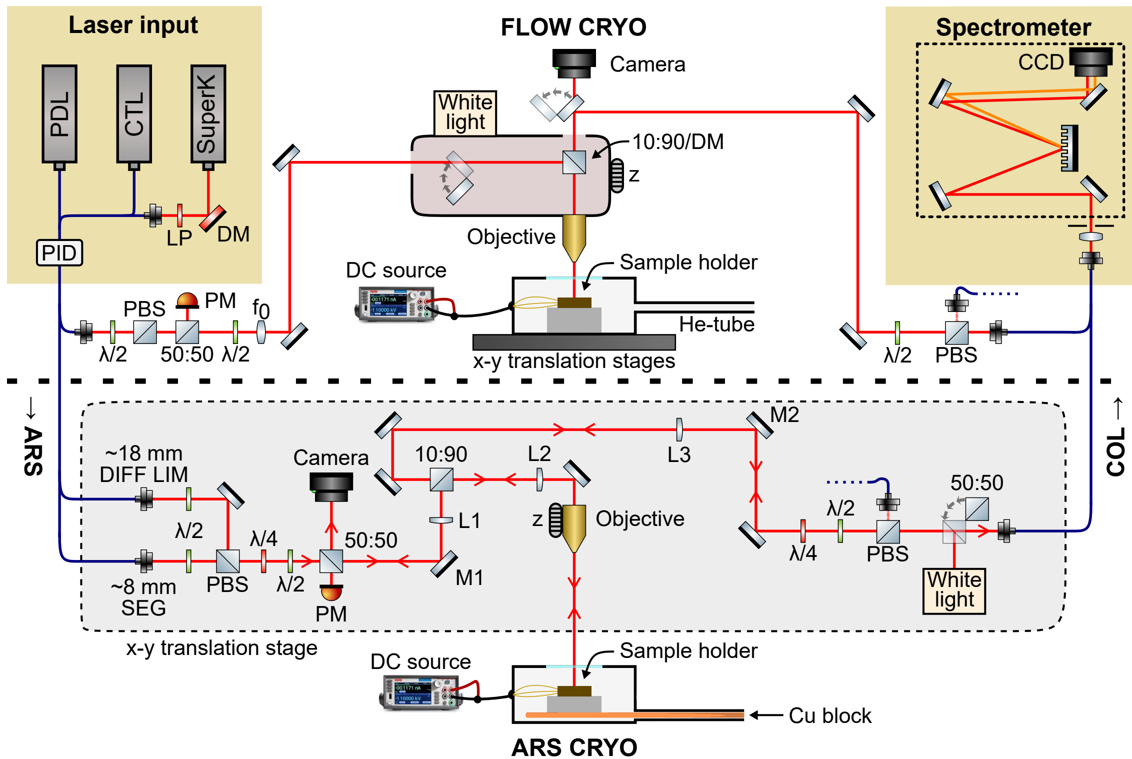

Figure 4.1: Schematic of the experimental setups. Three lasers are available depending on the type of measurement to be conducted. Two optical setups and cryostats are used in this work: the top half depicts the FLOW setup, while the ARS setup is shown in the bottom half. Light from either setup is sent to the collection path, where a spectrometer measures the captured intensities at different wavelengths. See the main text for more details.

Flow setup

The flow cryo setup is depicted in the top half of fig. 4.1. The sample is here cooled in a Microstat HiRes II continuous-flow cryostat from Oxford Instruments. The cryostat is cooled by a continuous flow of liquid helium to a heat exchanging chamber, which is in thermal contact to the copper pad of the sample holder. The temperature is controlled by a PID temperature controller via a heater attached to the heat exchanger, or by manually adjusting the rate of liquid helium, and is monitored by a thermal sensor. The transfer chamber itself is mounted on an x-y translational stages, providing large travel lengths on the sample and positioning of the cryostat with a precision of 0.1 µm.

Laser light enters the free-space part of the flow setup by a fiber coupler, where it first hits a half-wave plate ($\lambda/2$) and a polarizing beamsplitter (PBS). This allows for additional fine-tuning of the optical power to the sample. The input power to the sample can be monitored by splitting the path with a 50:50 beamsplitter and measuring the reflection port with a powermeter (PM). The polarization of the input laser can be controlled by a second half-wave plate. Light is then coupled to a focusing system (Olympus BXFM) above the sample. A handle on the mount introduces/removes a mirror to switch between an integrated white light source for illuminating the sample and laser excitation. Light is reflected towards the sample by either a 10:90 beamsplitter or dichroic mirror (for QD photoluminescence measurements, cutoff at 870 nm). Light is focused unto the sample with a 40X objective with a numerical aperture of 0.6. Light collected from the sample can be sent to either a charged-coupled device (CCD) camera for imaging or to the collection path, by removing/introducing a second mirror. The latter contains a half-wave plate and a PBS, whose outputs are coupled to fibers, potentially allowing for collection from two spatial regions on the sample. In this work however, only a single output port is used, which is sent to the collection path via fibers.

ARS setup

The ARS cryo setup is depicted in the bottom half of fig. 4.1. The cryostat used in this setup is a CS210F-GMX-20-OM closed-cycle cryostat from Advanced Research Systems (hence the name ARS). Here, the sample holder is in thermal contact with a copper block, which is cooled by the cold tip of the cryocooler in a space separated from the sample. The cold tip and copper block are however not in direct contact, and the thermal exchange is instead mediated by a helium exchange gas. This method of cooling has the benefit of minimizing vibrations, and doesn't require a continuous flow of cryogen. As opposed to the flow setup, the sample is here fixed to the table, and the entire optical setup is instead placed on x-y translation stages (greyed-out striped box in fig. 4.1) to administer travel along the sample. Light from the laser can be introduced to the optical path from two couplers: one that is optimized for SEGs, and another offering a diffraction limited spot-size (DIFF LIM). The power from these paths can be controlled by half-wave plates and a PBS. Full control of the input polarization is achieved with a subsequent quarter-wave plate ($\lambda/4$) and half-wave plate. A powermeter aligned with the reflection port of a 50:50 beamsplitter allows for monitoring the input power. Light is then directed into a vertical path above the sample, and is focused onto the sample with a 40X objective with a numerical aperture of 0.6. Light collected from the sample is then

partially reflected or transmitted by a 10:90 beamsplitter. The former is sent back through the setup onto a CCD camera for imaging, and the latter is sent to the collection path. In the collection path light can be coupled to two different output ports via a quarter-wave plate, half-wave plate and PBS, but in this work only a single output port was used, where light is sent to the collection path by fibers. A 50:50 beamsplitter can be introduced close to the out-coupler to allow a white-light source to illuminate the sample for imaging. By introducing a long-pass filter (cutoff 900 nm) in front of the camera, only the QD emission from the sample will be imaged, making it easier to focus to the sample at the correct wavelength.

Collection

Light collected from either setup is sent via fibers to a Princeton Instruments SP2500i spectrometer, where it is dispersed and the intensity at different wavelengths is measured at a CCD. Two dispersion gratings offering different wavelength ranges and resolutions are available. For the broadband transmission measurements, a coarse grating (150 g/mm) is used, with a resolution of 0.5 nm and range of 350 nm. For narrowband transmission and QD photoluminescence measurements, a fine grating (1200 g/mm) is instead employed, which has a much higher resolution of 0.05 nm, but also a narrower bandwidth of only 32 nm.

CHAPTER 5

Characterization of the tunable NOEM mirror

As presented in section 2.2.3, the switching effect produced by the central DC of the tunable NOEM mirror operates by the interference of propagating normal modes. It is therefore expected that the NOEM mirror displays a strongly dispersive behaviour. The interference of the normal modes can be altered via the electro-mechanical coupling in the device by imposing a voltage bias. In this section, the optical properties of the tunable NOEM mirror as a function of wavelength is investigated for different applied voltage biases.

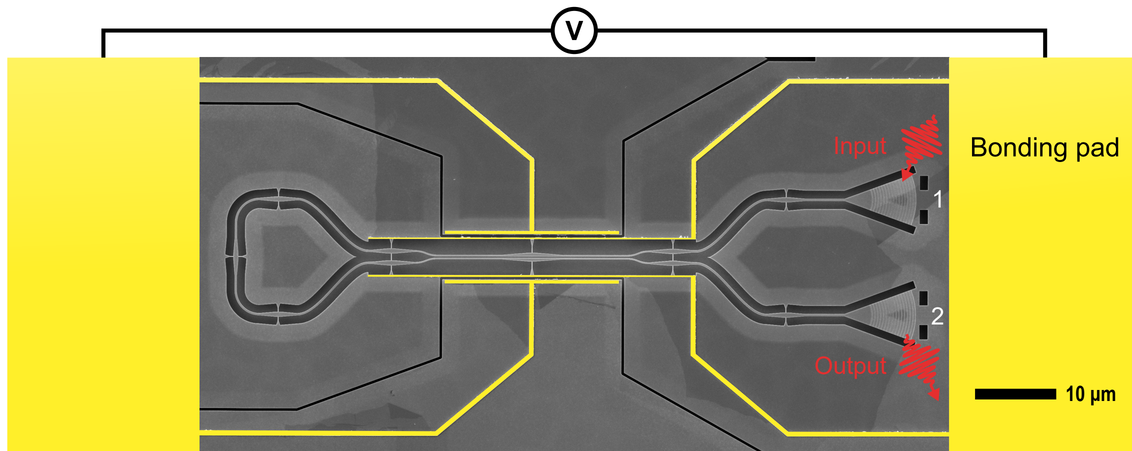

Figure 5.1: False-colored SEM of the NOEM mirror. The excitation laser is sent into port 1, and the transmitted light is collected at port 2 and measured with the spectrometer. Spectra are captured for different voltages applied to the electrodes (highlighted in yellow). The bonding pads are shown closer to the device than de facto for illustrative purposes.

5.1 Broadband optical characterization

The optical properties of a fabricated NOEM mirror device, pictured in fig. 5.1, is first investigated with the SuperK white-light source as the input laser. The measured device is from the LoopSwitchB sample, on which a total of forty-eight devices are fabricated and connected in parallel, each with different structural parameters. Of the parameters that are varied between devices, this specific device has a coupling length over which the normal modes interfere of L_c = 24 µm, starting waveguide gap distance y_0 = 100 nm, shuttle electrode length L_s = 22 µm and shuttle width w_s = 260 nm. The input laser is focused onto port 1, and the transmitted light spectrum is collected at port 2, which is recorded with the spectrometer equipped with the coarse grating. Optimally it would be favorable to also collect the reflected light of port 1, but exciting and collecting in the same port leads to a great amount of scattered light being collected, resulting in a noisy spectrum. The induced voltage bias is swept from 0 V to 8 V with steps of 0.1 V, and a transmission spectrum is recorded at each step. The maximum voltage is safely below the estimated pull-in voltage given by eq. 2.17 for this device of V_{PI} = 13.65 V. After the ramp up in voltage, the device is brought back to resting position by a opposite ramping down. The measurements presented here are conducted at RT.

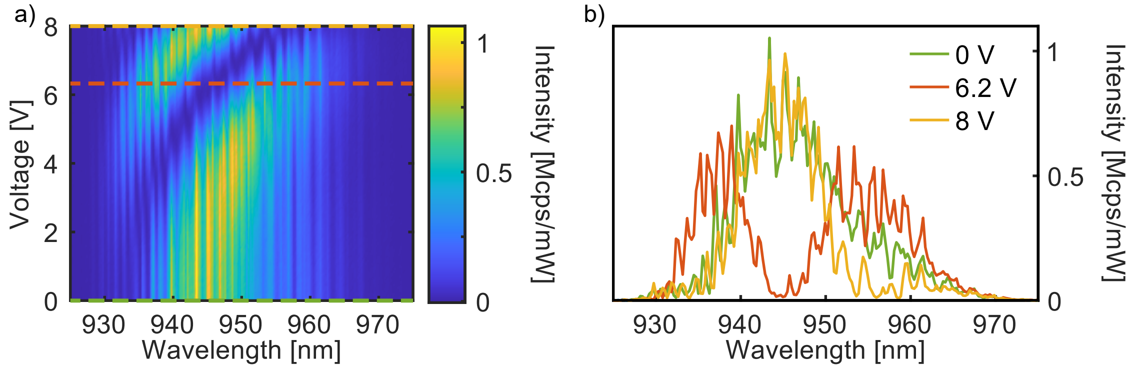

Figure 5.2: Broadband tuning of the transmitted intensities. a. Measured intensities at port 2, as a function of wavelength, for different voltages. A clear tuning of the transmission spectrum is observed. **b.** Cross-sections along the wavelength for select voltages. The cross-sections highlight the device's ability to fully extinguish (6.2 V, red curve) and regain (8 V, yellow curve) the transmission signal compared to starting point (0V, green curve).

The results of the voltage sweep as a function of wavelength and voltage are plotted in fig. 5.2.a. The power of the input laser is measured at each voltage step, and the data have correspondingly been normalized to a selected (arbitrary) excitation laser power and exposure time. From the data it is evident that the device is capable of extinguishing and regaining the signal to the transmitted port as the voltage across the electrodes is varied. To further illustrate this, three cross-sections at voltages of interest are plotted in fig. 5.2.b. The peak of the signal at 0 V is suppressed at 6.2 V and completely restored at 8 V.

5.1.1 Fringes analysis

Fringes in the spectra following the wavelength can be seen, which seemingly shift when the transmission reaches a minimum. The shift of the fringes is predicted by the S-matrix model of the mirror introduced in section 2.3.2, suggesting that these fringes stem from the device. This is shown in fig. 5.3.a, where the transmission intensity ratio is plotted along with the change in phase as a function of the waveguide displacement. As the transmission reaches a minimum, the mirror introduces a π phase shift to the light at the output port.

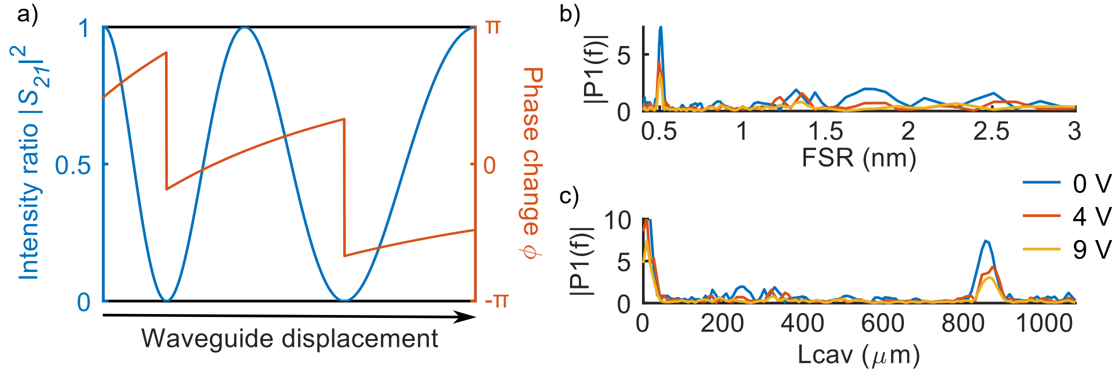

Figure 5.3: Analysis of the fringes in the measured spectra. a. Including information of the phase in the S-matrix model reveals that the device induces a π-phase shift at a transmission minimum, explaining the shift in the fringes observed in the data. **b.** Fast Fourier transform of the spectra at different voltages show a clear peak at FSR = 0.5 nm in the measured data. **c.** Corresponding optical cavity length (in air). The peak found at 853 µm corresponds to an optical cavity length of 159 µm when divided by the estimated group index of the device, which matches the approximate optical travel distance in the device.

In the NOEM mirror, SEG out-couplers that are not fully undercut impose a finite reflection coefficient, effectively forming a Fabry-Pérot cavity. In a Fabry-Pérot cavity, the transmission is given by [72]:

$$T = \frac{(1-R)^2}{1-2R\cos(\delta)+R^2}, \tag{5.1}$$

where R is the reflectance of the mirrors forming the cavity, and δ is the phase difference between successive transmission pairs:

$$\delta = \left(\frac{2\pi}{\lambda}\right) 2nl, \tag{5.2}$$

where n is the refractive index and l the optical cavity length. For $\delta = m \cdot 2\pi$ where m is in integer, the transmission reaches a peak, at corresponding wavelengths:

$$m \cdot 2\pi = \left(\frac{2\pi}{\lambda_{max}}\right) 2nl \Rightarrow m \cdot \lambda_{max} = 2nl, \tag{5.3}$$

with λ_{max} defined as the wavelength of a transmission peak. A sudden π phase shift induced by the DC would therefore cause all λ_{max} to shift by half the distance

between successive peaks, i.e. half a *free spectral range* (FSR), matching what is observed in the measured data. The FSR also provides information on the origin of the observed fringes, as it is related to the optical cavity length by:

$$FSR = \frac{\lambda_0^2}{2n_g l}, \tag{5.4}$$

where λ_0 is the central wavelength and n_g is the group index. For this NOEM mirror the corresponding l between the gratings is ~ 174 nm. For an estimated group index of $n_g = 5.36$ and central wavelength at $\lambda_0 = 930$ nm, the expected FSR becomes 0.46 nm. Resolving the FSR therefore requires a higher resolution than what is available with the coarse spectrometer grating (resolution of 0.5 nm).

To investigate the fringes in more detail, a similar measurement scheme as introduced in the previous section is implemented, but instead sweeping a broad wavelength region with the CTL and resolving with the fine spectrometer grating. A fast Fourier transform of the captured spectra resolves the FSR of the fringes, which is plotted for different voltages in fig. 5.3.b. The dominant FSR is found to be at 0.5 nm. Figure 5.3.c plots the corresponding cavity lengths (for air) given by eq. 5.4, and the main peak is found to be at 853 µm, which divided by the estimated group index gives $l = 853$ µm$/5.36 = 159$ µm, roughly matching the length between the two SEGs of the device. The discrepancy between the measured and expected cavity lengths is most likely due to the estimated n_g or evaluated central wavelength λ_0 not being exactly accurate. For the SuperK measurements, the observed fringes are most likely a mix of several fringes, most of which come from the setup.

5.1.2 Transmission bandwidth

The change in signal as a function of voltage is found to be strongly dispersive - it is however important to note that tuning of the transmission spectrum is achieved over the entire transmission bandwidth. The bandwidth of the device is roughly 35 nm, which is limited by the transmission profile of the SEGs that are used to couple light in and out of the device. The transmission profile of the SEGs can be captured by measuring the transmission through a nano-beam waveguide, a passive structure consisting of two SEGs distanced similarly as in the NOEM mirror, but with only a short waveguide connecting them. This structure is depicted in fig. 5.4.a and the averaged spectrum of three similar nano-beam waveguides is shown as the blue curve in fig. 5.4.b.

5.2 Comparison to S-matrix model

Comparing the obtained results to the S-matrix model of the mirror presented in section 2.3.2 requires first normalizing the data and extracting the waveguide displacement (gap distance) as a function of the applied voltage. To remove the profile of the dispersive SEG coupling efficiency from the spectra, the recorded data is normalized to the nano-beam waveguide transmission. Both the mirror and nano-beam waveguide transmission spectra have been smoothed to give a cleaner spectrum without fringes, as indicated in fig. 5.4.b. The applied voltages are subsequently

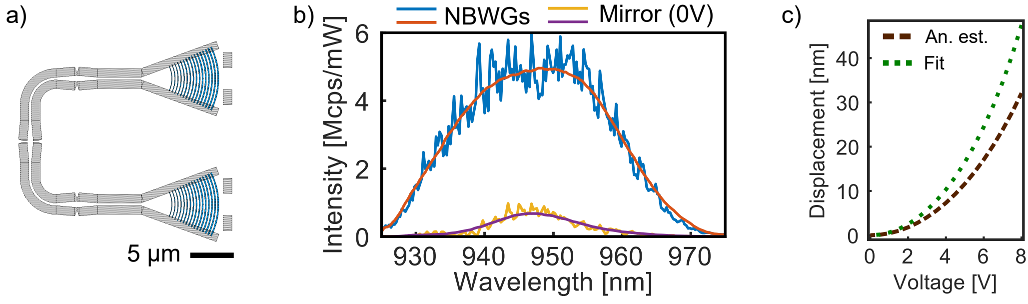

Figure 5.4: Normalization to a nano-beam waveguide. a. Nano-beam waveguide structure. **b.** Transmission spectra of the nano-beam waveguide structure (blue curve) and mirror at 0 V (yellow curve). To flatten out fluctuations, spectra from both devices are smoothed. Spectra of the mirror for all voltages are then normalized to the nano-beam waveguide structure. **c.** The waveguide displacement as a function of voltage given by eq. 2.16 for nominal device values (brown dashed line) and for fitted values (green dotted line). The deviation between the two indicate that the device stiffness has been underestimated.

transformed into actual displacements of the directional coupler waveguides by utilizing the electrostatic actuation model given by eq. 2.16, and the nominal device parameters. The waveguide displacement as a function of voltage given by this model is plotted in fig. 5.4.c (brown dashed line). While this relation is sufficient for an initial comparison between the S-matrix model and the measurements, eq. 2.16 depends solely on geometrical properties of the device, which are highly influenced by fabrication results. The expected maximal displacement at 8 V is found to be 32.1 nm. The normalized data as a function of waveguide displacement is plotted in fig. 5.5.a.

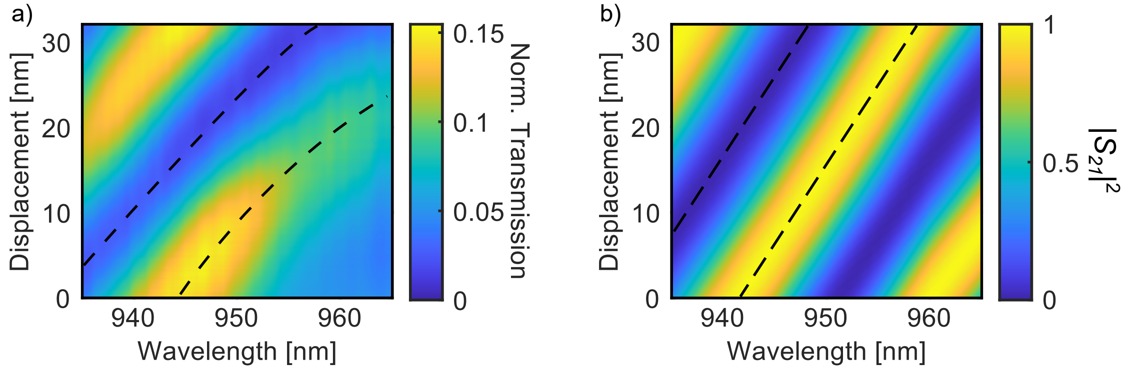

Figure 5.5: Comparison of the normalized data to the S-matrix model. a. Normalized spectra as a function of waveguide displacement. The displacement is calculated from eq. 2.16 and nominal device values. **b.** S-matrix simulation of the mirror, as a function of waveguide displacement. The predicted overall tuning behaviour is in good agreement with the measured data. In both figures, the black dashed lines highlight minima and maxima of the transmission spectra, showing a dispersion curve in the measured data not captured by the S-matrix model.

5.2.1 Device losses

Compared to the nano-beam waveguide, the transmission through the NOEM mirror is around 15 %, corresponding to a loss of ~ 8 dB. In ref [38], it is estimated that the losses from the DC are similar to that of a waveguide of the same length. There the waveguide losses are estimated to be $-(7.5 \pm 1.0)$ dB/mm. The waveguides used in this work are similar, and should therefore exhibit comparable losses. The estimated optical length from input to output of the NOEM mirror is about 195 µm, and the device insertion loss is therefore estimated to be (1.46 ± 0.2) dB. Propagation losses may vary from sample to sample due to differences in fabrication, but it is clear that propagation losses can not account for all the measured losses of the device. The insertion loss is an important figure-of-merit for any photonic device, and further work is needed to here determine its source, and improve the fabrication steps to reduce it. Losses in the device will also directly affect the tuning performance of the NOEM phase shifter, as was shown in section 2.3.3. Measurements to further characterize the loss in the devices were therefore attempted on passive, uncoupled versions of the NOEM mirror on the NEMSV3 sample in the ARS setup. The results of these measurements were however inconclusive, due to fabrication errors resulting in deformed SEG profiles that varied from device to device.

5.2.2 Improving the S-matrix model

The S-matrix model of the NOEM mirror can include a wavelength dependency, by using the numerical simulations of the DC (courtesy of Camille Papon), where the exact DC geometry was constructed in COMSOL Multiphysics together with a deformation profile that describes the change in waveguide geometry by the actuation from the electrodes. The results of the S-matrix model is plotted in fig. 5.5.b. This initial comparison shows that the modelled map roughly reflects the measured data. There are slight differences in the tuning and transmission, which are most likely due to small deviations in the geometrical parameters of the fabricated device compared to the intended parameters, and errors originating from the normalization. To show that the model can better replicate the measured data of the actual fabricated device, it can be optimized by varying the following parameters: the starting gap distance d_0 and coupling length L_c of the model, and the device stiffness k_T of the voltage-displacement relation (eq. 2.16).

In the following, an attempt to adjust the parameters of the S-matrix model to best emulate the observed transmission response is given. This "fitting" process is made further complicated by factors that the model does not address. Firstly, as can be seen in 5.5.a, at wavelengths longer than ~ 952 nm, the signal is strongly suppressed, caused by the SEGs of the device not transmitting well at these wavelengths. Secondly, the measured data shows a dispersive curvature that is not captured by the model. This is illustrated with the dashed black lines in fig. 5.5.a and 5.5.b, that track a maximum and minimum contour of the transmission along displacement and wavelength. In the modelled data, these contours follow a linear relation between increasing displacement and wavelength. For the measured data, this relation has a slight curvature. This means that when looking at cross-sections of the data along

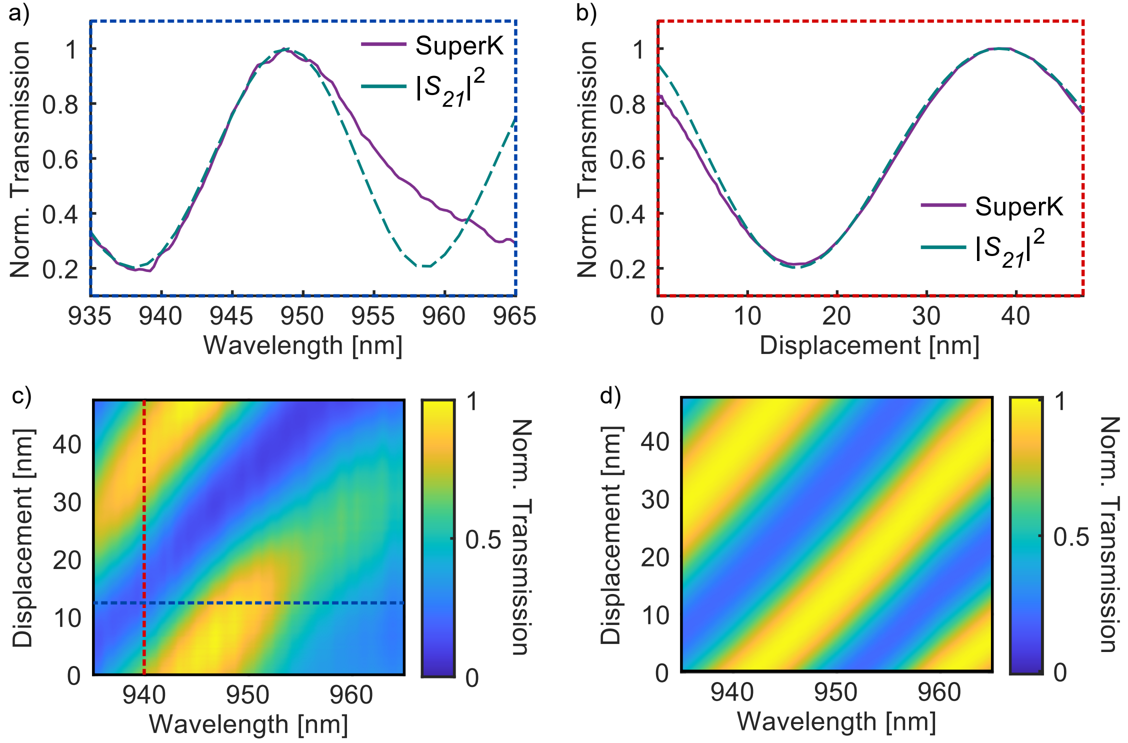

Figure 5.6: Improving the S-matrix model a. Transmission as a function of wavelength at a fixed waveguide displacement of 12 nm. Dashed line shows the numerical model, and solid line is the measured data. **b.** Same as **a.**, but as a function of displacement at a fixed wavelength of 940 nm. For both figures, the parameters d_0, k_T and L_c are adjusted until a good match is found. **c.** Normalized transmission spectra as a function of displacement, with the displacement given by the adjusted device stiffness. Blue and red dashed lines indicate the cross-sections shown in **a.** and **b.**, respectively. **d.** S-matrix simulation of the mirror, with improved parameters. Comparing this improved S-matrix model to the normalized data in **c.** shows a clear improvement over the previous comparison. The measured data in **a.**, **b.** and **c.** have been normalized to unity.

the wavelength, the width of the transmission curves will effectively change with the displacement. For cross-sections along the displacement axis, this results in a change of the tuning range with wavelength. For this reason, the model parameters are here adjusted to give the best match at the wavelengths around 938-945 nm, where the tuning is most clear.

The model is first adjusted by taking a cross-section of the data and model along the wavelength, and varying the initial gap distance d_0 until the curves are well-aligned. The coupling length L_c in the model can be varied to change the width of the transmission curves. This is illustrated in fig. 5.6.a for a cross-section at 12 nm waveguide displacement. It is easiest to fit at this gap distance, as there is a clear dip and peak in the transmission. The SuperK data has been normalized to unity for easier comparison. An adequate fit is found for a starting gap distance of $d_0 = 96$ nm and coupling length $L_c = 22.2$ µm (note that the total length of the waveguides includes a taper region of 7.8 nm in length, and the total length is therefore 30 nm). For comparison, the expected values were $d_0 = 100$ nm and

$L_c = 24$ µm. The differences between the adjusted and nominal parameters lie well within what can be justified as fabrication variations. Next, the tuning range is fitted by taking cross-sections of the measured data and model along the displacement, and varying the system stiffness k_T. This is illustrated in fig. 5.6.b for a wavelength of 940 nm. An adequate fit is found for $k_T = 0.64$ Nm^{-1}. The model deviates slightly from the measured data at smaller displacements, which is most likely due to the dispersion in the measured data explained previously. Compared to the analytical value of $k_T = 0.89$ Nm^{-1}, this suggests that the fabricated device is significantly more flexible, and that the maximal achievable displacement has been underestimated. For $k_T = 0.64$ Nm^{-1}, the maximal induced displacement is found to be 47.5 nm. The voltage-displacement curve using the adjusted value is plotted as the green dotted line in fig. 5.4.c.

The measured data normalized to unity with the adjusted k_T is plotted in fig. 5.6.c, and the adjusted model is plotted in fig. 5.6.d. The improved model shows good agreement to the data, and accurately predicts the tuning behaviour of the device. The model also describes the dispersive nature of the NOEM mirror to some extent, but fails to completely capture the dispersive curvature encountered in the measured data. For the device presented here the effect is minimal, but measurement on devices with other parameters in some cases show more extreme curvatures. During the fitting process it was noted that introducing minor corrections in the propagation constants β_S and β_{AS} could change the shape and contour curvature of the model, but no combination was found to successfully produce a good match to the data.

5.3 Transmission fine scan

The most important figure-of-merits for the NOEM mirror are the ER and switching displacement Δy. These quantities are measured by implementing a similar measurement scheme as introduced previously, but using the CTL laser and the fine grating of the spectrometer instead. The fine grating has a significantly higher resolution (0.05 nm) than the coarse one, and the CTL laser allows for a more controlled scan over frequencies than with the SuperK. For each voltage step, the frequency is scanned over a narrow range of interest, in this case between 938.8 and 940 nm. The SuperK data (fig. 5.2.a) shows that at around these frequencies multiple peaks and a clear dip in transmission is observed along increasing voltages, advantageous for extracting the ER. The results of the CTL scan are shown in fig. 5.7.a, showing an overall similar change in transmission as with the SuperK. The fringes have an FSR of 0.31 nm, and could therefore not have been detected with the coarse grating used in the SuperK measurements. They do not exhibit a similar shift in frequency at the transmission dip as the fringes in the SuperK measurements. To extract the ER and switching displacement, a cross-section along the voltages is taken at 939.55 nm (peak of a fringe), and the S-matrix model parameters are subsequently adjusted to match the data in a similar fashion as in the previous section. This results in slightly different parameters than for the SuperK data, with a device stiffness of $k_T = 0.59$ Nm^{-1} and starting gap $d_0 = 97$ nm providing the best match.

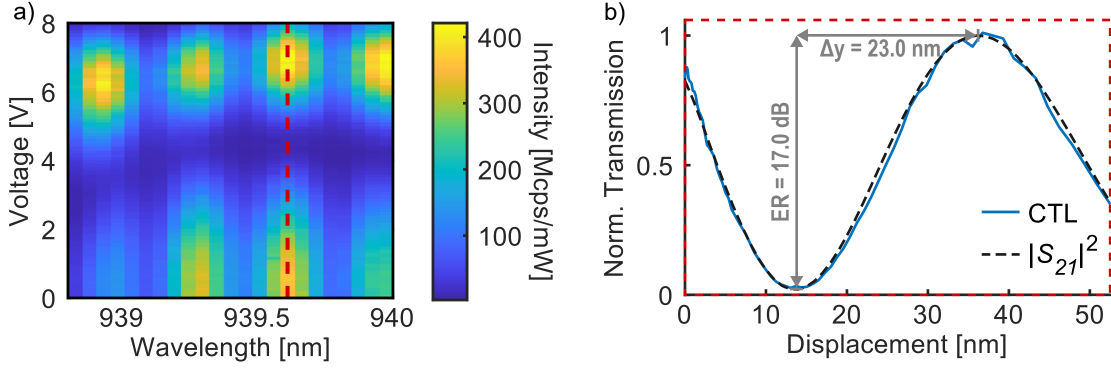

Figure 5.7: High-resolution voltage sweep measurements. a. Transmission voltage-sweep measurement, over a narrow range of wavelengths with the CTL laser. The higher resolution of the fine grating reveals fringes not previously visible, but a similar overall tuning behaviour. **b.** Transmission as a function of displacement at fixed wavelength of 939.55 nm. The measured data (blue line) yields an extinction ratio (ER = 17.0 dB) and switching displacement (Δy = 23.0 nm). The fitted S-matrix model (black dashed line) shows good agreement to the data.

Ideally, the two waveguides of the DC should be identical, but due to fabrication variations, this might not be the case. This can be incorporated into the model by including an amplitude term to the symmetric and anti-symmetric modes in the transmission and reflection coefficients:

$$t = \frac{1}{2}\left(a_S e^{-i\beta_S L_c} + a_{AS} e^{-i\beta_{AS} L_c}\right), \tag{5.5}$$

and

$$r = \frac{i}{2}\left(a_S e^{-i\beta_S L_c} - a_{AS} e^{-i\beta_{AS} L_c}\right). \tag{5.6}$$

In the ideal case $a_S = a_{AS} = 1$. The dip in transmission from the model can be fitted to the transmission dip of the measured data, and they are matched for the values $a_S = \sqrt{1.14}$ and $a_{AS} = \sqrt{0.86}$, indicating that the maximum achievable tuning contrast, or ER as was introduced in section 2.3.3, is limited by the symmetry of the coupled waveguides in the DC.

The CTL data cross-section at 939.55 nm and the fitted S-matrix model is plotted in fig. 5.7.b. The ER and Δy are extracted from the model as opposed to the data itself, as small fluctuations in the data can significantly affect the obtained values. The modelled data yield an ER of 17.0 dB and Δy of 23.0 nm. Measurements of corresponding values for the NOEM photon router (containing only the DC) are given in ref [49], which presents a splitting ratio of 23 dB and Δy of 65 nm. The splitting ratio differs from the ER in that it is a normalized value of the output of the two ports of the router, which cannot be measured directly in the NOEM mirror. The two values are therefore not directly comparable, but the obtained values suggest a worse tuning amplitude of the NOEM mirror. However, similar measurements with the CTL laser on devices with different parameters to the one presented here yielded ERs up to 23 dB, comparable to the NOEM photon router value. The switching displacement shows a significant improvement over the NOEM

photon router, as was expected since light propagates through the DC coupler twice in the NOEM mirror. In fact, the NOEM mirror can achieve a π-shift in intensity in less than 50 nm waveguide displacement.

5.4 Concluding remarks

In conclusion, the measurements to characterize the optical properties of the NOEM mirror with a broadband white-light source revealed tuning of the transmission signal through the device over a broad wavelength range of 35 nm, corresponding to the bandwidth of the SEG out-couplers. The insertion loss of the device is not directly measured, but normalizing the NOEM mirror data to that of nano-beam waveguide indicates significant losses of up to 8.2 dB, which cannot be accounted for solely by propagation losses. Measurements focused on directly characterizing the optical losses of the device were attempted but inconclusive, prompting future works to accurately determine the device loss. The theoretical S-matrix model shows good agreement with the measured data, and accurately depicts the tuning behaviour of the NOEM mirror, as well as most (but not all) of the dispersive nature of the device. On top of that, it can also give information on the structural and geometrical properties of the device, with a good fit to the data found for a coupling length of 22 nm, device stiffness of 0.64 Nm^{-1}, and starting gap distance of 96 nm. High-resolution measurements at around 940 nm show the high tuning performance of the device, with a full switch in transmission achievable with a waveguide displacement of only 23 nm. Indeed, a full π-shift in transmission is obtainable with less than 50 nm waveguide displacement. An ER of 17.0 dB was measured for the presented device, corresponding to an drop in the transmission signal of up to 98 %. NOEM devices with different structural parameters have been found to yield ERs of up to 23 dB.

Finally, two observations not presented in the main chapter text that are required to give a complete understanding of the NOEM mirror is discussed here. First, the measurements presented here were conducted at RT, integration with QDs require cryogenic temperatures. Measurements on other NOEM mirror devices conducted at both RT and 10K indicate that the NOEM mirror exhibits the same tuning behaviour at cryogenic temperatures, but that cooling down may have an impact on structural properties such as the device stiffness and starting gap distance, which affect the overall performance of the device. A more detailed analysis is required to draw conclusions on the thermal impact on the device performance. It is also worth noting that the transmission of the SEGs were found to be blue-shifted by approximately 25 nm after cool-down. The second important thing to note, is that the measurements conducted here technically do not prove the "mirror" properties of the device - the results merely show the ability to extinguish the transmission going through the device. It has however not been proven that the extinguished signal is instead reflected to the input port. As was mentioned in the beginning of the chapter, measuring the reflected signal is not possible on this device. Given the good agreement between the measured data and the S-matrix model for the transmitted signal, it is however a fair assumption to make that the reflected signal is similarly emulated by the S-matrix model.

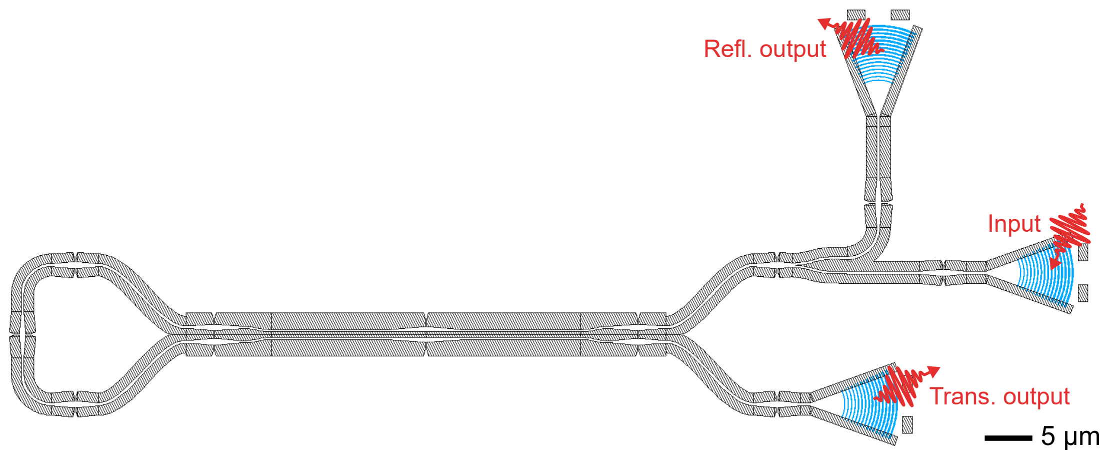

Figure 5.8: Proposed revision of the NOEM mirror to measure the reflected signal. The input arm of the mirror is split into two, each of which leads to an SEG coupler. The structure allows for measuring both the transmitted and reflected signal simultaneously, which is required to verify the anti-correlation between the two, predicted by the S-matrix model.

Future works should nevertheless attempt to prove this directly. A suggestion for a tailored NOEM mirror device capable of directly measuring both the transmitted and reflected signal is presented in fig. 5.8. Measurements on such a device should help confirm the anti-correlation between the transmitted and reflected signals, as predicted by the S-matrix model.

CHAPTER 6

Characterization of the tunable NOEM phase shifter

Tailoring the emission properties of single photon sources is a crucial step for creating efficient quantum photonic circuits. Minimizing the losses and impurities of the emitted photons is key, and even directing all emitted photons in the correct direction remains a challenge. As was discussed in section 2.3.3, the reason for this is that a QD embedded in a waveguide has an equal probability of emitting into either direction. As most circuit architectures only use photons emitted into one direction, those emitted in the "wrong" direction (50 % of the total counts) are effectively lost. Photonic-crystal mirrors integrated in the waveguide can reach extreme reflectivities,

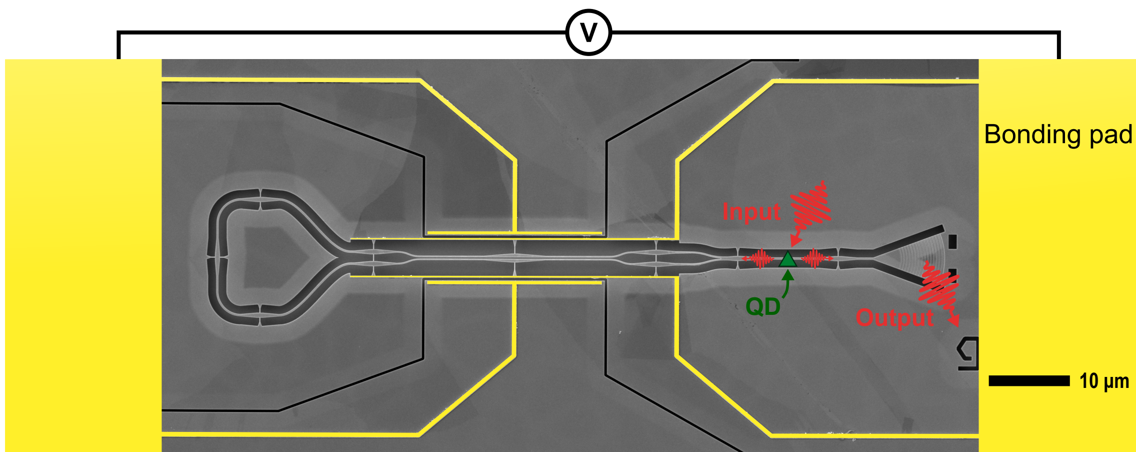

Figure 6.1: False-colored SEM of the NOEM phase shifter. A QD located within the structure at the approximate position of the green triangle is located. In all measurements the QD is excited above band from the top, and the QD emission is collected at the single output port. For voltage sweep measurements a bias voltage is induced between the electrodes (highlighted in yellow). The bonding pads are shown closer to the device than de facto for illustrative purposes.

but are not suitable candidates in solving this issue, as they offer no control of the phase of the reflected light, and therefore no control of the vacuum electric field amplitude at the position of the QD (which is inherently random from fabrication). This vacuum electric field is responsible for the spontaneous emission of an integrated QD, and controlling the phase is therefore decisive in controlling the emission properties of the QD.

In this work, a novel integrated device towards this goal has been proposed - the tunable NOEM phase shifter, pictured in fig. 6.1. According to the developed S-matrix model, the device should be capable of tuning the phase of the reflected field, thereby shifting the vacuum electric field around the QD and modifying its emission. This is done by varying the gap distance of the parallel waveguides in the central DC through a voltage bias applied between pairs of electrostatic actuators. In this chapter, the results of measurements to characterize the tuning of a QD's emission using the NOEM phase shifter is presented. First, the process of localizing and identifying a suitable QD is presented. Next, the emission of a QD within the NOEM phase shifter is collected for different voltage biases, and the results are compared to the predictions from the S-matrix model. Finally, lifetime measurements are conducted to directly determine the change in the spontaneous emission rate of the QD. All measurements are performed at 10 K.

6.1 Quantum dot localization and characterization

Figure 6.1 shows a NOEM phase shifter fabricated on the LoopSwitchB sample, which will be investigated in chapter. Due to the random spatial distribution of the QDs on the sample, the challenge becomes locating a QD at an optimal position in the device. As indicated on the figure, this optimal placement is on the single waveguide region before the SEG out-coupler. In this region, the properties of the vacuum electric field should be predicted by the S-matrix model - for other locations, say in one of the arms of the y-splitter, the field may look entirely different. A suitable QD candidate is located by scanning the PDL spot on the waveguide region from the top, while looking at the spectrum of light collected at the SEG port. This follows the above-band excitation scheme presented in section 2.1.2. The localization is best accomplished with the coarse grating of the spectrometer, as this yields higher counts. Once a bright and narrow emission line of a QD has been detected, the exact position of the laser spot can be fine-tuned by optimising the QD emission counts with the fine grating of the spectrometer. Due to a low QD density in the LoopSwitchB sample, only a single satisfactory QD located within the waveguide region of a NOEM phase shifter device was located, which will be denoted QDA. To verify that this emission line originates from the excitonic transition of a QD, the power of the excitation laser is swept from 0.01 µW to 0.44 µW, with spectra collected at each step. With increasing excitation power, emission coming from a QD is expected to saturate, and the FWHM of the emission line start to broaden, an effect known as *power broadening*.

The results of this power sweep are presented in fig. 6.2.a, showing a few select spectra at powers of interest. The emission line from QDA is found at a rather short

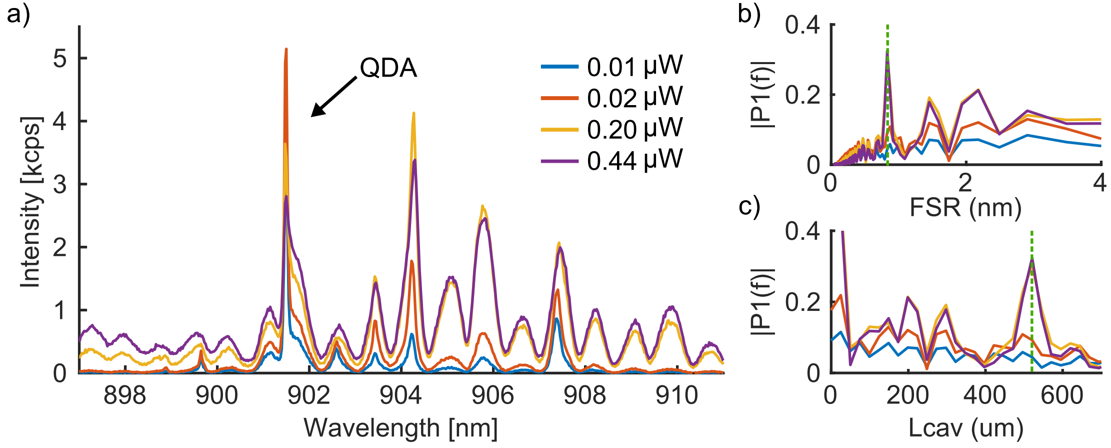

Figure 6.2: Power sweep measurements. a. Spectra of light collected from the output port for different excitation powers. A bright and narrow QD emission line is present at 901.5 nm that increases and subsequently decreases. Regularly spaced fringes are visible that become more pronounced with increasing power. **b.** Fast fourier transform of the spectra. A clear peak (green dashed line) is found at FSR = 0.83 nm. **c.** Corresponding optical cavity length (in air). The peak at L_{cav} = 520 µm corresponds to an optical cavity length of 97 mu, when divided by the estimated group index of the device. This value is in agreement with the approximate distance between SEG and loop in the device.

wavelength of 901.5 nm, but is distinctively narrow and bright, indicative that it is indeed emission from a single QD excitonic transition. The QD emission peak is qualitatively seen to initially increase, but subsequently drop significantly as the excitation power is increased. The emission is muddled by the presence of clear cavity fringes in the captured spectra, making it difficult to directly isolate the QD emission. Fast Fourier transforms of the spectra are plotted in fig. 6.2.b, where a clear peak emerges at higher powers at an FSR of 0.83 nm. Figure 6.2.c shows that these fringes correspond to an optical cavity of length of 520 µm (given by eq. 5.4), assuming propagation in air. Dividing this by the estimated group index for the device n_g = 5.36 yields an optical cavity length of 97 µm, which matches the estimated distance between the SEG coupler and loop in the NOEM phase shifter of $\sim$ 94 µm, suggesting that the fringes stem from the device itself, due to a finite reflection coefficient of the SEG. Emission into the cavity modes is likely the result of exciton recombination in the InAs wetting layer in the sample, a byproduct of using the above-band excitation scheme. The wetting layer emission has a central wavelength of $\sim$ 870 nm, but with a tail that stretches up to much higher wavelengths. At wavelengths above $\sim$ 903 nm, the SEG transmission efficiency increases dramatically, which explains the clear increase and subsequent decrease in cavity fringe amplitude for higher wavelengths.

To accurately investigate the saturation behaviour of QDA, the emission line is fitted, and the counts are integrated over the width of the peak for all powers. The fitting is however complicated by the overlap with the cavity resonances, which must be subtracted before fitting the peak. As shown in fig. 6.3.a, the background (red line with black crosses) is estimated and subsequently subtracted from the data

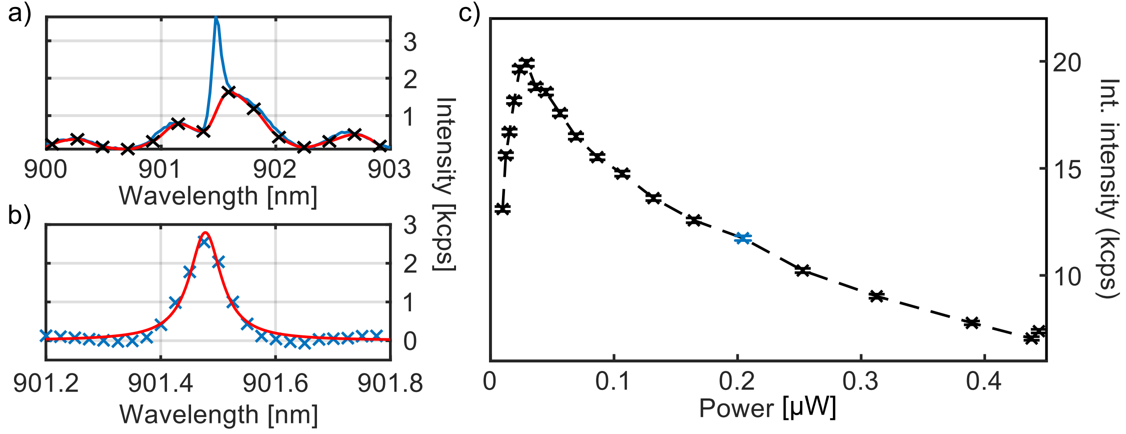

Figure 6.3: Corrected emission of QDA at different powers. a. QD emission spectrum at 0.2 µm (blue line) with the background fitted (red line, crosses). **b.** Same as **a.**, but after subtracting the fitted background. The QD emission is fitted with a Lorentzian function. **c.** Corrected emission of QDA as a function of power. The QD is found to saturate at $P_{sat} \approx 0.3$ µW, and subsequently decrease. The decrease may be a result of a coupling of the QD emission to the cavity modes. The blue data point in **c.** indicates the spectra shown in **a.** and **b.**

(blue curve), producing a corrected QD emission peak as shown by the blue crosses in fig. 6.3.b. The resulting peak is then fitted with a Lorentzian function (red line), and the counts over the line width are integrated. The corrected, integrated QD fluorescence counts as a function of excitation laser power is presented in fig. 6.3.c. The figure shows that QDA is found to saturate at an excitation power of $P_{sat} \approx 0.03$ µW. The saturation power is an important parameter to consider, as further investigations of the QD emission rate should be conducted well below P_{sat}. Power sweep measurements well below saturation were not conducted in this work, but should be carried out in future works, as such can provide information on the exact excitonic transition being addressed [73].The drop in intensity at higher powers ($P > P_{sat}$) is likely caused by the non-resonant coupling to the cavity modes. In fig. 6.2.a, a slight shift in the cavity resonances' wavelengths is seen at higher powers. Increasing the QD-cavity detuning leads to a decrease in the QD saturation intensity [74], which is likely the reason here. It is also worth noting that as the width of the QD emission line and cavity resonances are very similar, the background fitting will likely include some of the QD emission signal, and more so for higher powers, making the intensity drop more pronounced.

6.2 Tuning of the quantum dot emission rate

To characterize the NOEM phase shifter's capability in tuning QD emission, the QD identified in the previous section (QDA) is pumped above band from the top with the PDL, at a power well below QD saturation $P = 0.01$ µW. A voltage sweep protocol similar to section 5.1 is implemented, where the voltage across the electrodes is scanned from 0 V to 9 V in steps of 0.5 V, and spectra are recorded

at each step with the fine grating, collected from the SEG coupler. Figure 6.4 plots the captured spectra for different voltages (in integer steps for better clarity), with the black crosses and dashed line tracing the peak of the QD emission.

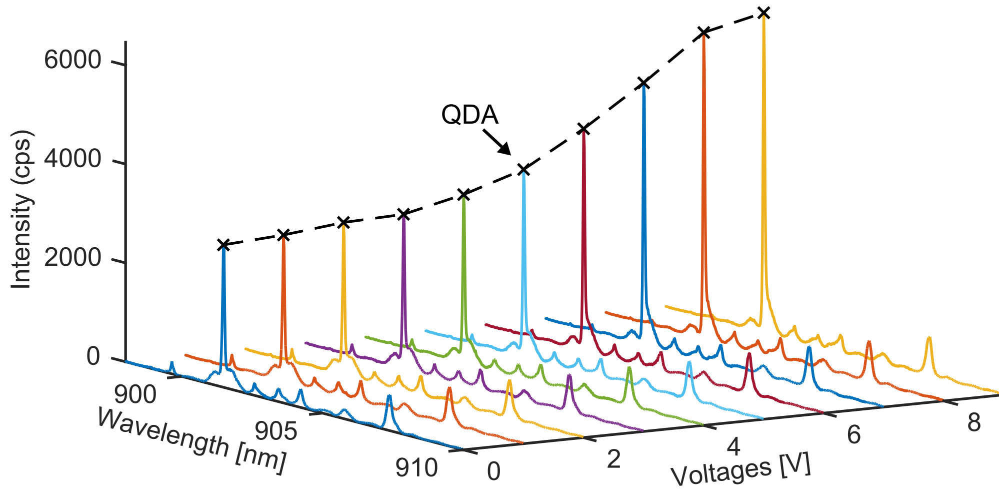

Figure 6.4: Tuning of the quantum dot emission. As the voltage across the electrodes is increased, the emission from QDA collected at the output port is significantly increased. The black dashed line and crosses track the peak of the emission line as a guide for the eye.

The presented data have been normalized to an excitation laser power of $P = 0.01$ µW to account for power fluctuations. A clear increase in the emission peak height with voltage is observed. There is little emission into the cavity modes due to the low excitation laser power, but as there is a clear overlap between the QD emission and cavity mode, this background emission must once again be subtracted. Similarly to section 6.1, the background emission is fitted and subtracted, the resulting QD emission line fitted with a Lorentzian function, and the counts are integrated. The corrected, integrated counts of QDA as a function of waveguide displacement of the DC is shown in fig. 6.5.a. The waveguide displacement is given by eq. 2.16 and nominal values for the specific device, with the corresponding voltage-displacement curve plotted as the brown dashed line in fig. 6.5.b.

The NOEM phase shifter containing QDA has the following structural parameters: shuttle electrode length $L_s = 26$ µm, shuttle electrode width $w_s = 260$ nm, coupling length $L_c = 20$ µm, and starting gap distance $d_0 = 150$ nm. The estimated performance of the device is gauged by considering two couplings. The first is the electro-mechanical coupling, specified by the first two parameters, and is for this device expected to be very good. This is reflected in the maximal achievable waveguide displacement, which for this device is 73 nm at 9 V. The opto-mechanical coupling, i.e. the change in the optical properties of the device with waveguide displacement, is due to the large starting gap distance and shorter coupling length expected to be less than optimal. The data presented in fig. 6.5.a show that the QD emission rate has been increased by a factor of 2.09 for a waveguide displacement of 73 nm. The range of the tuning is however not entirely clear, as no minima or maxima er present in the data.

6.2.1 Comparison to the S-matrix model

Next, an attempt to match the S-matrix model of the NOEM phase shifter introduced in section 2.3.3 to the data is made, under the assumption that the decay rate is proportional to the vacuum electric field amplitude $\gamma \propto |E|^2$. The measured data is influenced by many factors, and obtaining an exact fit is therefore not relevant. Nonetheless, to show that the developed S-matrix model can roughly describe the observed tuning behaviour, an adequate match to the data is found by varying the parameters: coupling length L_c, starting gap distance d_0, device stiffness k_T, device loss a_L, and an arbitrary proportionality constant α. The numerical simulations used for the model are however only defined for wavelengths between 920 nm and 990 nm. The difference to the QD emission wavelength of 901.5 nm can however be compensated for by varying the other fitting parameters. A satisfactory fit to the data is presented in fig. 6.5.c.

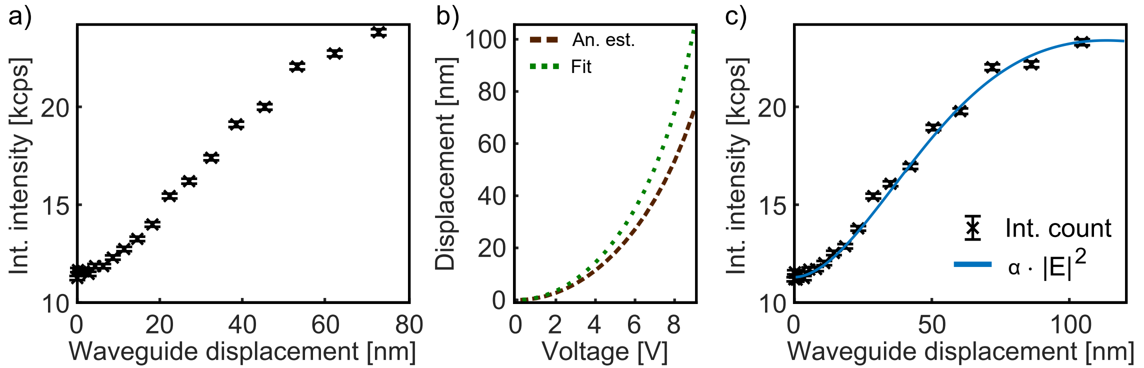

Figure 6.5: Tuning of QDA emission. a. Integrated counts of the QDA emission line as a function of waveguide displacement, calculated by correcting for the background data and fitting the emission line with a Lorentzian function (see fig. 6.3). The displacement is found from eq. 2.16 and nominal device values. **b.** The deviation in the tuning curves using the nominal (brown dashed line) and adjust (dotted green line) device stiffness k_T indicates that the device is more flexible than expected, as was the case for the NOEM mirror. **c.** The simulated vacuum electric field can be made to match the data by varying the parameters of the S-matrix model.

The parameters used for this fit (nominal values) are: L_c = 28 µm (27.8 µm), $d_0 = 135$ nm (150 nm), $k_T = 0.55$ Nm^{-1} (0.69 Nm^{-1}), and $a_L = 83$ %. A few things are here worth noting. First, a good match was achieved with values that are close to the nominal values, within what can be justified by fabrication imperfections. Second, as was also the case for the NOEM mirror, the device stiffness and therefore maximal achievable displacement seem to have been underestimated. The voltage-displacement curve for the adjusted k_T is plotted as the green dotted line in fig. 6.5.b, implying a maximal achievable displacement of 104.6 nm. Finally, recalling eq. 2.48, losses can be incorporated into the model by reducing the amplitude of the reflected wave in the device, ultimately resulting in a decrease in the tuning amplitude that can be achieved by the device. A loss of 0.83 % corresponds to 7.7 dB, comparable to the measured loss of the NOEM mirror of 8.2 dB.

6.2.2 Temporal shift

Measurements to characterize the repeatability of the emission tuning of QDA with the NOEM phase shifter revealed a curious phenomenon: the starting point in the tuning curve seemingly shifts over time. Figure 6.6.a shows a similar voltage sweep capturing the emission of QDA as was presented in section 6.2, conducted 49 minutes after the voltage sweep measurements presented previously. The data is similarly corrected for background emission and fitted with a Lorentzian function, and the tuning of the integrated counts is compared to the previous measurement in fig. 6.6.b (assuming a similar voltage-displacement curve given by nominal device values). The two time-separated measurements show starkly different tuning

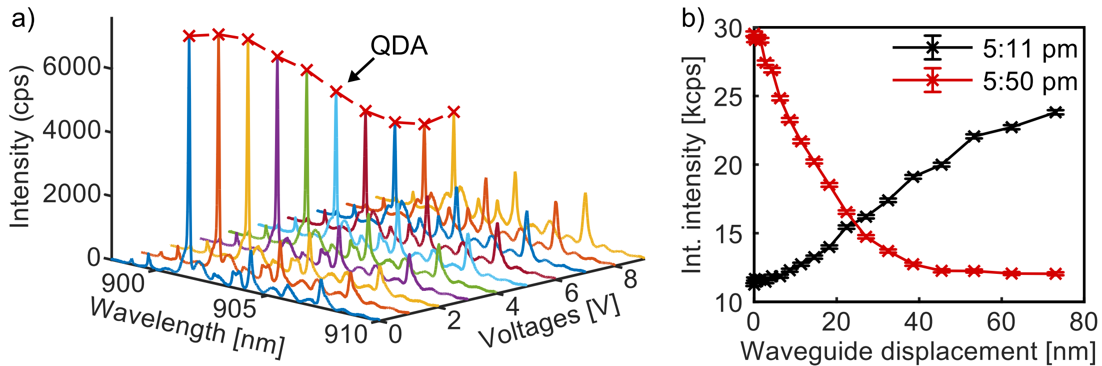

Figure 6.6: Tuning of the quantum dot emission at a later time. a. QD emission voltage sweep measurement conducted 49 minutes after the one presented previously. The red dashed line and crosses trace the peak of the emission line as a guide for the eye. **b.** Integrated counts of QDA emission for the early (black curve) and late (red curve) measurements. A dramatic change in the tuning behaviour of the emission of QDA is observed.

behaviours - the early measurement shows a clear increase in counts for larger gap distances, while the later measurement shows a sharp decrease. Assuming that this behaviour is accurately captured by the S-matrix model, this difference corresponds to changing the initial gap distance of the modelled device, in other words changing the "starting point" of the tuning curve. This also explains the changes in intensities being different - the early measurement shows a factor ~ 2.09 increase in the intensity, while the later shows a slightly larger decrease of a factor ~ 0.41, despite it reaching an apparent minimum. A large starting gap distance leads to less emission tuning with displacement, as compared to a smaller starting gap distance. Several possible explanations for this temporal shift were investigated during the course of the experiments, but none proved conclusive. Most notably, large fluctuations in temperature could have an impact on the structural properties of the device, altering its tuning capabilities. The temperature was however observed to be stable between measurements. The spectral overlap between cavity mode and QD emission will have an impact on the tuning behaviour, which has not yet been inspected. In the following, a possible explanation for the temporal shift due to the spectral shift of the cavity modes over time is given.

6.2.3 Spectral tuning of cavity mode resonances

In section 6.2.1, the S-matrix model for the NOEM phase shifter was matched to the data, showing good agreement between predicted and recorded data. As noted before, a precise fit to the data is not feasible, as this would have to account for a multitude of factors. However, further analysis indicates that disregarding this limitation, the developed S-matrix model still fails to tell the entire story. Recalling eq. 2.48, the developed model describes the vacuum electric field forming a standing wave surrounding the emitter, altered by a change of phase induced by the device, that is described by the S-matrix. It is here necessary to make an important distinction: such a model only describes the *spatial* overlap of the emitter and surrounding field, but does not account for their *spectral* overlap. In other words, the model assumes that the exciton transition and electric field mode are resonant. However, the results obtained in this work show QD emission and surrounding cavity modes that are off-resonance, with a detuning that changes with voltage. This is highlighted in fig. 6.7, which shows a zoom-in of the results of the two voltage sweep measurements separated by time presented earlier for 0 V and 9 V. Two cavity modes are seen

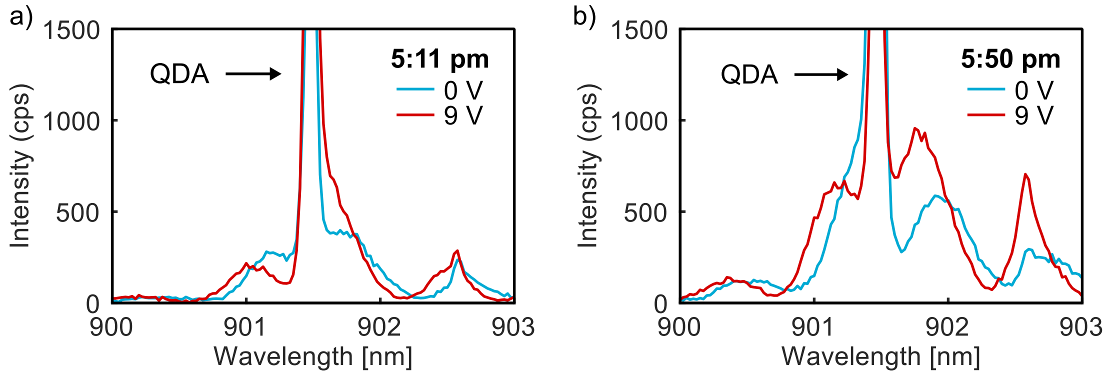

Figure 6.7: Tuning of the cavity resonances. a. Zoom-in of the captured spectra at 0 V (light-blue curve) and 9 V (red curve) for the early measurement. The emission line of QDA is centered between the two cavity resonances at 0 V, which are shifted towards lower wavelengths at 9 V. **b.** Same as **a.**, but for the later measurement. The initial positions of the cavity resonances at 0 V have been shifted, so that the QDA emission line now nearly overlaps with the left resonance. The cavity resonances are similarly shifted towards lower wavelengths at 9 V. The clear shift in the cavity resonances' wavelengths between **a.** and **b.** is the likely cause of the change in tuning behaviour over time, and indicates that it is the spectral tuning of cavity resonances that is mainly responsible for the QD emission tuning.

that overlap with the QD emission mode. The amplitudes of these cavity modes are too small for Fourier transformation analysis, but it is assumed that these cavity fringes are identical to those previously analysed, found to originate from the device. As the voltage is increased, the cavity modes are spectrally shifted towards lower wavelengths, affecting the spontaneous emission rate of the QD. Numerical simulations of the DC reveal that the effective refractive index in the DC changes with gap distance, which according to eq. 5.3 would result in a shift in the wavelength of the cavity mode.

The Purcell enhancement of the spontaneous decay rate of a QD emitter in a non-resonant cavity is given by [22]:

$$F_P = \frac{\Gamma_{cav}}{\Gamma_{hom}} = \frac{3Q}{4\pi^2 V_m} \frac{(2\kappa)^2}{4\Delta^2 + (2\kappa)^2} \frac{|\mathbf{r_{vc}} \cdot \mathbf{E}(\mathbf{r_0})|^2}{|\mathbf{r_{vc}}|^2 |\mathbf{E_{max}}|^2}, \tag{6.1}$$

where Q and V_m are the cavity mode quality factor and mode volume, and Δ and 2κ are the exciton transition-cavity resonance detuning and FWHM of the cavity mode. Finally, $\mathbf{r_{vc}}$, $\mathbf{E}(\mathbf{r_0})$ and $\mathbf{E_{max}}$ are the transition dipole moment, electric field at the dipole position and maximum electric field, respectively. The distinction between tuning mechanisms is made clearer by eq. 6.1: the spontaneous emission rate can either be enhanced *spectrally* by changing Δ, or *spatially* by changing $\mathbf{E}(\mathbf{r_0})$. It is important to clarify that no matter which mechanism is responsible, the end result is the same: a change in the LDOS responsible for the spontaneous emission of the QD emitter. As previously discussed, the cavity modes appear because of a finite reflection coefficient of the SEG out-coupler. For perfectly non-reflective SEGs, these cavity modes disappear, and the tuning of the spontaneous emission rate is expected to be governed entirely by the change in spatial overlap predicted by the S-matrix model. The change in spontaneous emission rate due to the spectral tuning of a cavity mode can be written:

$$F_{P,cav} = \frac{F_{P,f}}{F_{P,i}} = \frac{\Gamma_f}{\Gamma_i} = \frac{(2\kappa_f)^2(4\Delta^2 + (2\kappa_i)^2)}{(2\kappa_i)^2(4(\Delta + \delta\lambda)^2 + (2\kappa_f)^2)}, \tag{6.2}$$

where $F_{P,f}$ (Γ_f) and $F_{P,i}$ (Γ_i) are the Purcell enhancements (spontaneous emission rates) at 9 V and 0 V, respectively, Δ is the initial detuning at 0 V, and $\delta\lambda$ is the shift in cavity resonance wavelength at 9 V. The FWHM of the cavity resonance at 9 V and 0 V is given by $2\kappa_f$ and $2\kappa_i$, respectively. The equation assumes there is no change in the spatial overlap, and therefore only takes the spectral tuning into account.

The total Purcell enhancement by the spectral tuning of the two overlapping cavity resonances, which are denoted *left* and *right* according to their spectral position compared to the QD emission, can be estimated by extracting approximate values from fig. 6.7 and using: $F_{P,total} = F_{P,left} \cdot F_{P,right}$. For the early measurement presented in fig. 6.7.a, the total Purcell enhancement is found to be $F_{P,total} \approx 0.55 \cdot 2.47 = 1.36$. For the later measurement presented in fig. 6.7.b an enhancement of $F_{P,total} \approx 0.36 \cdot 1.31 = 0.47$ is found. Comparing these to the measured changes in QD emission of 2.09 and 0.41 for the early and late measurements, respectively, indicates that the spectral cavity tuning has an impact on the total change in emission, but to varying degree. It is however worth noting that eq. 6.2 presents a highly simplified picture, and does not take the overlap between the two cavity modes into account, for example. It is also very sensitive to small fluctuations of its parameters. Further measurements nonetheless indicate that the majority of the tuning is due to the spectral cavity tuning, with limited contributions from the spatial mode tuning. This is corroborated by two observations: the limited tuning in the absence of cavity fringes, and the temporal shift discussed in 6.2.2. The latter is highlighted by looking at the spectra for 0 V (light blue lines) for both measurements, shown in fig. 6.7.a and 6.7.b. A clear shift in the cavity resonance wavelengths between the two measurements is visible, which would explain

the change in the overall tuning behaviour of the QD emission. At the time of writing, it remains unclear what causes this temporal shift. One possible explanation is that the shift could be due to a drift in the gap distance of the DC, but further investigations are required for a conclusion to be made.

6.2.4 Impact of device losses

Voltage sweep measurements as those presented previously have been conducted on QD's without the presence of cavity modes. These measurements were performed on devices on the NEMSV3 sample containing near fully-undercut SEGs (see fig. 3.5.b as an example), which should possess minimal reflection coefficients. Voltage sweep measurements showed little-to-no tuning of the QD emission throughout. While this may partly be due to fabrication imperfections such as damages to the metal electrodes (see fig. 3.4.a), it is believed that it is mainly caused by the limited spatial mode tuning, which in turn is due to losses in the device. This further highlights how the emission tuning of QDA was likely mainly the result of spectral tuning of the surrounding cavity resonances. The losses in the NOEM phase shifter can not be measured directly, but assuming that the losses are comparable to those of the NOEM mirror, measured to be 8.2 dB, the S-matrix model shows that the maximal achievable tuning is by a factor of 1.83, corresponding to an extinction ratio of $ER = 2.63$ dB. This is illustrated by the red curve in fig. 6.8.a.

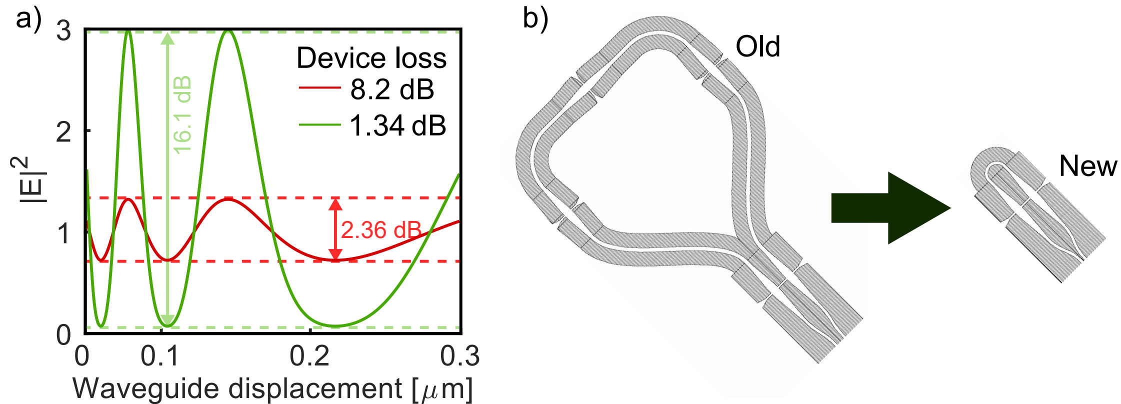

Figure 6.8: Impact of losses to device performance. a. The vacuum electric field amplitude given by the S-matrix model for device losses comparable to the NOEM mirror (red curve) shows a limited tuning with gap distance of only 2.36 dB. Reducing the device losses to 1.34 dB (green curve) comparable to the NOEM photon router is feasible. In this case, the tuning amplitude is significantly improved to 16.1 dB. **b.** Redesigned loop for the device. The significantly shorter length should help reduce propagation losses.

As discussed in section 5.2.1, the source of these losses remains unclear and requires more in-depth analyses. The limiting factor in the tuning of the QD emission by the NOEM phase shifter is therefore evidently device losses. An attempt was made to reduce device losses by re-designing the loop of the NOEM phase shifter, as depicted in fig. 6.8.b. The length of the new loop has been significantly shortened, which should reduce propagation losses. NOEM phase shifters with this amended loop were

fabricated and characterized on the NEMSV3 sample, but the updated design did not show a significant improvement over the older. Losses on the NEMSV3 sample are however expected to be even larger than those on the LoopSwitchB sample due to fabrication imperfections, and the device yield rate for the re-designed NOEM phase shifters was very low.

To gauge the full potential of the NOEMS phase shifter, the performance of the device with losses comparable to another state-of-the-art NOEMS devices is presented. The tuning of the vacuum electric field given by the S-matrix model, with losses similar to the NOEM photon router, is shown as the red curve in fig. 6.8.a. The NOEM photon router bears much resemblance to the NOEM phase shifter, and has an insertion loss of 0.67 dB [38]. To account for light travelling twice through the DC, this value has been doubled in fig. 6.8.a. A NOEM phase shifter with a device loss of 1.34 dB shows a significantly improved tuning amplitude of up to a factor of 41.05, corresponding to an extinction ratio of $ER = 16.1$ dB. Future works on the NOEM phase shifter device should therefore emphasize optimizing the device parameters and improving nano-fabrication processes towards the goal of minimizing device losses.

6.3 Fluorescence lifetime measurements

To complete the investigation of the NOEM phase shifter, the change in the spontaneous emission rate of QDA as a function of voltage is measured directly by time-resolved fluorescence lifetime measurements. The QD is again pumped above-band with an excitation laser power of $P = 0.01$ µW, well below the QD saturation level, and the collected emission is sent through the filtering setup presented in fig. 6.9.a. The grating can be aligned to spatially filter the QD emission line, which is subsequently collected and sent to a single-photon avalanche diode (SPAD). In the SPAD, a current is generated upon the detection of a photon. This electric signal is then sent to a PicoHarp 300 time-correlated single-photon (TSCPC) device that resolves the photons in the time-domain. The measured photon arrival times are adjusted relative to a synchronization signal emitted by the PDL. A high signal-to-noise ratio is achieved by integrating over thousands of photon counts until a specified threshold is reached. The measurement is repeated for two different voltage biases that have previously been measured in a voltage-sweep measurement to correspond to a maximum and minimum of the QD emission rate.

The results of the fluorescence lifetime measurements are presented in fig. 6.9.b and 6.9.c, corresponding to a low emission rate (5 V) and high emission rate (0 V), respectively. Initially, the measured correlated photon counts (blue curves) do not only represent the decay rate of the QD, as they are convolved with the instrument response function (IRF) of the measurement setup. The IRF (black curves) is measured by aiming the excitation laser on an empty part of the sample and correlating photon counts from the scattered light. The IRF is deconvoluted from the measured photon correlations, which are then fitted by a single exponential. The optimal fit is found by varying the offset of the IRF and the starting fit time. The resulting fits are shown as the red curves, with the green curves indicating the fits prior to the fit starting time. The low χ^2-values and correlation factors indicate

that the exponential function accurately reproduces the data, while not over-fitting.

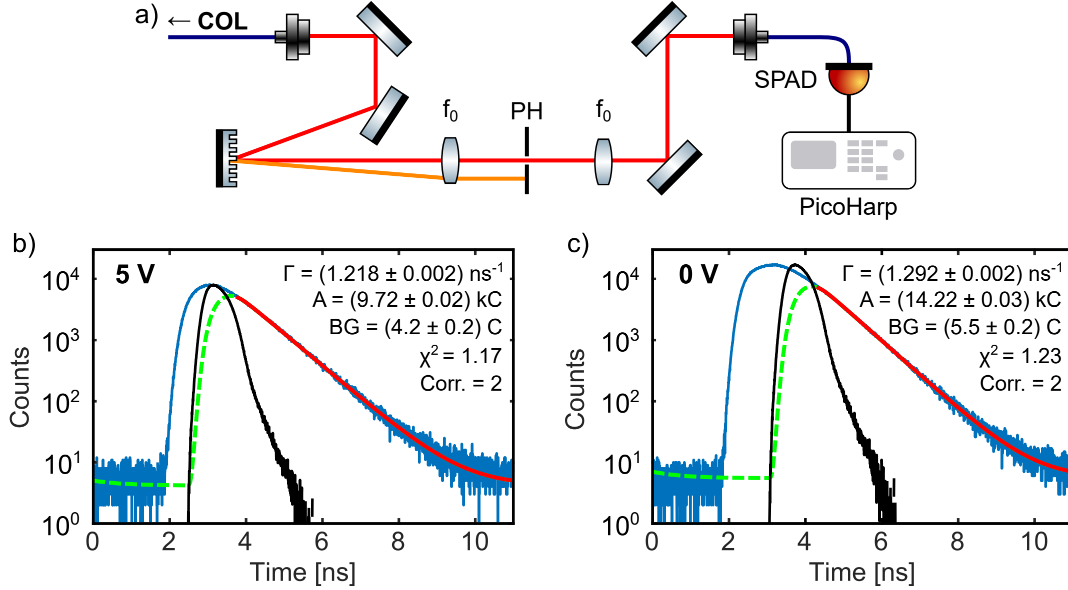

Figure 6.9: Quantum dot fluorescence lifetime measurements. a. Free-space grating filter setup. The QD emission line is filtered with a grating, and an SPAD and PicoHarp correlate the photon arrival times. **b.** Results of the lifetime measurements at 5 V. The photon counts (blue curve) are deconvoluted from the IRF (black curve), and are fitted with a single exponential (red curve) to extract the decay rate. The green dashed line indicate the fits prior to the selected starting point. The low χ^2-value indicate that the exponential function reproduces the data well, and the low correlation factor indicates that the data is not over-fitted. **c.** Same as **b.**, but at 0 V. The decay rate is found to only change marginally between the two voltages.

In the low counts case, the decay rate is found to be $\Gamma_{low} = (1.218 \pm 0.002)$ ns $^{-1}$, which is only marginally increased for the high counts case to $\Gamma_{high} = (1.292 \pm 0.002)$ ns $^{-1}$. The measured increase in the spontaneous decay rate is therefore only a factor of 1.06. The minimal change in decay rate is likely due to the temporal shift discussed previously. Changing the setup from a voltage sweep measurement to a lifetime measurement takes time, and integrating photon counts until a high enough signal-to-noise ratio is reached takes several minutes. During this time, the temporal shift may have changed the spontaneous decay rate. Secondly, right before commencing the lifetime measurement, the tuning curve of the QD emission resembled a "valley". This is the reason for choosing 5 V, instead of say 9 V, as this corresponds to a minimum. The contrast between high and low counts was therefore not optimal. It is anticipated that the change in the spontaneous decay rate be considerably higher in the absence of the temporal shift and for a higher contrast between low and high counts.

6.4 Concluding remarks

In summary, measurements to characterize the NOEM phase shifter's ability to tune the spontaneous emission rate of an embedded QD were conducted. By imposing a voltage bias of up to 9 V across the electrostatic actuators of the DC, the change in waveguide displacement resulted in a tuning of the spontaneous emission rate of the embedded QD by up to a factor of 2.44, corresponding to an ER of 3.8 dB. The measurements however cast doubt on the central mechanism responsible for the tuning, due to the presence of cavity resonances in the recorded spectra. These cavity resonances likely arise due to a finite reflectance of the SEG. The FSR of the cavity fringes were found to correspond to an optical cavity length in the device of 97 µm, comparable to the length between SEG and loop in the device of $\sim$ 94 µm. Whether the tuning is due to the phase shifter modulating the spatial mode of the vacuum electric field, as predicted by the S-matrix, or by tuning the cavity modes in and out of resonance with the QD emission, remains unclear. Adjusting the parameters of the S-matrix model, which only accounts for the spatial tuning, the model was made to adequately reproduce the measured data. However, measurements on a NOEM phase shifter fabricated on a different sample with no visible cavity resonances showed little-to-no tuning of the QD emission rate. Taking all things into account, it is here speculated that the spectral tuning of the cavity resonances is the dominant factor in the observed change in QD emission rate, with limited contributions from the spatial mode tuning. Irregardless of the exact mechanism, the end result is the same: a change in the LDOS responsible for the spontaneous emission of the QD.

The repeatability of the emission tuning was found to be severely inhibited by an apparent drift in the cavity resonances' wavelength over time. In fact, identical voltage sweep measurements conducted 49 minutes apart showed near anti-correlated behaviour. The fluorescence lifetime measurements of the QD demonstrated only a marginal tuning of a factor 1.06, likely also limited by the temporal shift. As the cavity resonances are always shifted towards lower wavelengths with voltage, the changing initial wavelengths of the resonances have a dramatic impact on the overall tuning curve of the QD emission rate. Potential sources of the temporal shift, such as temperature changes, were excluded. It is speculated that fluctuations in the gap distance of the DC may prove a viable explanation. Future works should attempt to quantify the temporal drift more precisely, for example by recording time-resolved emission spectra and tracking the cavity resonances' drift, in order to propose a conclusive hypothesis.

Significant device losses are predicted by the S-matrix model to have a detrimental impact on the spatial mode tuning amplitude (ER) of the QD emission rate. The current design of the NOEM phase shifter does not allow for measuring the losses directly, but they are expected to be comparable to the NOEM mirror, which already displayed unaccountably large losses. Losses are the likely explanation of the little-to-no tuning of the QD emission rate found for devices without cavity resonances. Reducing losses is expected to dramatically increase the performance of the NOEM phase shifter, and future works should therefore look to optimize the device structure and fabrication processes towards this end.

CHAPTER 7

Conclusion and outlook

The aim of this thesis was to present novel applications of the nano-opto-electro-mechanical directional coupler for the development of new on-chip functionalities. To this end, two new chip-scale devices were introduced: a mirror with adjustable reflectivity, and a tunable phase shifter. The thesis first presented the quantum dot emitters used in this work, as well as a derivation of how their spontaneous emission may be addressed by modifying the surrounding optical environment. The underlying coupled-mode theory governing the devices' ability to alter optical fields via an electro-mechanical tuning was presented. Using the S-matrix formalism, models were developed describing the devices' optical responses. The S-matrix formalism, in combination with the cascading junctions method, proved to be a powerful tool, and is expected to be integral in the development of future complex photonic architectures. The thesis presented the fabrication processes used to fabricate the devices, applicable for numerous other nano-scale photonic devices. The fabricated samples were characterized at both room temperature and cryogenic temperatures.

The nano-mechanical mirror demonstrated the tuning of a broadband coherent light source transmitted through the device, with a change in power of 17.0 dB over a mechanical switching displacement of only 23 nm. Similar fabricated devices with different structural parameters yielded extinction ratios of up to 23.0 dB. To the best of this author's knowledge, this device comprises a novel approach to chip-based adjustable reflectors with a state-of-the-art performance. A thorough study of the relevant literature yielded only one article with a comparable device, in which simulations of an on-chip tunable reflector with a theoretical maximum extinction ratio of 18.2 dB are presented [75].

Characterization of the nano-mechanical tunable phase shifter demonstrated the tuning of the spontaneous emission rate of an embedded quantum dot emitter of up to a factor of 2.44. The measurements revealed that the central mechanism responsible for this increase was in fact the spectral tuning of cavity resonances, as opposed to the spatial optical field modulation hypothesized by the S-matrix model. Improvements to the fabrication processes will however eliminate this unwanted spectral tuning, resulting in the change in spontaneous emission rate being governed entirely by the spatial modulation, which can be improved by reducing device losses.

There remains much to be done with these devices, and future works can progress in one of two directions: optimizing device performance, or combining them (and other integrated devices) to construct more advanced photonic structures. For the NOEM mirror, it remains imperative to directly prove the anti-correlation of the transmitted and reflected signals. This can be achieved with the device presented in fig. 5.8. Similarly, reducing the insertion loss of the device is critical for integration in QPICs. Reducing losses can be accomplished by improving the nano-fabrication processes to minimize the surface roughness of the sample [76], or by scaling down the length of the enclosed loop, as was shown in fig. 6.8.b. Another benefit of reducing device losses is that it would enhance the effectiveness of a potential cavity structure containing the mirror [56]. Figure 7.1.a presents a proposed structure comprised of a photonic-crystal Bragg mirror and the tunable NOEM mirror.

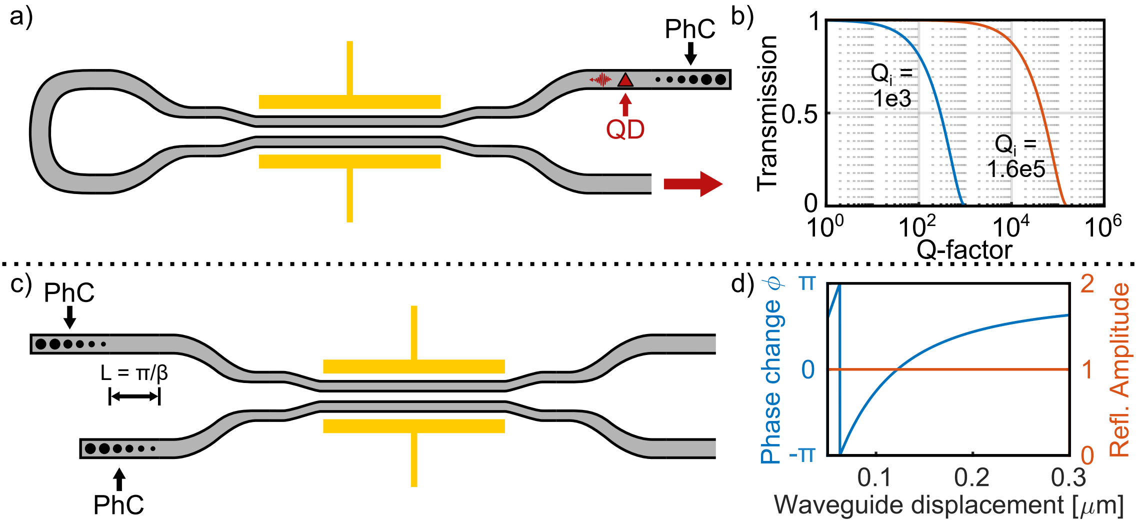

Figure 7.1: Proposed future NOEM devices. a. Schematic of tunable cavity device. A cavity is formed with a photonic crystal mirror (PhC) and the tunable NOEM mirror. A contained QD (red triangle) is Purcell enhanced. **b.** Trade-off between transmission and cavity Q-factor. As the Q-factor (Purcell enhancement) is increased, the transmission out of the cavity drops. Different intrinsic Q-factors (Q_i) indicate the impact of losses. **c.** Schematic of alternative tunable phase shifter. PhC mirrors are incorporated to the two arms of the directional coupler, separated by a distance corresponding to a π-phase shift. **d.** Phase change and reflection amplitude of the phase shifter. Numerical simulations of the DC and the S-matrix show that the device is fully reflective (orange curve, assuming no losses), with an induced change of phase depending on the DC gap distance.

The single-photon indistinguishability and emission rate of a quantum dot will be Purcell enhanced if placed inside the cavity, determined by the quality factor of the cavity [77, 78]. However, as shown in fig. 7.1.b, increasing the cavity quality factor leads to decreasing transmission out of the cavity. The NOEM mirror would here be a key asset, as its tunable reflectivity would allow for coherent control of these properties, so an optimal trade-off can be reached for the experiment at hand.

The tunability of the spontaneous decay rate of a QD by the NOEM phase shifter is manifestly affected by device losses. Reducing device losses is therefore

critical in improving the performance of the NOEM phase shifter. Advancing fabrication processes and shortening the device loop is similarly expected to further this goal. Specifically for the NOEM phase shifter, the contained y-splitter structure is expected to be a large source of radiative losses. These can be further reduced by optimizing the y-splitter geometry [79], or by incorporating a photonic-crystal-based y-splitter [80]. Alternatively, a NOEM phase shifter device completely disposing of the lossy y-splitter is here proposed, illustrated in fig. 7.1.c. This proposed device comprises the NOEM directional coupler with photonic-crystal Bragg reflectors integrated on two branches of the device. An asymmetry in the length of the two arms containing the reflectors are incorporated to induce a π-phase difference between them. This requires deterministic fabrication with a precision that is currently not possible, but advances in the fabrication methods may prove this feasible in the near future. The S-matrix for such a device is:

$$S = \begin{bmatrix} r^2 + t^2 & 0 \\ 0 & -(r^2 + t^2) \end{bmatrix} \tag{7.1}$$

An analysis of the S-matrix with values from numerical simulations of the directional coupler are presented in fig 7.1.d. The resulting device is fully reflective for all configurations of the directional coupler. The phase change induced by the device can be tuned by re-configuring the directional coupler. This phase shifter is therefore effectively similar to the one presented in this work, but is expected to have significantly smaller radiative losses, due to the shorter device length and the absence of a y-splitter junction.

The devices presented in this work constitute important building blocks for the scaling of quantum photonic experiments. They can readily be integrated and combined with other photonic devices to form complex photonic architectures, towards the goal of advanced, fully-integrated photonic quantum-information processing applications with multiple qubits.

Bibliography

[1] Thomas S. Kuhn. *The Structure of Scientific Revolutions*. University of Chicago Press, 1962.

[2] Michael A Nielsen and Isaac L. Chuang. *Quantum Computation and Quantum Information*. Cambridge: Cambridge University Press, 2010. DOI: 10.1017/CBO9780511976667.

[3] D. P. DiVincenzo. "Quantum Computation". In: *Science* 270.5234 (1995), pp. 255–261. DOI: 10.1126/science.270.5234.255.

[4] Dean Copsey et al. "Toward a scalable, silicon-based quantum computing architecture". In: *IEEE Journal of Selected Topics in Quantum Electronics* 9.6 (2003), pp. 1552–1569. DOI: 10.1109/JSTQE.2003.820922.

[5] P. W. Shor. "Algorithms for quantum computation: discrete logarithms and factoring". In: *Proceedings 35th Annual Symposium on Foundations of Computer Science*. 1994, pp. 124–134. DOI: 10.1109/SFCS.1994.365700.

[6] Lov K. Grover. "A fast quantum mechanical algorithm for database search". In: *Proceedings of the twenty-eighth annual ACM symposium on Theory of computing - STOC '96*. Vol. 41. 3. ACM Press, 1996, pp. 212–219. DOI: 10.1145/237814.237866.

[7] Alán Aspuru-Guzik and Philip Walther. "Photonic quantum simulators". In: *Nature Physics* 8.4 (2012), pp. 285–291. DOI: 10.1038/nphys2253.

[8] I. M. Georgescu, S. Ashhab, and Franco Nori. "Quantum simulation". In: *Reviews of Modern Physics* 86.1 (2014), pp. 153–185. DOI: 10.1103/RevModPhys.86.153. arXiv: 1308.6253.

[9] Jeremy L. O'Brien, Akira Furusawa, and Jelena Vučković. "Photonic quantum technologies". In: *Nature Photonics* 3.12 (2009), pp. 687–695. DOI: 10.1038/nphoton.2009.229. arXiv: 1003.3928.

[10] Jacques Carolan et al. "Universal linear optics". In: *Science* 349.6249 (2015), pp. 711–716. DOI: 10.1126/science.aab3642. arXiv: 1505.01182.

[11] Nicholas C. Harris et al. "Linear programmable nanophotonic processors". In: *Optica* 5.12 (2018), p. 1623. DOI: 10.1364/optica.5.001623.

[12] Han-Sen Zhong et al. "Quantum computational advantage using photons". In: *Science* (2020). DOI: 10.1126/science.abe8770.

[13] H. J. Kimble. "The quantum internet". In: *Nature* 453.7198 (2008), pp. 1023–1030. DOI: 10.1038/nature07127. arXiv: 0806.4195.

[14] "Quantum internet: A vision for the road ahead". In: *Science* 362.6412 (2018), eaam9288. DOI: 10.1126/science.aam9288.

[15] Charles H. Bennett and Gilles Brassard. "Quantum cryptography: Public key distribution and coin tossing". In: *Theoretical Computer Science* 560.2 (2014), pp. 7–11. DOI: 10.1016/j.tcs.2014.05.025.

[16] Anne Broadbent, Joseph Fitzsimons, and Elham Kashefi. "Universal Blind Quantum Computation". In: *2009 50th Annual IEEE Symposium on Foundations of Computer Science*. IEEE, 2009, pp. 517–526. DOI: 10.1109/FOCS.2009.36. arXiv: 0807.4154.

[17] Pieter Kok et al. "Linear optical quantum computing with photonic qubits". In: *Reviews of Modern Physics* 79.1 (2007), pp. 135–174. DOI: 10.1103/RevModPhys.79.135.

[18] N. Somaschi et al. "Near-optimal single-photon sources in the solid state". In: *Nature Photonics* 10.5 (2016), pp. 340–345. DOI: 10.1038/nphoton.2016.23. arXiv: 1510.06499.

[19] Peter Lodahl. "Quantum-dot based photonic quantum networks". In: *Quantum Science and Technology* 3.1 (2018). DOI: 10.1088/2058-9565/aa91bb. arXiv: 1707.02094.

[20] J T Shen and Shanhui Fan. "Coherent photon transport from spontaneous emission in one-dimensional waveguides". In: *Optics Letters* 30.15 (2005), p. 2001. DOI: 10.1364/OL.30.002001.

[21] M. Arcari et al. "Near-Unity Coupling Efficiency of a Quantum Emitter to a Photonic Crystal Waveguide". In: *Physical Review Letters* 113.9 (2014), p. 093603. DOI: 10.1103/PhysRevLett.113.093603. arXiv: 1402.2081.

[22] Feng Liu et al. "High Purcell factor generation of indistinguishable on-chip single photons". In: *Nature Nanotechnology* 13.9 (2018), pp. 835–840. DOI: 10.1038/s41565-018-0188-x.

[23] Peter Lodahl, Sahand Mahmoodian, and Soren Stobbe. "Interfacing single photons and single quantum dots with photonic nanostructures". In: *Reviews of Modern Physics* 87.2 (2015), pp. 347–400. DOI: 10.1103/RevModPhys.87.347. arXiv: 1312.1079.

[24] P. Gallo et al. "Integration of site-controlled pyramidal quantum dots and photonic crystal membrane cavities". In: *Applied Physics Letters* 92.26 (2008), p. 263101. DOI: 10.1063/1.2952278.

[25] C. Roy and S. Hughes. "Phonon-Dressed Mollow Triplet in the Regime of Cavity Quantum Electrodynamics: Excitation-Induced Dephasing and Nonperturbative Cavity Feeding Effects". In: *Physical Review Letters* 106.24 (2011), p. 247403. DOI: 10.1103/PhysRevLett.106.247403.

[26] Leonardo Midolo, Albert Schliesser, and Andrea Fiore. "Nano-opto-electromechanical systems". In: *Nature Nanotechnology* 13.1 (2018), pp. 11–18. DOI: 10.1038/s41565-017-0039-1.

[27] Sangyoon Han et al. "Large-scale silicon photonic switches with movable directional couplers". In: *Optica* 2.4 (2015), p. 370. DOI: 10.1364/OPTICA.2.000370.

[28] M. Poot and H. X. Tang. "Broadband nanoelectromechanical phase shifting of light on a chip". In: *Applied Physics Letters* 104.6 (2014), p. 061101. DOI: 10.1063/1.4864257. arXiv: 1312.2454.

[29] Peng Shi et al. "Tuning the quality factor of split nanobeam cavity by nanoelectromechanical systems". In: *Optics Express* 23.15 (2015), p. 19338. DOI: 10.1364/OE.23.019338.

[30] Terry Rudolph. "Why i am optimistic about the silicon-photonic route to quantum computing". In: *APL Photonics* 2.3 (2017). DOI: 10.1063/1.4976737. arXiv: 1607.08535.

[31] D. J.P. Ellis et al. "Independent indistinguishable quantum light sources on a reconfigurable photonic integrated circuit". In: *Applied Physics Letters* 112.21 (2018). DOI: 10.1063/1.5028339.

[32] Xing Ding et al. "On-Demand Single Photons with High Extraction Efficiency and Near-Unity Indistinguishability from a Resonantly Driven Quantum Dot in a Micropillar". In: *Physical Review Letters* 116.2 (2016), p. 020401. DOI: 10.1103/PhysRevLett.116.020401. arXiv: 1601.00284.

[33] Pascale Senellart, Glenn Solomon, and Andrew White. "High-performance semiconductor quantum-dot single-photon sources". In: *Nature Nanotechnology* 12.11 (2017), pp. 1026–1039. DOI: 10.1038/nnano.2017.218.

[34] Hui Wang et al. "Towards optimal single-photon sources from polarized microcavities". In: *Nature Photonics* 13.11 (2019), pp. 770–775. DOI: 10.1038/s41566-019-0494-3.

[35] T. Lund-Hansen et al. "Experimental Realization of Highly Efficient Broadband Coupling of Single Quantum Dots to a Photonic Crystal Waveguide". In: *Physical Review Letters* 101.11 (2008), p. 113903. DOI: 10.1103/PhysRevLett.101.113903. arXiv: 0805.3485.

[36] Julien Claudon et al. "A highly efficient single-photon source based on a quantum dot in a photonic nanowire". In: *Nature Photonics* 4.3 (2010), pp. 174–177. DOI: 10.1038/nphoton.2009.287.

[37] K.H. Drexhage. "Influence of a dielectric interface on fluorescence decay time". In: *Journal of Luminescence* 1-2.C (1970), pp. 693–701. DOI: 10.1016/0022-2313(70)90082-7.

[38] Camille Papon et al. "Nanomechanical single-photon routing". In: *Optica* 6.4 (2019), p. 524. DOI: 10.1364/optica.6.000524. arXiv: 1811.10962.

[39] Richard J. Warburton. "Single spins in self-assembled quantum dots". In: *Nature Materials* 12.6 (2013), pp. 483–493. DOI: 10.1038/nmat3585.

[40] Thomas Ihn. *Semiconductor Nanostructures: Quantum States and Electronic Transport*. Oxford University Press, 2010.

[41] Ravitej Uppu et al. "On-chip deterministic operation of quantum dots in dual-mode waveguides for a plug-and-play single-photon source". In: *Nature Communications* 11.1 (2020), p. 3782. DOI: 10.1038/s41467-020-17603-9. arXiv: 2001.10716.

[42] Emmanuel Rosencher and Borge Vinter. *Optoelectronics*. Cambridge University Press, 2002. DOI: 10.1017/CBO9780511754647.

[43] Lukas Novotny and Bert Hecht. *Principles of nano-optics*. Cambridge University Press, 2009. DOI: 10.1017/CBO9780511794193.

[44] Peter Lodahl. "Controlling the dynamics of spontaneous emission from quantum dots by photonic crystals". In: *Nature* 430.7000 (2004), pp. 654–657. DOI: 10.1038/nature02772.

[45] K. Prindal-Nielsen. "Light matter interaction in nano-beam waveguides". MA thesis. University of Copenhagen, 2017.

[46] Christian Haffner et al. "Nano–opto-electro-mechanical switches operated at CMOS-level voltages". In: *Science* 366.6467 (2019), pp. 860–864. DOI: 10.1126/science.aay8645.

[47] Tao Chu et al. "A compact silicon nano-wire waveguide optic switch". In: *2005 IEEE International Conference on Group IV Photonics* 2005 (2005), pp. 134–136. DOI: 10.1109/group4.2005.1516429.

[48] Joris Van Campenhout et al. "Low-power, 2×2 silicon electro-optic switch with 110-nm bandwidth for broadband reconfigurable optical networks". In: *Optics Express* 17.26 (2009), pp. 24020–24029. DOI: 10.1364/oe.17.024020.

[49] Camille Papon. "Nano-Electro-Mechanical Switches for Quantum Photonic Applications: Fabrication and Characterization". MA thesis. University of Copenhagen, 2018.

[50] Hermann A. Haus and Weiping Huang. "Coupled-Mode Theory". In: *Proceedings of the IEEE* 79.10 (1991), pp. 1505–1518. DOI: 10.1109/5.104225.

[51] Chin-Lin Chen. *Foundations for Guided-Wave Optics*. John Wiley & Sons, Inc., 2006. DOI: 10.1002/0470042222.

[52] Peter Markos and Costas M. Soukoulis. *Wave Propagation*. Princeton University Press, 2008. DOI: 10.1515/9781400835676.

[53] Lukas Chrostowski and Michael Hochberg. *Silicon Photonics Design*. Cambridge University Press, 2015. DOI: 10.1017/CBO9781316084168.

[54] Yi Zhang et al. "Sagnac loop mirror and micro-ring based laser cavity for silicon-on-insulator". In: *Optics Express* 22.15 (2014), p. 17872. DOI: 10.1364/OE.22.017872.

[55] Dana E. Westmoreland et al. "Properties of quantum dots coupled to plasmons and optical cavities". In: *The Journal of Chemical Physics* 151.21 (2019), p. 210901. DOI: 10.1063/1.5124392.

[56] Xiaoyan Zhou et al. "On-Chip Nanomechanical Filtering of Quantum-Dot Single-Photon Sources". In: *Laser & Photonics Reviews* 14.7 (2020), p. 1900404. DOI: 10.1002/lpor.201900404.

[57] Kazuhiro Kuruma et al. “Surface-passivated high- Q GaAs photonic crystal nanocavity with quantum dots”. In: *APL Photonics* 5.4 (2020), p. 046106. DOI: 10.1063/1.5144959. arXiv: 2001.02377.

[58] Jack W. Judy. “Microelectromechanical systems (MEMS): fabrication, design and applications”. In: *Smart Materials and Structures* 10.6 (2001), pp. 1115–1134. DOI: 10.1088/0964-1726/10/6/301.

[59] Robert Bogue. “Recent developments in MEMS sensors: a review of applications, markets and technologies”. In: *Sensor Review* 33.4 (2013), pp. 300–304. DOI: 10.1108/SR-05-2013-678.

[60] Ian W. Frank et al. “Programmable photonic crystal nanobeam cavities”. In: *Optics Express* 18.8 (2010), p. 8705. DOI: 10.1364/OE.18.008705.

[61] Kateřina Dohnalová et al. “Surface brightens up Si quantum dots: direct bandgap-like size-tunable emission”. In: *Light: Science & Applications* 2.1 (2013), e47–e47. DOI: 10.1038/lsa.2013.3.

[62] Arne Ludwig et al. “Ultra-low charge and spin noise in self-assembled quantum dots”. In: *Journal of Crystal Growth* 477 (2017), pp. 193–196. DOI: 10.1016/j.jcrysgro.2017.05.008.

[63] T.R. Groves. “3 - Electron beam lithography”. In: *Nanolithography*. Elsevier, 2014. DOI: 10.1533/9780857098757.80.

[64] Wenchuang (Walter) Hu et al. “Sub-10 nm electron beam lithography using cold development of poly(methylmethacrylate)”. In: *Journal of Vacuum Science & Technology B: Microelectronics and Nanometer Structures* 22.4 (2004), p. 1711. DOI: 10.1116/1.1763897.

[65] Xiaoyan Zhou et al. “High-efficiency shallow-etched grating on GaAs membranes for quantum photonic applications”. In: *Applied Physics Letters* 113.25 (2018), p. 251103. DOI: 10.1063/1.5055622. arXiv: 1809.03189.

[66] Anton Kobelev et al. “Boron Trichloride Dry Etching”. In: *Encyclopedia of Plasma Technology*. December. CRC Press, 2016. DOI: 10.1081/E-EPLT-120053961.

[67] Henri Jansen et al. “BSM 7: RIE lag in high aspect ratio trench etching of silicon”. In: *Microelectronic Engineering* 35.1-4 (1997), pp. 45–50. DOI: 10.1016/S0167-9317(96)00142-6.

[68] R. J. Shul et al. “Inductively coupled plasma etching of GaN”. In: *Applied Physics Letters* 69.8 (1996), pp. 1119–1121. DOI: 10.1063/1.117077.

[69] L. Midolo et al. “Soft-mask fabrication of gallium arsenide nanomembranes for integrated quantum photonics”. In: *Nanotechnology* 26.48 (2015), p. 484002. DOI: 10.1088/0957-4484/26/48/484002. arXiv: 1506.00376.

[70] Roya Maboudian. “Critical Review: Adhesion in surface micromechanical structures”. In: *Journal of Vacuum Science & Technology B: Microelectronics and Nanometer Structures* 15.1 (1997), p. 1. DOI: 10.1116/1.589247.

[71] “Perspective of self-assembled InGaAs quantum-dots for multi-source quantum implementations”. In: *Applied Physics Letters* 117.3 (2020), p. 030501. DOI: 10.1063/5.0010782.

[72] Stephen G. Lipson, Henry Lipson, and David Stefan Tannhauser. *Optical Physics*. Cambridge University Press, 1995. DOI: 10.1017/CBO9781139170413.

[73] M. Kaniber et al. “Investigation of the nonresonant dot-cavity coupling in two-dimensional photonic crystal nanocavities”. In: *Physical Review B* 77.16 (2008), p. 161303. DOI: 10.1103/PhysRevB.77.161303.

[74] Arka Majumdar et al. “Phonon mediated off-resonant quantum dot–cavity coupling under resonant excitation of the quantum dot”. In: *Physical Review B* 84.8 (2011), p. 085309. DOI: 10.1103/PhysRevB.84.085309.

[75] Jingfu Ye, Yan Li, and Shiliang Qu. “Design and theoretical demonstration of an on-chip metal Bragg grating switch based on two-beam interference”. In: *Journal of Physics D: Applied Physics* 53.25 (2020), p. 255101. DOI: 10.1088/1361-6463/ab7ac9.

[76] A.G. Rickman, G.T. Reed, and F. Namavar. “Silicon-on-insulator optical rib waveguide loss and mode characteristics”. In: *Journal of Lightwave Technology* 12.10 (1994), pp. 1771–1776. DOI: 10.1109/50.337489.

[77] Jake Iles-Smith et al. “Phonon scattering inhibits simultaneous near-unity efficiency and indistinguishability in semiconductor single-photon sources”. In: *Nature Photonics* 11.8 (2017), pp. 521–526. DOI: 10.1038/nphoton.2017.101.

[78] L. Midolo et al. “Spontaneous emission control of single quantum dots by electromechanical tuning of a photonic crystal cavity”. In: *Applied Physics Letters* 101.9 (2012), p. 091106. DOI: 10.1063/1.4748302. arXiv: 1207.2980.

[79] Zhe Xiao et al. “Ultra-compact low loss polarization insensitive silicon waveguide splitter”. In: *Optics Express* 21.14 (2013), p. 16331. DOI: 10.1364/OE.21.016331.

[80] Daquan Yang, Huiping Tian, and Yuefeng Ji. “High-bandwidth and low-loss photonic crystal power-splitter with parallel output based on the integration of Y-junction and waveguide bends”. In: *Optics Communications* 285.18 (2012), pp. 3752–3757. DOI: 10.1016/j.optcom.2012.05.022.

[81] G.R. Simpson. “A Generalized n-Port Cascade Connection”. In: *MTT-S International Microwave Symposium Digest*. Vol. 81. MTT005, 1981, pp. 507–509. DOI: 10.1109/MWSYM.1981.1129978.

Cascading junctions formalism

The following derivation of the method of cascading junctions is adopted from ref. [81], and is here applied to S-matrices describing optical structures. A cascade junction is defined as a connection between two ports from two different systems, with corresponding individual S-matrices. By combining the two systems, this cascade junction ends up becoming internal to the resulting system. This approach can be generalised to any amount of ports and cascading junctions, with the only requirement being that at least one port remains open to the environment. In the following, the generalized case with two systems connected by n cascade junctions is considered, illustrated in fig. A.1.

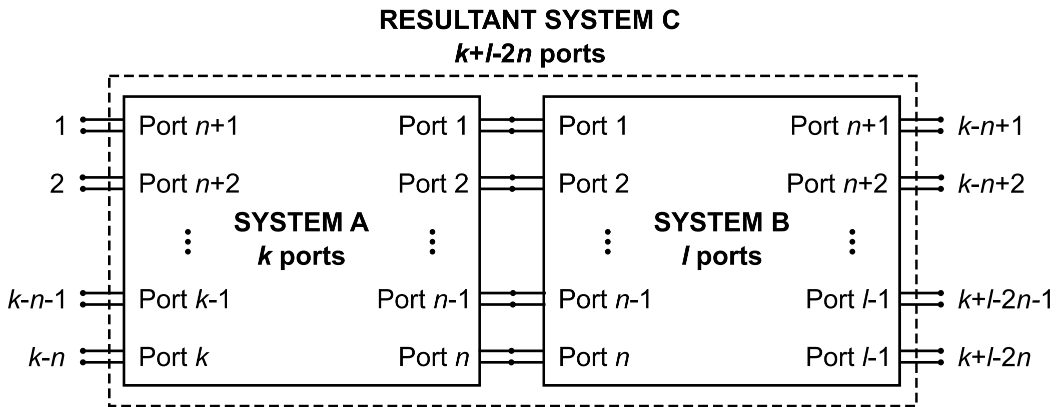

Figure A.1: Generalized cascade connection. Cascading two systems with k ports and l ports, respectively, with n junctions results in a combined system with $k + l - 2n$ ports. The ports of the individual systems are numbered so that the lowest number ports are cascaded.

For system A containing k ports and system B containing l ports, the combined system C will have $k+l-2n$ ports. The ports are numbered so that the lowest number ports of each system are combined to form the cascade junctions. To compute the S-matrix of the combined system S_C, the S-matrices of system A (S_A) and system B (S_B) are split into four sections each as showed in fig. A.2, forming eight smaller

matrices S_1 to S_8. These can then be inserted into the following equations that give

$$
S_A = \left|\begin{array}{cccc:cccc}
S^A_{1,1} & S^A_{1,2} & \cdots & S^A_{1,n} & S^A_{1,n+1} & \cdots & \cdots & S^A_{1,k} \\
S^A_{2,1} & & & \vdots & \vdots & & & \vdots \\
\vdots & & S_1 & \vdots & \vdots & S_2 & & \vdots \\
S^A_{n,1} & \cdots & \cdots & S^A_{n,n} & S^A_{n,n+1} & \cdots & \cdots & S^A_{n,k} \\
\hdashline
S^A_{n+1,1} & \cdots & \cdots & S^A_{n+1,n} & S^A_{n+1,n+1} & \cdots & \cdots & S^A_{n+1,k} \\
\vdots & & S_3 & \vdots & \vdots & S_4 & & \vdots \\
\vdots & & & \vdots & \vdots & & & \vdots \\
S^A_{k,1} & \cdots & \cdots & S^A_{k,n} & S^A_{k,n+1} & \cdots & \cdots & S^A_{k,k}
\end{array}\right|
\quad
S_B = \left|\begin{array}{cccc:cccc}
S^B_{1,1} & S^B_{1,2} & \cdots & S^B_{1,n} & S^B_{1,n+1} & \cdots & \cdots & S^B_{1,l} \\
S^B_{2,1} & & & \vdots & \vdots & & & \vdots \\
\vdots & & S_5 & \vdots & \vdots & S_6 & & \vdots \\
S^B_{n,1} & \cdots & \cdots & S^B_{n,n} & S^B_{n,n+1} & \cdots & \cdots & S^B_{n,l} \\
\hdashline
S^B_{n+1,1} & \cdots & \cdots & S^B_{n+1,n} & S^B_{n+1,n+1} & \cdots & \cdots & S^B_{n+1,l} \\
\vdots & & S_7 & \vdots & \vdots & S_8 & & \vdots \\
\vdots & & & \vdots & \vdots & & & \vdots \\
S^B_{l,1} & \cdots & \cdots & S^B_{l,n} & S^B_{l,n+1} & \cdots & \cdots & S^B_{l,l}
\end{array}\right|
$$

Figure A.2: Decomposition of the S-matrices. The S-matrices of systems A and B are decomposed into eight smaller matrices, with system A forming the matrices S_1 to S_4, and system B forming the matrices S_5 to S_8.

the components of S_C:

$$S_I = S_3 S_5 (I - S_1 S_5)^{-1} S_2 + S_4, \tag{A.1}$$

$$S_{II} = S_3 S_5 (I - S_1 S_5)^{-1} S_1 S_6 + S_3 S_6, \tag{A.2}$$

$$S_{III} = S_7 (I - S_1 S_5)^{-1} S_2, \tag{A.3}$$

$$S_{IV} = S_7 (I - S_1 S_5)^{-1} S_1 S_6 + S_8. \tag{A.4}$$

Equations A.1-4 can subsequently be combined to generate the combined S-matrix S_C:

$$S_C = \begin{bmatrix} S_I & S_{II} \\ S_{III} & S_{IV} \end{bmatrix} \tag{A.5}$$

A.1 Degenerate cases

The previous equations are general, and can be used for any k, l and n. They can however be greatly simplified in the following two degenerate cases:

1. $k = n$ and $l > n$: all ports of system A are cascaded. In this case, S_2, S_3, and S_4 do not exist, eliminating equations A.1, A.2, and A.3. S_C is then given solely by equation A.4:
$$S_C = S_{IV} \tag{A.6}$$

2. $l = n$ and $k > n$: all ports of system B are cascaded. In this case, S_6, S_7, and S_8 do not exist, eliminating equations A.2, A.3, and A.4. S_C is then given solely by equation A.1:
$$S_C = S_I \tag{A.7}$$

A.2 Matlab code

A Matlab-function developed for this project to compute cascading junctions is given below. It is called by `cascade_smatrices(S_A,S_B,nports)`, which takes the inputs `S_A` and `S_B`, that are the two S-matrices to be combined, and `nports`, that are the amount of cascading junctions. It can also handle symbolic variables, but this requires the Symbolic Math Toolbox. Variables can be defined using the `syms` command.

```
function S_out = cascade_smatrices(S_A,S_B,nports)
%This function can help you calculate the combined S-matrix
%for two devices in junction

%Defines S-matrices
s_A = S_A;
s_B = S_B;

%Specify number of cascading ports
n = nports;

%Finds number of ports in the two devices
k = length(s_A);
l = length(s_B);

%Calculates smaller matrices
s_1 = s_A(1:n,1:n);
s_2 = s_A(1:n,n+1:k);
s_3 = s_A(n+1:k,1:n);
s_4 = s_A(n+1:k,n+1:k);
s_5 = s_B(1:n,1:n);
s_6 = s_B(1:n,n+1:l);
s_7 = s_B(n+1:l,1:n);
s_8 = s_B(n+1:l,n+1:l);

%Calculates equations
s_I = s_3*s_5*(inv(eye(n)-s_1*s_5))*s_2+s_4;
s_II = s_3*s_5*(inv(eye(n)-s_1*s_5))*s_1*s_6+s_3*s_6;
s_III = s_7*(inv(eye(n)-s_1*s_5))*s_2;
s_IV = s_7*(inv(eye(n)-s_1*s_5))*s_1*s_6+s_8;

%Outputs combined S-matrix
S_out = [s_I,s_II;s_III,s_IV];
```

Appendix B

Optimized fabrication recipe

Chapter 3 introduced the general process for fabricating MEMS/NEMS devices. This appendix presents the detailed fabrication recipe used in this work.

Metal deposition and lift-off

1. Cleave a 10×10 mm^2 chip of undoped wafer with medium/high QD density
2. Sonicate in acetone (80 kHz, 30 % power) for 2 min. Flush with IPA and blow-dry with N_2
3. Spin-coat $\sim$ 60 µL ZEP520 resist at 2200 RPM for 60 sec
4. Bake on hot-plate at 185 °C for 5 min
   4.1. Resulting thickness can be measured on Filmetrics Thin Film Measurement system. Desired resist thickness is (550 ± 20) nm
   4.2. If thickness is outside tolerance, strip resist in 70 °C NMP for 10 min, followed by RT NMP for 2 min. Flush by IPA and blow-dry with N_2. Repeat from step 3
5. Run PEC on mask file with Beamfox Proximity. Suggested settings for Elionix F-125 EBL system at 125 kV:
   5.1. For thin electrodes and alignment markers: field size 500 µm, number of dots 1 million, pitch 8, current 1 nA, clearance dose 150 µC/cm^2. Average dwell time should be 0.024 µs
   5.2. For large bonding pads: field size 500 µm, number of dots 1 million, pitch 40, current 20 nA, clearance dose 180 µC/cm^2. Average dwell time should be 0.036 µs
6. Expose sample with Elionix F-125
7. Develop in n-amylacetate at RT for 70 sec. Rinse 10 sec in IPA and blow-dry
8. Descum in oxygen plasma at 100 W for 45 sec
9. In PVD system, apply Ar plasma etching for 60 sec before deposition. Evaporate 10 nm Cr followed by 170 nm Au
10. Lift-off: place sample in 80 °C NMP for 5 min. Sonicate (80 kHz, 50 % power) for 30 sec. Again in 80 °NMP for 5-10 min. Sonicate again (80 kHz, 50 % power) for 20 sec. Rinse in RT NMP for 2 min. Flush in IPA and blow-dry

10.1. Warning: do not sonicate further. Overdoing lift-off can lead to stripping of small electrodes, detrimental to device performance.

Etching of shallow-etched gratings

1. Dehydrate sample on hot-plate at 185 °C for 5 min
2. Spin-coat ∼ 60 µL CSAR 9% resist at 4000 RPM for 60 sec
3. Bake on hot-plate at 185 °C for 1 min
   3.1. Desired resist thickness is (220 ± 10) nm
   3.2. If thickness is outside tolerance, strip resist in RT 1,3-dioxolane for 10 min. Repeat from step 2.
4. Run PEC on mask file with Beamfox Proximity. Suggested settings for Elionix F-125 EBL system at 125 kV: field size 500 µm, number of dots 1 million, pitch 4, current 1 nA, clearance dose 350 µC/cm^2. Average dwell time should be 0.014 µs
5. Expose sample with Elionix F-125
6. Develop in n-amylacetate at -5 °C for 40 sec. Temperature should remain stable throughout development. Temperature set point can be set to -10 °C if struggling to maintain stable temperature. Rinse 10 sec in IPA and blow-dry with N_2
7. RIE in BCl_3/Ar (5:10), RF power 43 W, pressure 20 mTorr. Monitor etching depth with end-point detection in a 200 × 200 µm^2 square. User ends process approximately when reflection curve has reached $1\frac{1}{4}$ period.
   7.1. Etch depth can after resist removal be measured with a profilometer. Etching depth should in reference square be (90 ± 10) nm.
8. Strip residual resist in RT 1,3-dioxolane for 10 min. Rinse 10 sec in IPA and blow-dry with N_2

Etching and undercut of photonic structures

1. Dehydrate sample on hot-plate at 185 °C for 5 min
2. Spin-coat ∼ 60 µL ZEP520 resist at 2200 RPM for 60 sec
3. Bake on hot-plate at 185 °C for 5 min
   3.1. Desired resist thickness is (550 ± 20) nm
   3.2. If thickness is outside tolerance, strip resist in 70 °C NMP for 10 min, followed by RT NMP for 2 min. Flush by IPA and blow-dry with N_2. Repeat from step 2.
4. Run PEC on mask file with Beamfox Proximity. Suggested settings for Elionix F-125 EBL system at 125 kV: field size 500 µm, number of dots 1 million, pitch 4, current 1 nA, clearance dose 350 µC/cm^2. Average dwell time should be 0.014 µs
5. Expose sample with Elionix F-125
6. Develop in n-amylacetate at -5 °C for 40 sec. Rinse 10 sec in IPA and blow-dry with N_2
7. ICP etch in BCl_3/Cl_2/Ar (3:4:25), RF power 43 W, ICP power 300 W, pressure 4.7 mTorr. Monitor etching depth with end-point detection on bulk resist.

System ends process when roughly 260 nm resist remains. Etch time is typically 45-60 sec

8. Strip residual resist in 70 °C NMP for 10 min, followed by RT NMP for 2 min. Rinse 10 sec in IPA and blow-dry with N_2
9. Preparation for wet etching and subsequent cleaning procedure should be done simultaneously
   - 9.1. Clean all beakers and equipment with MQ water 5 times
   - 9.2. Prepare small beaker with 5 % HF, 4 large beakers with MQ water
   - 9.3. Prepare H_3PO_4:MQ 1:10 solution. Extract 5 mL H_3PO_4 with pipette and deposit in beaker. Add 50 mL MQ water. Stir with pipette
   - 9.4. Pour a few mL H_2O_2 in a plastic disposable beaker
   - 9.5. Pour 10-15 mL MW water in medium sized plastic disposable beaker. Fill 4 similar plastic beakers with IPA
10. Wet etching: Place sample in plastic boat, and submerge in HF for 44 sec. Size of undercut depends on etching time.
11. End process by submerging in MQ water beaker, and subsequently switching between MQ water beakers. Submersion time for MQ water beakers are 10 sec/1.5 min/3 min/5 min
12. Note: in general, when the boat is moved to a beaker, lightly stir for about 10 sec and place on the bottom of the beaker. MQ water beakers should be cleaned with MQ water 5 times between each chemical cycle, and the MQ water should be replaced anew

Finishing cleaning and drying procedure

1. Prepare with step 9.
2. Clean for 1 min in H_2O_2. Repeat MQ water cycle from step 11.
3. Deoxidize in H_3PO_4 solution for 1 min. Repeat MQ water cycle from step 11.
4. Place boat in beaker containing 10-15 mL MQ water. Slowly pour in IPA from sidewall, as boat is gently stirred and moved upwards.
5. Transfer boat to 4 more beakers of IPA and submerge for 2 min in each. Remove the boat in the second beaker
6. Clean all CPD holder parts with IPA and blow-dry with N_2
7. Fill bottom part of CPD holder with IPA, place sample within, and assemble the rest of the CPD holder
8. Clean inside of CPD chamber and stirring magnet with IPA and wipe dry. Fill bottom of CPD chamber with IPA, and insert CPD holder. If required, fill in IPA from the chamber sides until IPA level is slightly above the middle of the viewing window
9. Close CPD chamber, open CO_2 bottle, and run MemsTest2 recipe in the CPD system. Drying time is approximately 2 hours
10. After completion, remove finished sample from CPD holder

Note: CSAR 13% can generally be used in place of ZEP520. Initial tests show that a dose correction coefficient of 1.2 applied when exposing provides acceptable results. At the time of writing, further tests are being conducted to optimize exposure parameters when using CSAR 13%.